University of Alberta

Application of a Biomechanical Finite Element Spine Model to the Vicious Cycle Scoliosis Growth Theory: Evaluation of Improved FEA Geometry and Material Assignment

by

Jonathan Winfield Fok

A thesis submitted to the Faculty of Graduate Studies and Research
in partial fulfillment of the requirements for the degree of

Masters of Science

Department of Mechanical Engineering

©Jonathan Winfield Fok

Fall 2009

Edmonton, Alberta

Examining Committee

Dr. Jason Carey, Department of Mechanical Engineering

Dr. Samer Adeeb, Department of Civil Engineering

Dr. Roger Toogood, Department of Mechanical Engineering

Dr. Gregory Kawchuk, Department of Physical Therapy

Mr. Jim Raso, Glenrose Rehabilitation Hospital

Dr. Andre McDonald, Department of Mechanical Engineering

Abstract

Scoliosis is defined as the abnormal three dimensional curvature of the spine with 80% of all cases being idiopathic in nature. If left unchecked, this condition can cause cardio-pulmonary complications and occasionally death. Currently, the most common method of treatment of scoliosis is through mechanical bracing or in extreme cases, corrective surgery. Current treatments can be further improved with a greater understand of the growth patterns of scoliotic spines. The objective of this study is to develop a finite element spine model capable of responding to loading conditions in a similar fashion to previous finite biomechanics spine model and utilize the 'vicious cycle' scoliosis theory in an effort to model scoliosis growth.

Using CT images of a healthy spine, a three dimensional finite element model of the L3-L4 vertebra is generated. Asymmetric loading due to compression and muscle forces can then be applied on the spine and the resultant stresses are then translated into equivalent thermal load. Using this thermal load, it is possible to cause the spine model to grow, thereby predicting the growth pattern of a spine due to asymmetric loading.

Acknowledgements

Table of Contents

List of Tables

List of Figures

R represents the radius of curvature, M_A is the moment caused by asymmetric loading, θ_1 is the wedge angle and θ is the angle at the cross section of interest 120

Nomenclature/Abbreviations

<u>Anatomical Viewing Planes</u>

Many studies often divide up the human body into several standardized planes so that different regions of the body can be referred to quickly and without confusion. These planes are created by imaginary lines and can be applied to the entire body as well as individual components such as a vertebra. The following table provides a description of the planes used in this study.

Viewing plane	Description	Visual Representation
Frontal/Coronal Plane	A plane which divides a structure into front and back parts	
Sagittal Plane	A plane which divides a structure into right and left parts	
Transverse Plane	A plane which divides a structure into top and bottom parts	
Median Plane	A special case of the sagittal plane that runs through the midpoint of a structure	[1]
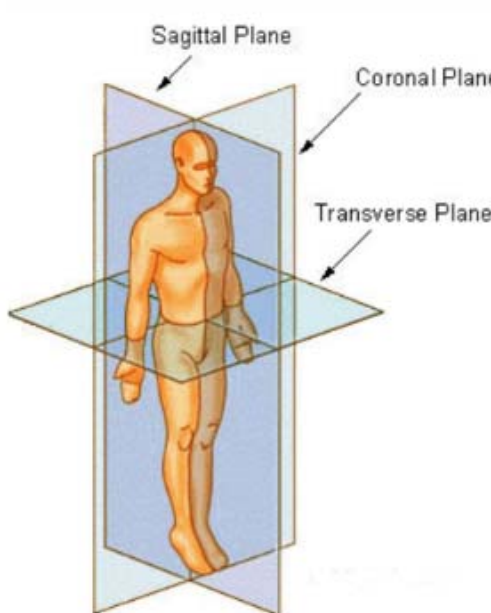
Anatomical Relations

The term 'left' or 'right' can allude to different locations depending on the viewing plane. Consequently there is a need for a consistent naming convention that can provide directional relations regardless of the viewing plane. The following table provides a summary of the anatomical relations used in this study. Note that the directional components (x, y, z) shown below is for illustration purposes and not necessarily the same as the coordinate system utilized for this study.

Viewing Plane	Description	Visual Representation
Medial - Lateral	Medial is nearer to the center of the body, lateral is farther away. 'x' direction	
Posterior - Anterior	Posterior is towards the back, anterior is towards the front. 'y' direction	
Inferior - Superior	Inferior is towards the bottom while superior is towards the top. 'z' direction	[1]
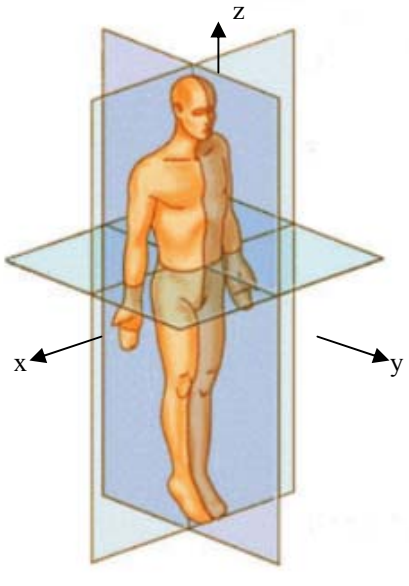
Material Property Nomenclature

Symbol	Unit	Description
E_{xx}	MPa	Elastic modulus along the x axis
E_{yy}	MPa	Elastic modulus along the y axis
E_{zz}	MPa	Elastic modulus along the z axis
G_{xy}	MPa	Shear modulus of a material along the x axis with a force applied along the y axis
G_{xz}	MPa	Shear modulus of a material along the x axis with a force applied along the z axis
G_{yz}	MPa	Shear modulus of a material along the y axis with a force applied along the z axis
ν_{xy}	Unitless	Poisson's ratio. Ratio of the strain in the y axis versus that in x axis when loaded in the x-axis
ν_{xz}	Unitless	Poisson's ratio. Ratio of the strain in the z axis versus that in x axis when loaded in the x-axis
ν_{yz}	Unitless	Poisson's ratio. Ratio of the strain in the z axis versus that in y axis when loaded in the y-axis

Abbreviations

Abbreviation	Full Name
CCRG	Confidence Connected Region Growing
CT	Computed Tomography
C	Cervical Vertebra/Region
^{o}C	Degree Centigrade
DOF	Degree of Freedom
FE	Finite Element
FEA	Finite Element Analysis
FEM	Finite Element Method
FSU	Functional Spinal Unit
IGES	Initial Graphic Exchange Specification
L	Lumbar Vertebra/Region
mm	Millimeter
MPa	Mega-Pascal
N	Newton
PDE	Partial Differential Equation
STL	Stereo Lithography
T	Thoracic Vertebra/Region

Chapter 1
Introduction and Project Scope

With recent advancements in computer processing power and software capabilities, it has become feasible and economically advantageous to utilize solvers which employ finite element analysis (FEA) to perform detailed studies on structures, even before a prototype has been produced. Such software and techniques allow researchers to develop a better understanding of the mechanical and geometric characteristics of the object they seek to study, which in turn allows for changes to be made to the device while it is still in the developmental phase.

In recent years, researchers have begun to apply computer modeling to the field of biomedical engineering as finite element modeling (FEM), allowing the performance of studies under pseudo *in-vivo* conditions. As such, there is now a better understanding of the human body mechanics to aid in the development of more effective treatments to various physical ailments. By using FEA, newly created prosthetic implants can be adapted to better match the mechanical characteristics of actual tissue before it is prototyped. More recently, FEA models have shown to successfully model the human spine, providing insights into spine biomechanics [2-9].

1.1 Motivation

Scoliosis is the abnormal three-dimensional deformation of the spine, and results in the lateral displacement of the spine as well as limited vertebra axial rotation [10]. This combined effect of the displacement and rotation results in the

spine developing into a 's' or 'c' shape when viewed on the frontal plane. While there have only been two known cases of untreated scoliosis causing death, the condition can lead to back pain and cardiopulmonary complications or failure [11, 12]. Scoliosis progression occurs primarily during puberty, affecting roughly 10 to 3% of the adolescent population; nearly 80% of which are idiopathic [11, 12].

As there is no known cause for this condition, there is a strong need to better understand the growth pattern of scoliosis spines to improve treatments of the disease. This can be accomplished through the use of FEA. By creating a spine computer model, it is possible to simulate spine growth over the pubertal period in adolescence; determine not only how a scoliotic spine will grow, but what types of loads will affect spine growth. Eventually, this information may allow for clinicians and future researchers to better predict scoliosis growth and determine the cause of scoliosis.

1.2 Objective

The objective of this study is to develop a biomechanical spine model analogue through the use of finite element analysis that can respond to mechanical loading in a similar manner to a human spine with the primary goal of applying it to a scoliosis growth model. Using this model, this study will also focus on the development of a spine growth model using the "vicious cycle" theory, detailed further in this study, which will simulate spine growth due to biological as well as mechanical factors such as external loading. The analysis will also be used to validate a common theory behind the cause of scoliosis, namely that asymmetric loads cause asymmetric spine growth which in turn develops into scoliosis.

To achieve this project goal, the following objectives must be met:

(1) Development of an anatomically accurate functional spinal unit (FSU) based on Computed Tomography (CT) scans of an individual not afflicted by scoliosis. This includes the appropriate application of material properties;

(2) Application of symmetric physiological loading on the FSU which accounts for body weight at the particular spine level as well as any muscle stabilization forces;

(3) Application of asymmetric loading on the FSU;

(4) Comparison between the asymmetric and symmetric stresses within each vertebral body of the FSU and assigning each stress value with a growth factor. This growth factor will account for both A) normal biological growth and B) growth caused by mechanical factors;

(5) Transforming the growth values into temperature loads and applying the temperature loads to the vertebral bodies. Vertebral body expansion due to the temperature loads is used to simulate spine growth for a period of one year;

(6) Updating of the deformed geometry and repeating steps two through six for a period of three years; and

(7) Validation of the final deformed model through comparison with other scoliosis growth models.

1.3 Scope

As the information achieved through this study is to be applied to the general scoliosis affected population, patient specific geometry and loading are undesirable. Consequently, the generated geometry will be generalized although important structural features of the vertebral body will be maintained.

Modeling of the entire vertebral column to such a high degree of detail as this study dictates would not only be time consuming but demand processing power that is beyond the scope of this work. Consequently only a portion of the spine, more specifically the L3/L4 region of the spine will be modeled. This region was chosen due to the clarity of the L3/L4 vertebra shapes from available CT scans.

1.4 Thesis Outline

For clarity, this thesis will be divided into seven sections with discussions on:

(1) Anatomical background: a discussion of the relevant anatomical background information of the spine such as geometry, mechanical characteristics and functions along with information regarding the definition of scoliosis and theories behind its development.

(2) Finite element analysis theory: the principle technique used in the growth model. Included in this section are some of the mathematical and element formulations used.

(3) Literature review of past spine and growth models: a detailed summary of the results and studies done by other researchers regarding both spine biomechanics model creation as well as scoliosis growth models.

(4) Development procedure and spine biomechanics studies: a discussion regarding the material properties, assumptions and idealizations utilized for the model. In addition, there will also be a discussion on the software utilized to create the geometric and finite element model as well as the procedure utilized to create the model and the simulation. Finally spine biomechanics validation will be performed on the created geometry.

(5) Scoliosis case study: a detailed discussion on the application of the generated FSU on a scoliosis growth model along with comparisons between the created model with scoliosis growth models generated by other researchers. Limitations of the current model will also be reviewed.

(6) Conclusion and future work: a summary of the results and their significance as well as thoughts as to how the model can be improved to provide a more patient specific model.

Chapter 2
Spine Physiology and Scoliosis Background

In order to properly create a biomechanically correct spine model, there must first be proper understanding of spine physiology. Without a clear understanding of the spine's physiological response to loading, or even its geometric features, any generated finite element (FE) model will not respond appropriately to any applied loading. General anatomical background information that is relevant to the project will be reviewed in this chapter. In the first section, background information vital to the understanding of the biomechanics of the spine will be presented. Included in this section are discussions regarding the vertebral column anatomy, and mechanical characteristics of the vertebra and intervertebral disk. This will be followed by a discussion regarding scoliosis as well as comments regarding some of the more popular theories behind its cause.

2.1 Biological Background

2.1.1 Vertebral Column Anatomy

Designed to support the torso, upper extremities and head, the vertebral column is also responsible for providing protection to the spinal cord and nerves as well as maintaining posture. The vertebral column consists of 33 vertebrae, sequentially from top to bottom: five cervical, twelve thoracic, seven lumbar, five sacral and four coccygeal. However, significant motion only occurs between the top 25 vertebrae (cervical to lumbar) as the nine lower vertebrae fuse together to form the sacrum and coccyx. A visual representation of a typical lumbar vertebra can be seen in Figure 2-1 below.
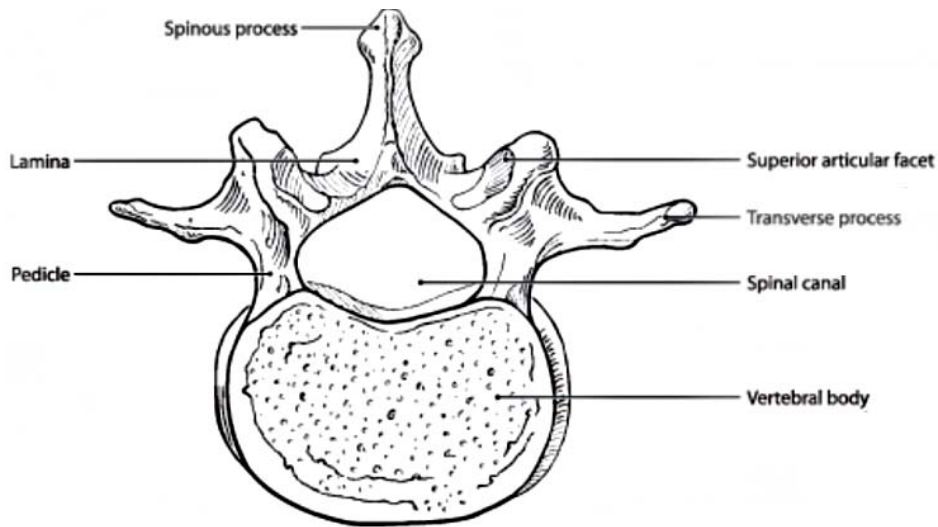
Normal lumbar vertebra, seen from above
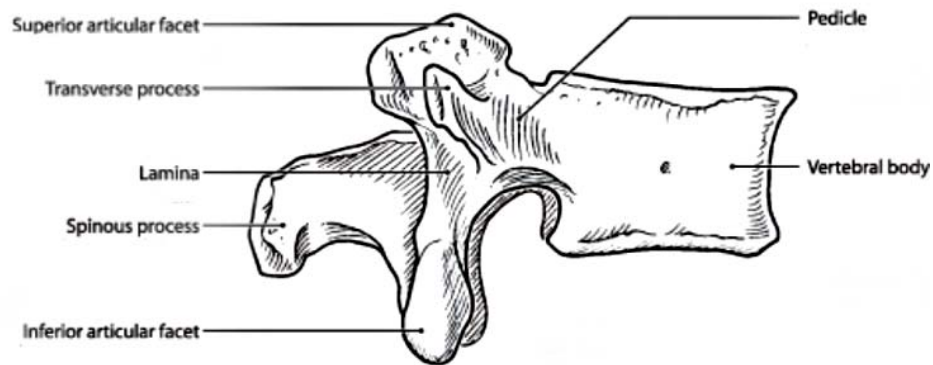
Normal lumbar vertebra, side view

Figure 2-1: Anatomy of a single lumbar vertebra. [13]

Classified as irregular bones, the vertebra consists of two distinct regions, the vertebral body and the posterior elements. The posterior elements of the vertebra are the attachment points for many of the vertebral column muscles and also serve to protect the spinal cord. Connection between the posterior elements and the vertebral body is achieved through two pedicles. Emerging from the posterolateral sides of the vertebral body, the posterior ends of the pedicles are

attached to two flat bones known as laminae which connect together at roughly the vertebra line of symmetry. The opening created by the pedicles, laminae and the vertebral body form a rough triangular cavity called the vertebral foramen or vertebral canal where the spinal cord runs. [14] Extending from the laminae are several processes: a single spinous process which projects posterior, two transverse processes which extend posterolaterally and four articular processes. Two of the articular processes extend superior to the laminae while the other two extend inferiorly. Combined with the articular processes of adjacent vertebra, these processes form joints known as facets. These joints allow for limited motion between segments and more importantly, restrain such motion to ensure there is no spinal cord damage.

The vertebral body is a massive, roughly cylindrical body which provides support for the weight of the upper body above it. The size of the vertebral body increases as it descends the spinal column as a response to increasing load, seen in Figure 2-2, with the greatest changes in vertebra size occurring from the mid thoracic region down.
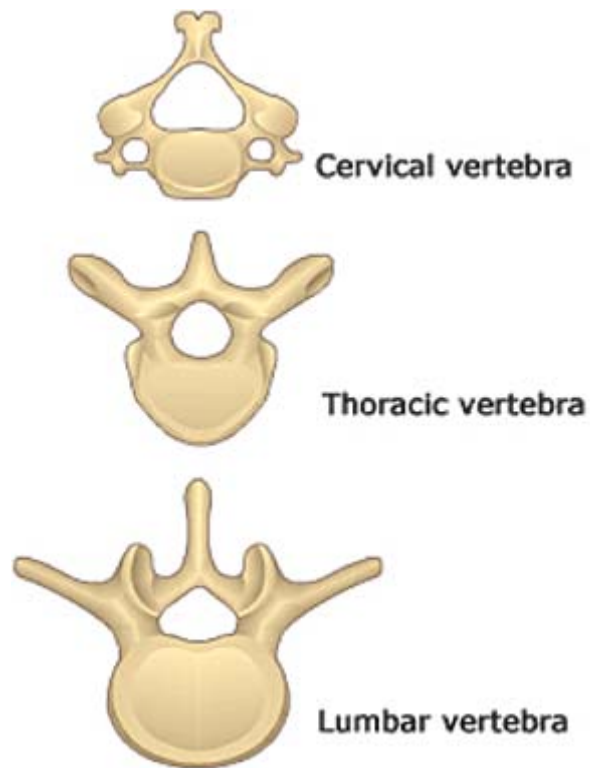
Figure 2-2: Vertebral body size comparisons. [15]

As with all bones, the vertebral body itself is comprised of two different types of bone: a hard, thin outer cortical bone shell and a porous inner core of cancellous or trabecular bone. While the cortical bone is highly dense with virtually no open spaces, the cancellous bone can best be described as a series of vertical bony columns reinforced by horizontal beams [14]. A comparison between cortical and cancellous bone makeup can be seen in Figure 2-3.
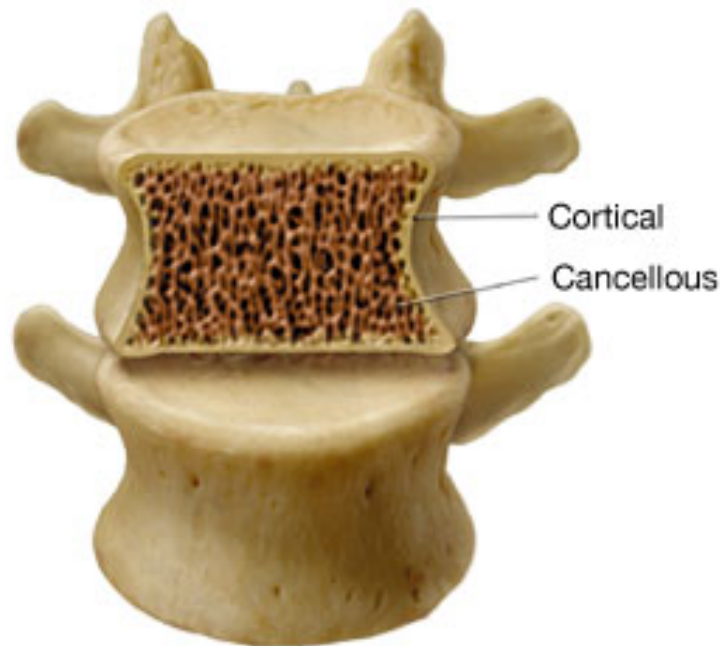
Figure 2-3: Structure of cancellous compared to cortical bone. [16]

The geometry of the vertebral body varies depending on the level of the spine. The smallest of the moveable vertebra, the cervical (C) vertebra bodies are approximately oval in shape with the narrower side appearing in anteroposterior direction. The thoracic (T) vertebral bodies are usually heart shaped, while the largest of the vertebra, the lumbar (L), are often described as kidney bean-shaped. Due to the ossification of the vertebral bodies, the outer rims of the inferior and superior surfaces of the vertebral body, known as the annular epiphysis, are often elevated when compared to the medial surfaces. Thus, these vertebral surfaces are often concave. It is also this ossification process that creates a concave lateral profile of the vertebral body as shown in Figure 2-4 [14]. As with most biological tissues however, this general shape varies between person to person and even within a single individual.
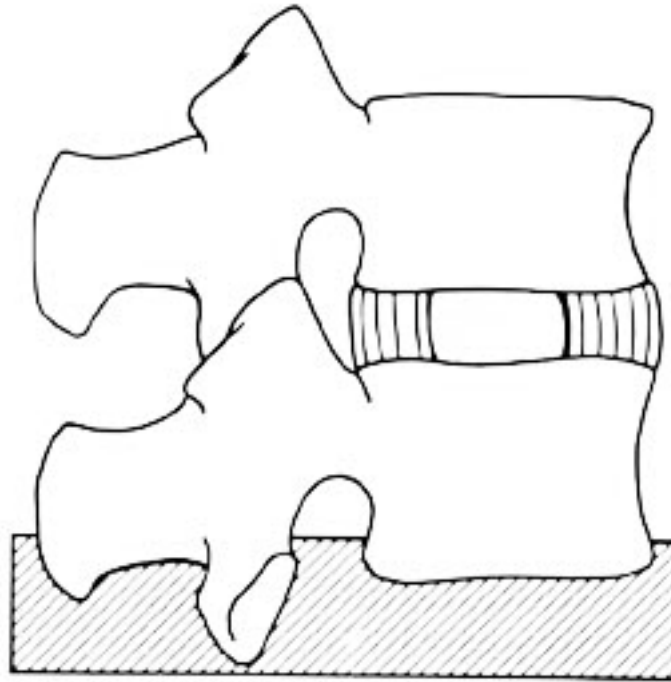
Figure 2-4: Sagittal profile of the vertebral body. Notice the slight concave profile on the side, top and bottom surfaces of the vertebral body. Adapted from White et al. [11]

With the exception of the connection between C1-C2, limited mobility along the spinal column is provided by twenty three intervertebral disks which are located between each non-fused adjacent vertebral bodies. These disks also allow for spine flexibility, load transmission and shock absorption although the latter function has been disputed as it is suggested that there is no reason why the spine would require more shock absorption capacity as compared to other long bones such as the femur [17].

Averaging about eleven millimeters in thickness, the disk itself can be divided into two different regions: the annulus fibrosus, a tough and fibrous outer ring, and the nucleus pulpous, a softer gelatin core. While there is a clear difference in structure between the annulus and the nucleus, there is no clear transitional zone between the different regions. The annulus usually consists of

twelve, one millimeter thick coaxial lamellae, forming a hollow cylinder which encloses the nucleus. The lamellae tend to be thicker and better defined in the anterior region of the disk while the posterior region tends to have lamellae which are not only thinner on average, but merge together as well. The outer lamellae layers form a direct attachment to the vertebral body while the inner lamellae layers attach to the cartilage endplates to form an enclosure which surrounds the nucleus. [18]

The annulus is composed of collagen fibers embedded in a ground substance. The fibers are usually tilted 30° from the transverse plane with the direction of tilt alternating between adjacent lamellae. Concentration of collagen fibers within the annulus tends to increase in the outer region due to the loading which the disk undergoes. The ground substance which bonds the collagen fibers together is similar to the gelatin substance found in the nucleus with the distinction being the ground substances' ability to form aggregates. The nucleus itself is a highly hydrated capsule in which water accounts for more than 80% of its total weight. The nucleus occupies anywhere between 30-50% of the transverse cross sectional area of the disk [11]. Some collagen fibers are present within the nucleus although unlike the annulus, they are not orientated in any particular direction [18]. A sketch that displays the gross anatomy of the intervertebral disk as well as the alternating annulus fibers is shown in Figure 2-5. A transverse section of the intervertebral disk taken from a 16 year old female can be seen in Figure 2-6.
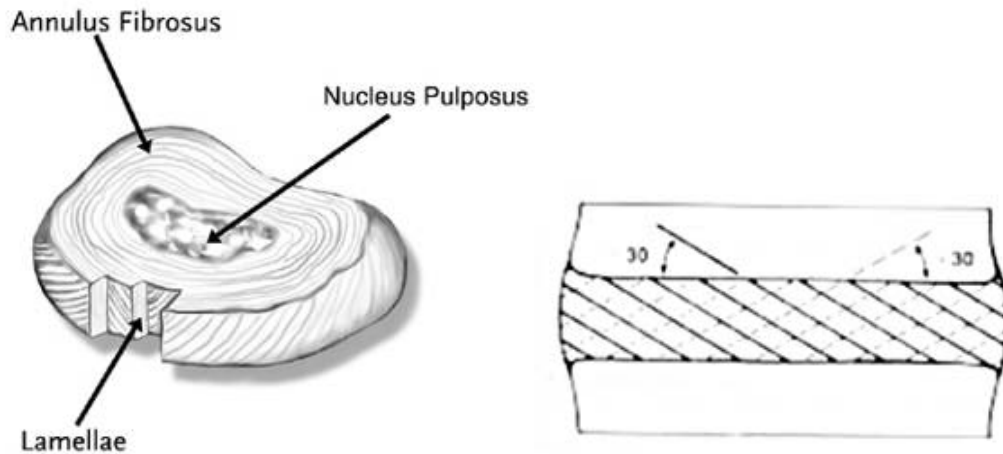
Figure 2-5: The lamellae layers of the intervertebral disk. The left image displays the gross anatomy of the intervertebral disk while the right image shows the orientation of the fibers. Adapted from White et al. [11]
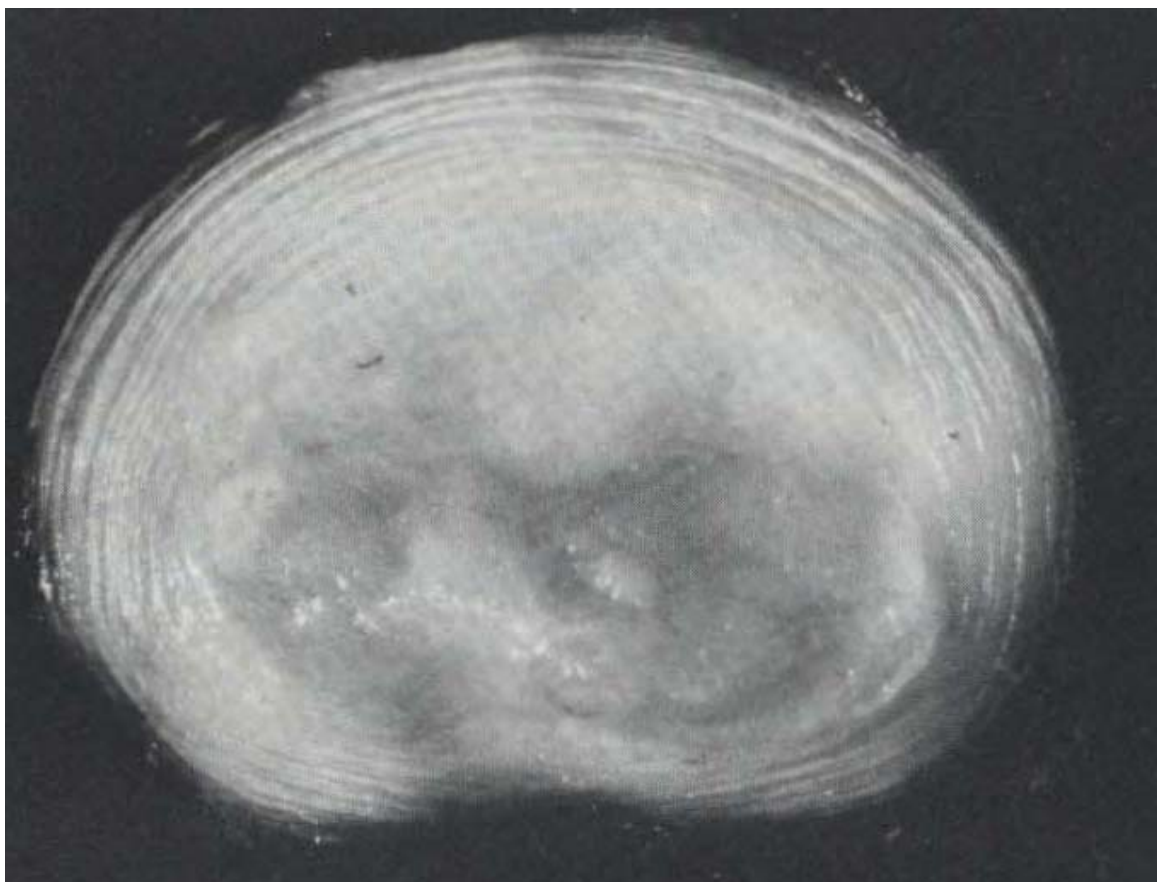
Figure 2-6: The nucleus pulposus of the intervertebral disk is the shinier and 'bubbly' region of the disk. The annulus surrounds the nucleus with clearly defined lines. Adapted from Ghosh [18]

The disk is roughly cylindrical in shape but often adopts an oval or 'kidney bean' shape. The transverse cross section is directly dependent on the

13

shape of the vertebra that it is attached to. When viewed in the sagittal section, the disk appears wedged shape with the anterior height greater than the posterior. Disk height does not vary significantly with its location in the spine although the relative size compared to that of the vertebra does decrease the farther down the spine [18]. Figure 2-7 below illustrates the sagittal view of the intervertebral disk.
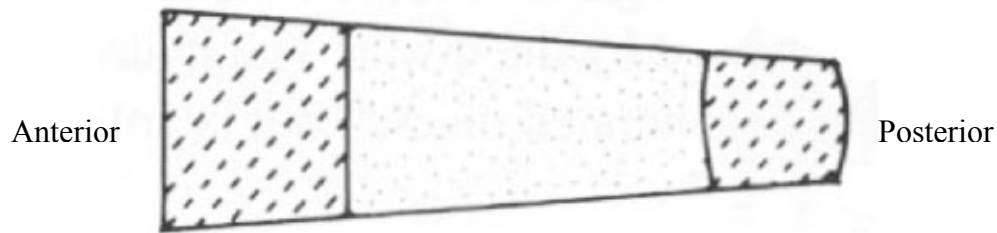
Figure 2-7: Sagittal view of the intervertebral disk. Adapted from Ghosh [17]

A final component of the FSU is the cartilage endplates located on the superior and inferior surfaces of the intervertebral disk. Composed primarily of collagen fibers, the endplate differs from the annulus in that it possesses no lamellae layers and the fibers are not tilted with respect to the transverse plane. The endplates are connected to the inner portion of the annulus region and not attached directly to the vertebral bodies themselves. As with the region between the annulus and the nucleus in the intervertebral disk, there is no clear transitional region between the endplates and the inner annulus region to which it is attached [18]. Figure 2-8 displays the total mobile unit of the intervertebral disk.
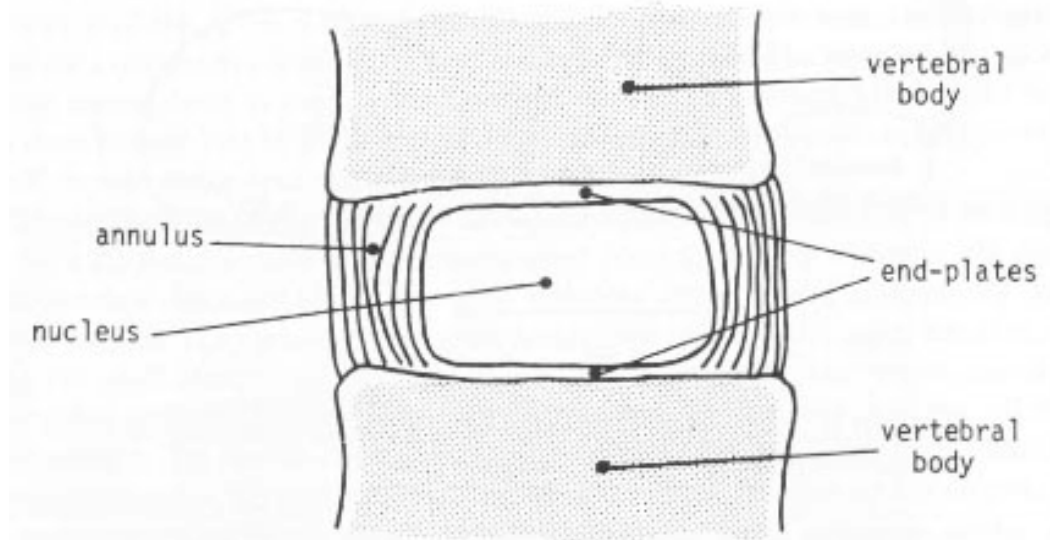
Figure 2-8: A simplified diagram of a motion segment of the spine. The endplate thickness has been exaggerated for clarity purposes. Adapted from Ghosh [18]

A physiologically accurate spine model should possess both cortical and cancellous bone regions as well as cartilage endplates on the superior and inferior surfaces of the vertebral bodies. These components should also accurately reflect the geometry seen in actual vertebra such as a concave lateral profile or a kidney bean transverse profile. The intervertebral disk should include distinct annulus layers and a separate nucleus pulposus; and have a variable transverse profile to account for changes in shape between adjacent vertebral bodies.

2.1.2 Mechanical Characteristics of the Vertebral Column

Bone is an anisotropic and heterogeneous material and slightly visco-elastic. Due to modeling difficulties however, bone is often oversimplified as a homogenous isotropic linear elastic material; or a slightly more accurate case as a transversely isotropic material. In terms of the vertebral body, the hard outer cortical shell provides much of the strength and stiffness needed to withstand the compressive loading of the human body. Studies have indicated that the cortical shell bears anywhere between 50 to 75% of the total compressive load depending

15

on the age of the individual. The cancellous core on the other hand, is not limited to simple load sharing with the cortical bone. When loaded to failure, it has been determined that the intrabecular spaces within the cancellous bone collapses resulting in the constraint of bone marrow. This constraint leads to an increase of hydraulic cushioning that can prevent further material failure. While the cortical bone strength tends to remain uniform throughout, the cancellous bone possesses greatest strength near its center and is weakest along the periphery. [12]

The intervertebral disk as a whole is a heterogeneous, visco-elastic material. Due to the unique makeup of the annulus and nucleus regions, the annulus fibers are always in a state of constant tension while the nucleus is in constant compression. This pre-stressing increases the disks' stiffness and rigidity [18].

Due to the orientation of the fiber angles, the annulus region resists circumferential, or hoop stress much more effectively than axial loading. In addition, it has been shown that the outer annulus region tends to be stiffer than those found in the inner region.

Unlike the annulus region which resists loading directly, the nucleus responds to applied load through an internal increase in hydrostatic pressure and transfers this pressure load to the surrounding tissue, namely the annulus and the cartilage endplates [11, 18]. This type of loading is shown in Figure 2-9. As a whole the annulus fibrosus has the capability of withstanding sizeable compressive loads. [18]
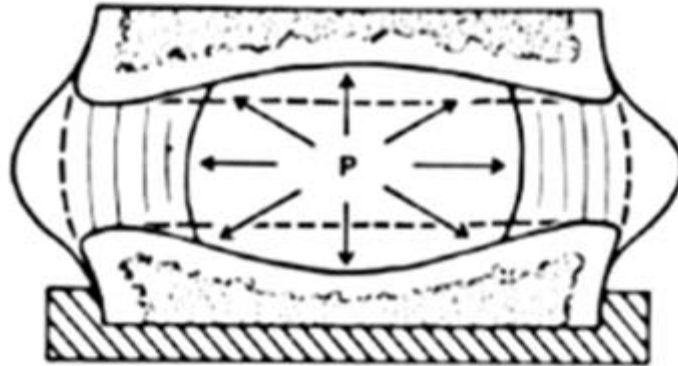
Figure 2-9: The hydrostatic pressure 'P' generated in the nucleus during purely compressive loading of the intervertebral disk. Notice how the outer annulus layers bulge under the compressive load. Adapted from White [11]

An accurate spine model must be able to account for these biological mechanical characteristics. Modeling bone as anisotropic material assignment would be inefficient if a highly detailed geometry is used, consequently the cortical and cancellous bone could be modeled as transverse isotropic. The annulus fibrosus should be modeled to reflect what is seen naturally, namely a less stiff inner layers relative to the outer layers. The nucleus should be modeled as an incompressible or nearly incompressible material to remain analogous to a pressure vessel.

2.1.3 Selected Mechanical Loading Conditions and Intervertebral Disk Response

While the vertebral bodies themselves do absorb a large proportion of body weight, it is the intervertebral disk and other ligaments which aid in the transmission of the load to the lower vertebrae as well as provide resistance to excessive spine motion. In addition, with the intervertebral disk being less stiff when compared to the vertebral bodies, its deformation and response to various loading conditions provides an excellent indicator of how computer generated models compare to the physiological case.

In purely compressive loading, the annulus resists the load in two different ways. Resistance is provided through the relative rigidity of the collagen fibers. However, to maximize the tensile strength found in the collagen fibers, the annulus also bulges in the radial direction during compression thereby stretching the embedded collagen fibers allowing for additional resistance against compression. This bulging behavior can be seen in Figure 2-9. As expected, the greater the compressive loading, the greater the collagen fibers resistant to the applied load. The intervertebral disk nucleus also aids in load resistance. The internal pressure of the nucleus increases with load, subsequently increasing hoop stress being applied to the annulus and the vertebral endplates with minimum deformation to the nucleus itself. The hoop stress generated by the nucleus does not result in greater annulus radial bulge as these stresses tend to decrease as the distance from the nucleus increases. The combined response of the annulus and the nucleus allows the intervertebral disk to withstand a great deal of compressive load. [11, 18]

Another common loading condition is bending. In such instances, the disk adopts a more distinct 'wedged' profile when viewed laterally. An example of this can be seen in Figure 2-10. On the region where the disk is undergoing the greatest compressive load, annulus bulging is evident, while the opposite side often has little to no bulging. Instead, the annulus layers on the lower compressive load side tend to bunch together more tightly to better resist the slight increase in tensile load. The nucleus in all bending directions responds in the same manner as if the load were purely compressive. Due to the collagen fibers natural slack,

resistance to bending is relatively low during the first few degrees and increases as the bending load increases. A sketch of the different stretched levels of the collagen fibers can be seen in Figure 2-11. In extreme cases, the tensile force resulting from bending often overcomes the natural compressive forces resulting in one side of the disk undergoing tensile loading. Because of the range of motion available to the vertebral column, the disk resists extension (leaning backwards) greater than flexion (leaning forwards). [11, 18]
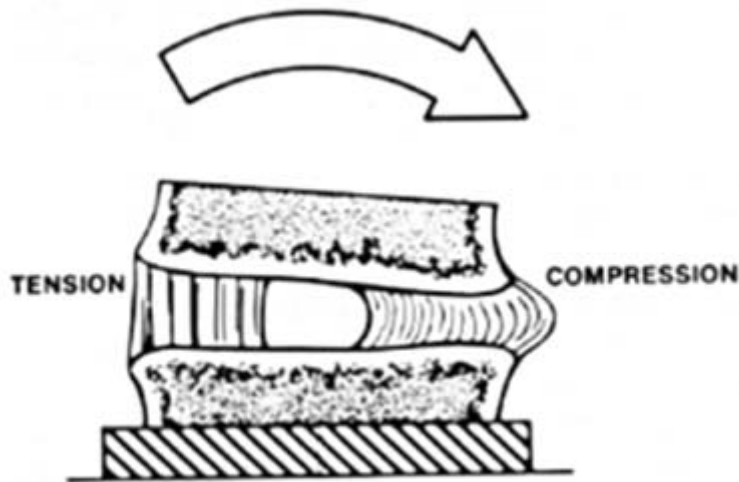
Figure 2-10: The intervertebral disk placed under high bending loads. The annulus fibers in the tension side are responsible for resisting the bending motion. Adapted from White et al. [11]
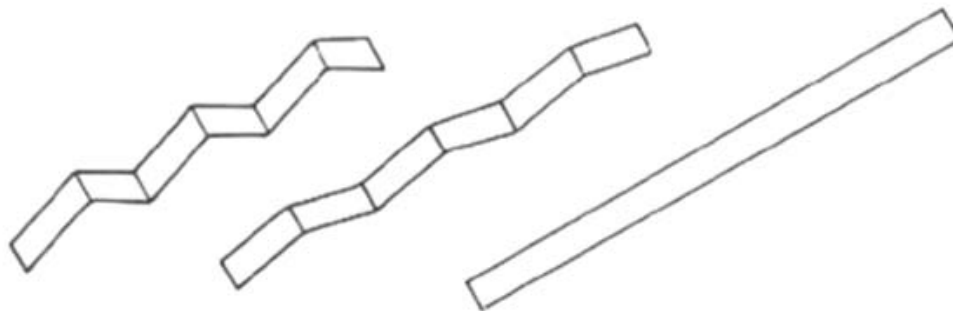
Figure 2-11: A sketch of the collagen fibers within the annulus. The far left image displays the fiber's length at rest. The middle image displays the fiber when placed under moderate loading while the right image shows the maximum stretched length of the fiber. Adapted from Ghosh et al. [18]

Physiologically, the disk rarely undergoes pure compressive, bending or torsional loading and is often subjected to combined loading. Under normal circumstances, failure of the disk is due to this combined loading as opposed to a single loading type.

In addition to the behaviors mentioned above, the disk also exhibits visco-elastic and other time dependent properties. Fluid flow between the nucleus, annulus and surrounding tissue is highly regulated and even with prolonged loading; water content loss in the disk is only about 10%. With the removal of the load, any expelled water is recuperated evenly. In the event that prolonged bending load is applied, the uneven fluid flow within the disk results in a temporary wedged disk profile even when the load is removed. Given enough time however, the disks original shape will return. This fluid flow results in creep within the disk which in turn affects the mechanical characteristics of the disk. Disks which have undergone creep tend to be stiffer in compression and recover from additional deformations more rapidly. However, these disks also tend to exhibit reduced resistance to bending. [11, 18]

When applied to spine biomechanics models, particularly for scoliosis research, static loads are of greater interest. Consequently, accurate spine models utilized in scoliosis research should be able to respond accurately to the most dominant type of spine loading: axial compression.

2.2 Bone Growth Behavior

There are several different ossification centers within the vertebral body itself as stipulated by White [11] and show in Figure 2-12 below. These centers are regions where bone growth occurs within the vertebra itself. While these ossification centers are agreed upon, there has been great debate regarding bone growth behavior in regards to whether significant growth occurs at the endplates of the vertebra or along the entire vertebral body. Researchers such as Lin et al. [19] support the theory that growth occurs only on the endplates of the vertebra while others, such as Adeeb et al. [20] suggest that bone growth occurs along the entire vertebral body. This study will assume that bone growth occurs along the entire vertebral body.
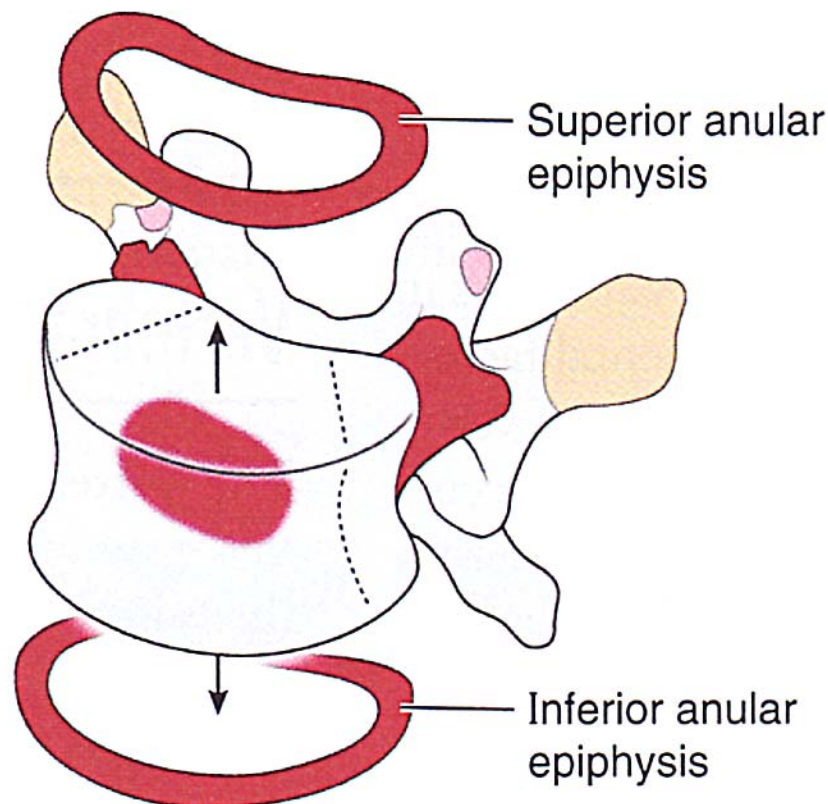
Figure 2-12: Theorized ossification centers of the vertebral body (shown in red). Adapted from Moore [14]

2.3 Scoliosis

2.3.1 Definition and Treatment

A healthy spine adopts a slight 'c' shaped curve in the thoracic region when viewed in the sagittal plane while along the frontal plane there is little to no curvature (Figure 2-13a and Figure 2-13b) with the exception being a slight right thoracic curve, theorized to be due to aorta position [12]. Scoliosis is defined as the abnormal three dimensional curvature of the spine with the most prevalent curvature seen in the lateral direction (Figure 2-13c) [11-12, 21]. Should the curvature become severe enough, noticeable deformation of an individual vertebra can occur as demonstrated in Figure 2-14 [11].

(a)   (b)   (c)

Figure 2-13: Sagittal (a) and coronal (b) viewing plane of a healthy spine. [22]; (c) coronal viewing plane of a spine suffering from scoliosis. [23]
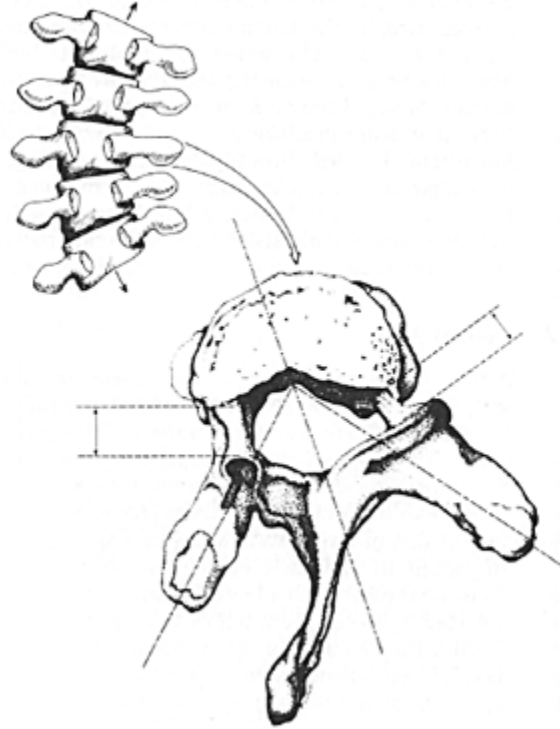
Figure 2-14: A severe case of scoliosis which results in deformation of the vertebral body and posterior elements. Notice the differences of this vertebra compared to that of Figure 2-1. Adapted from White et al. [11]

A common means of clinical measurement of scoliosis curvature is the 'Cobb' angle which determines the angle between the two vertebral bodies that are suffering from the greatest amount of tilt (Figure 2-15). While there is no set minimum curvature limit for scoliosis, there is a general agreement that a spine is designated as 'scoliotic' when this lateral spine curvature exceeds a Cobb angle of 10° [24].
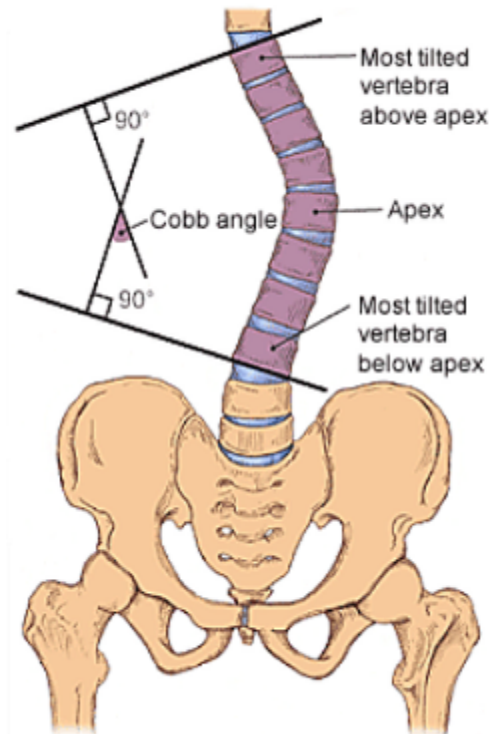
Figure 2-15: Cobb angle measurements of a scoliotic spine [25]

There is evidence to suggest that genetic traits are inherited although no discernable pattern is observed [10, 11]. However, there is a higher prevalence of the condition in females [24]. The most common type of scoliosis curvature is in the thoracic region of the spine.

With little information on the cause of scoliosis, treatment is difficult. In many cases, scoliosis curves progression can suddenly halt resulting in spines with small Cobb angles. In these instances, no corrective measures are taken and only careful observation is needed to ensure there is no subsequent curve progression. In cases where the spine curvature continues to progress however, additional corrective measures such as mechanical bracing is often employed. Braces such as the Milwaukee Brace or Boston Brace serve to apply mechanical loads to the spine to prevent further asymmetric growth. In the extreme cases

where such procedures are ineffective or if the patient so desires, corrective surgery can be considered, resulting in the implantation of metal rods to prevent further spine curvature.

2.3.2 Common Scoliosis Cause and Progression Theories

Several theories regarding the cause of scoliosis have been put forth, all of them attempting to address the mechanics of the condition. Roaf suggested that scoliosis is caused as a result of an increased growth rate of the anterior spine components compared to the posterior elements. As the body cannot sufficiently accommodate the rapid increase in vertebral body growth due to the confinement of the abdominal muscles and other organs, the spine is forced to grow in the lateral direction, thus developing into scoliosis. [26]

MacEwen put forth that scoliosis was caused not by mechanical loading, but a result of the loss of sensory input. By monitoring the electromyographical activities of the deep dorsal muscles in the spine, MacEwen found that patients with progressive scoliosis consistently showed increased muscle activity. By severing the dorsal nerve roots MacEwen was able to induce scoliosis in several animal studies with the curve concavity occurring on the side with the damaged nerve. This in turn causes an asymmetric muscle load force placed on the spinal column. [27]

Sevastik et al. [28] suggested that asymmetric growth of the thoracic ribcage in some cases can result in idiopathic scoliosis. This type of asymmetric growth would stimulate axial growth of the underlying costosternal cartilage of the spine which would alter the balance of spinal forces [28]. Pal also agreed with

this theory and suggested that the progression of scoliosis could be stopped by removing one rib from the 'heavier' side of the body [29].

Van der Plaats et al. [10] built upon asymmetric loading as a cause behind the initiation of scoliosis and looked at one of three different modes which would cause asymmetric loading: buckling, abnormal or delayed growth of muscles, and abnormal or delayed growth of ligaments.

Recently, one of the most popular theories regarding the contributing factors of scoliosis lies with asymmetric loading of the spine. This has given rise to Dr. Stokes' theory of a 'vicious cycle' shown in Figure 2-16 [30]. It is believed that scoliosis spines tend to undergo greater loading on one side of the spine. Consequently, the area of the vertebral body which is undergoing greater load tends to grow slower than other areas. This asymmetric loading results in asymmetric growth of the vertebra which in turn prompts continued or increased asymmetric loading [31-33]. This progression continues until the asymmetric loading somehow halts. This is however, an explanation of progression as opposed to initiation.
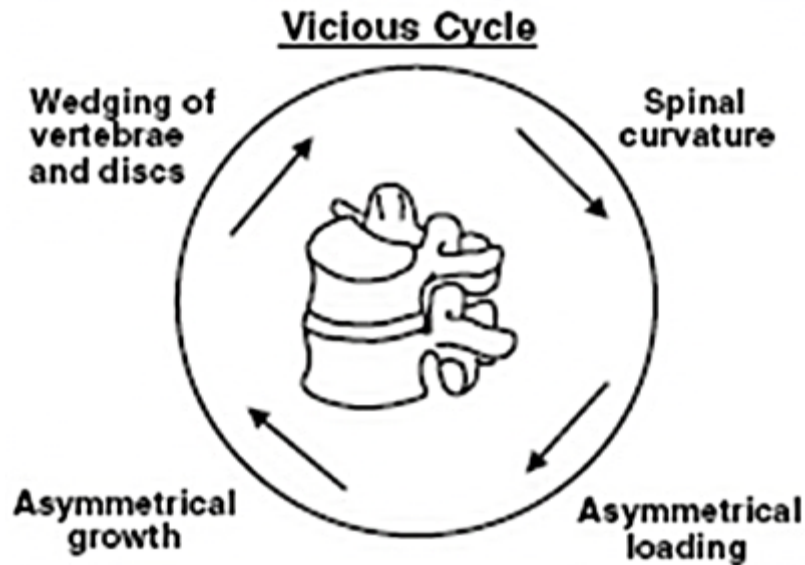
Figure 2-16: The 'vicious cycle' theory of scoliosis progression suggested by Dr. Stokes [31]

2.4 Scoliosis Treatment Complications

Despite the fact that scoliosis is a well documented condition, there is no general agreement into the cause of the deformity and treatment responses have all been reactionary in nature. For example, bracing is only used only after the curve proves to be progressive instead of working towards stopping potential spinal curvature before a high Cobb angle is reached.

In order to improve treatment so it is preventative in nature, there is a strong need to predict the progression of the deformity. In doing so, it will allow researchers and clinicians to identify which scoliosis patients will suffer from progressive curvature growth and provide the appropriate treatment as quickly as possible, improving the quality of life of the patient as well as reducing health care costs.

Such scoliosis growth model predictors can also aid in the understanding of the condition and provide insight into the progression of scoliosis and

determining what factors, such as loading conditions, geometry or material properties cause progressive and non-progressive forms of the condition. This study seeks to improve upon asymmetric spine growth models currently developed by other researchers by providing a more physiologically accurate spine model through the use of finite element analysis.

Chapter 3
Finite Element Analysis Theory

Finite element analysis (FEA) has been regularly employed to determine not only the biomechanics of the spine, but scoliosis growth patterns as well. Previous scoliosis models however were limited by the scope in which the FEA was applied due to geometric idealization or the application of coarse meshing.

This chapter focuses on the theory of FEA and how the choice of meshing or application of material properties can alter the way a model reacts. In addition, there will also be a discussion as to why FEA is employed in studies of complex biological systems like the spine. Element types utilized in this study, as well as a brief discussion of the different types of elements used in other studies will also be looked at. A section regarding the effects of mesh density on finite element models will also be discussed.

3.1 Finite Element Method (FEM)

FEM is a type of numerical solution. The basis of this technique involves the representation of a body by a series of discrete divisions known as elements. Instead of solving a region with an infinite number of degrees of freedom (DOF), FEM divides the region into elements with a finite number of DOF, allowing for a solution to be calculated. These elements are then connected together by enforced and shared boundaries (nodes). Mathematical approximations that provide a shape of the desired variable are then made. By combining the equations of each element, the overall behavior of the entire domain can be established. The following section provides more detailed FEM explanations.

3.2 Finite Element Method Theory

In engineering, material behavior is most often characterized first by a difference equation which is then transformed into a differential equation, be it partial or ordinary. The solution to the partial differential equation (P.D.E.) is known as a "strong form" solution. A strong form differential equation, such as the example shown in equation 3-1 requires that the solution function satisfies all points of the differential equation. As such, should there be any instance where the function is not valid at a single point, the solution cannot be considered. Should there be a discontinuity in the function, two different strong form equations are required; one before and one after the discontinuity. In summary, the strong form equations provide an exact solution to the governing differential equation for a given function. [34]

$$\frac{\partial^2 u}{\partial x^2} = -\frac{cx}{EA} \qquad \textbf{3-1}$$

Note that 'u' is the function for which a solution is required, be it linear or nonlinear.

Weak form equations, as shown in equation 3-2, provide a solution which satisfies the function in a general sense by ensuring the error reaches a minimum. As the solution of the weak form might not satisfy the strong formulation at every point, it is easier to solve, and is capable of handling function discontinuities without the need of additional solutions. [35]

$$\int_0^x \left(\frac{\partial^2 u}{\partial x^2} + \frac{cx}{EA} \right) f_1(x) dx = 0 \qquad \textbf{3-2}$$

The function $f_1(x)$ is a piecewise linear function which approximates the solution function over the domain while the terms in the brackets is termed the residual. Over the entire domain, the weak form solution can take the form shown in equation 3-3.

$$u = \sum a_i f_i(x) \qquad\qquad \textbf{3-3}$$

Where, the 'a' is the magnitude or intensity of the solution. In order for the solution to reach a minimum as required for weak form equations, the integral displayed in equation 3-2 is made equal to zero.

Finite element analysis involves dividing the solution domain into smaller sections termed 'elements' and approximating the domain using certain shape (linear or non-linear) functions as shown in Figure 3-1. The greater the number of elements utilized in the function, the higher the accuracy of the weak form (numerical) solution. [34]
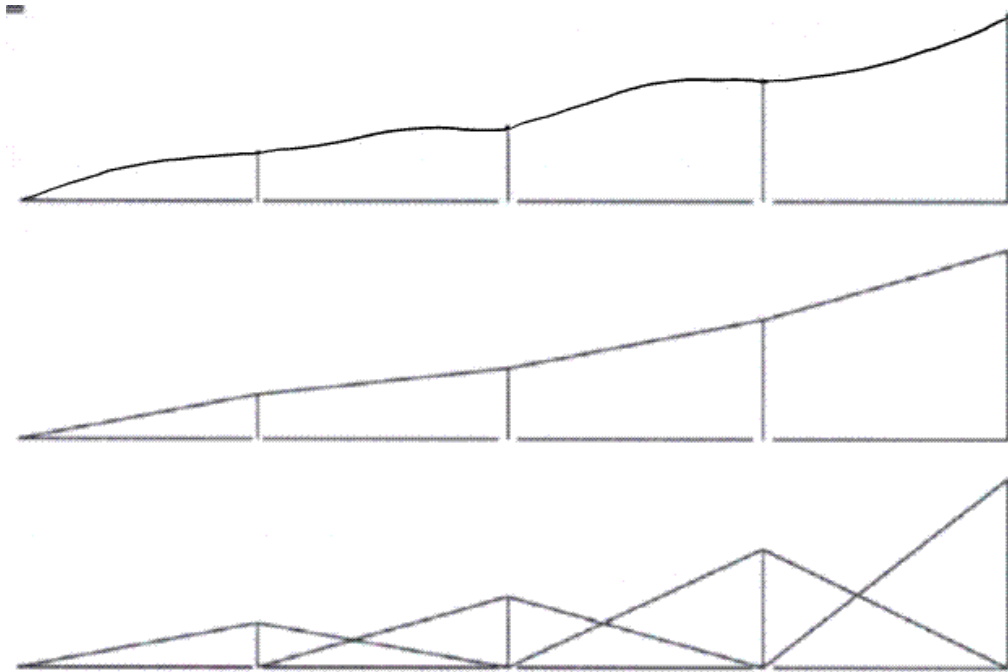
Figure 3-1: Element formulation (bottom) and linear piecewise approximation (middle) of an exact function (top). Notice that the elements form linear piecewise approximations of the exact function. Adapted from CivE 665 lecture notes [34]

It can seen from Figure 3-1 that a large element size with a finite number of nodes will be required to produce an 'average' or 'best fit' response across the entire element domain. This can result in a loss of detail and reduce the accuracy of the model. By replacing a single large element with multiple smaller elements possessing the same number of nodes will provide a far more accurate representation of the domain's behavior. This comes at the cost of increased model complexity as the introduction of more elements results in the increase of equilibrium equations. [35]

3.3 Element Type Considerations

It has been established that the number of elements utilized within a domain is critical; however, the type of elements used is also important in order to best characterize the underlying geometry of the model. When modeling three

dimensional objects, there are several different types of elements commonly in use: tetrahedral (four node elements) or hexahedral (eight node elements). While both of these element types are capable of modeling irregular geometry, they are limited in that the element edges between the nodes are straight and cannot bend. This limits their application in biological structures such as bone where the surface structure is composed of curves. Consequently higher order tetrahedral (ten node) or hexahedral (twenty node) elements are created by placing a 'mid-side' node thereby allowing the element edges to curve, better matching the underlying geometry. Figure 3-2 illustrates an example of a standard tetrahedral element and a higher order tetrahedral element.

(a)   (b)
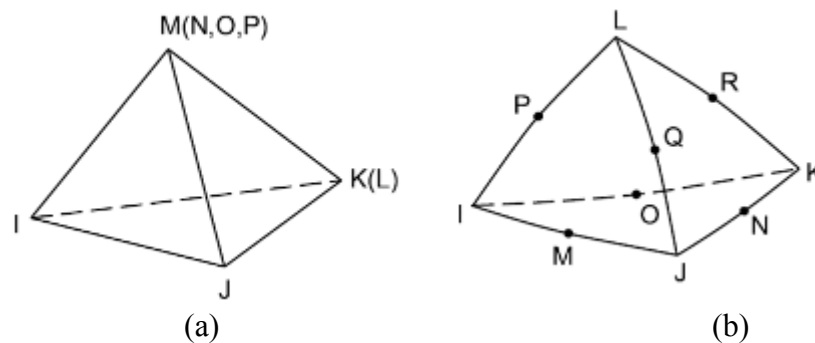
Figure 3-2: (a) a standard four node tetrahedral element and (b) a higher order ten node tetrahedral element. Notice how the presence of a midside node allows for the linear edges of the element to change slope, creating a non-linear boundary, adapted from Ansys help files [36]

There is no specific guideline to determine the number, type or size of the elements used for the FEM. However consideration must be made to ensure that the resulting solution will provide an accurate representation and that further mesh refinement will not provide any model improvements.

3.4. Mesh Density Considerations

As discussed previously, an increase in the number of elements (a finer mesh/increased mesh density) results in a more accurate representation of a domain solution. A demonstration of this effect can be seen in a mesh convergence study. A simple beam with a single end fixed and a 100N load applied to the farthest edge is meshed with variable mesh density and the overall displacement of the beam calculated using FEA. The results can be seen in Figure 3-3.

(a)   (b)
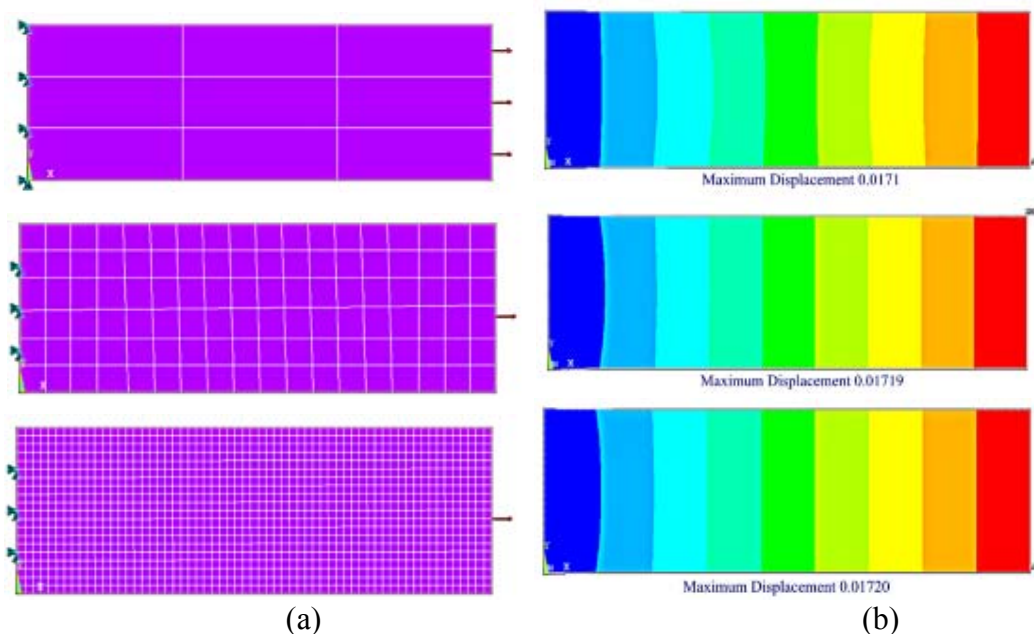
Figure 3-3: (a) The same beam with different mesh densities under identical loading conditions. The top image displays a coarse mesh, the middle displays a medium mesh and the bottom image displays a very fine mesh. The left surface of all three images are fixed in all directions and a 230MPa pressure load applied to the right surface of the beam (b) The corresponding horizontal displacements seen in the beams due to loading

As can be seen from the Figures, as the mesh density increased so too did the maximum displacement of the model. As Figure 3-4 displays however, this increase will not be infinite. By fitting a best fit line though the data points a trend can be seen.
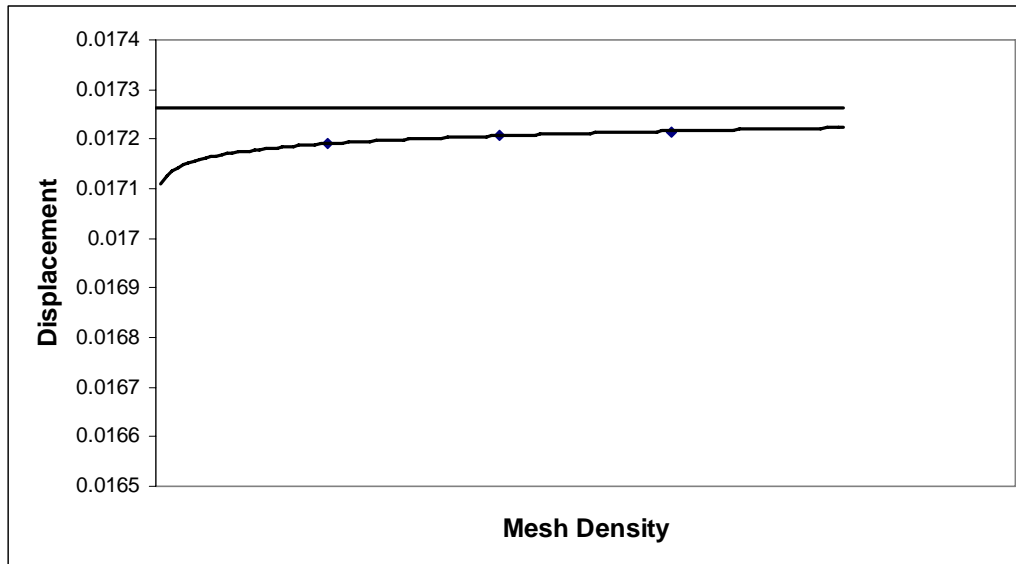
Figure 3-4: A graph displaying the relationship between displacement and increasing mesh density, a predictive trend-line has been fitted to the data points to plot a potential pattern. The straight line indicates the theoretical solution as calculated using Castigliano's Theorem, an energy method

With the x-axis representing a progressively increasing mesh density, it can be seen that the coarse mesh provides a value deviation of 0.417%, the medium mesh density 0.307% and the fine mesh density a value of 0.272%.

From the graph it is clear that at a certain point, the total model displacement will be constant, regardless of the number of elements and the mesh density. This point is termed as 'mesh convergence'. While increasing the mesh density may potentially yield a more accurate value it can significantly increase processing time depending on the complexity of the model, making such models impractical to use; a justifiable balance between convergence and computational time must be made. In this particular example, the effect of an increasing mesh density is negligible as a high mesh density does not provide significant improvements in displacement results and as such, a coarse mesh would be sufficient.

There are also additional considerations that must be made in regards with mesh density and the applied loading conditions. Notice that as the mesh densities of the beam increases, it appears that the colored band nearest to the fixed end, namely the blue region, begins to curve. Recall that the left surface of the bar is fixed in all directions, meaning that while the remainder of the bar width is allowed to shrink in accordance with Poisson's ratio, the surfaces nearest to the wall is not able to as they are fixed, resulting in an inaccurate deformation distribution as well as stress distributions. These inaccuracies are further exacerbated by increasing the mesh density. In this particular case, this error can be eliminated by changing the loading conditions such that the left surface is restrained from any motion along the horizontal plane only.

As can be seen, considerations regarding mesh density, the types of elements utilized and the number of elements used in any FEA must be made in order to ensure that utilized computer solvers are able to solve the given problem with acceptable accuracy under reasonable time constraints.

Chapter 4
Literature Review

While there has been little progress in regards to understanding the cause of scoliosis and how to best treat the condition, there have been significant steps taken in modeling scoliosis growth. In this section, past work on spine and scoliosis growth finite element models will be reviewed with particular focus on individual capabilities and limitations. Not all of the finite element models discussed are used for scoliosis growth models. These studies however, can provide valuable information regarding the use of FEA software to evaluate spine biomechanics. Included in this chapter's discussions are material properties, geometry creation techniques and physiological accuracy, assumptions made and their limitations.

4.1 Finite Element Spine Biomechanics Studies

Although current studies into spine biomechanics do at times utilize geometrically accurate spine models with physiologically similar material properties, many current scoliosis growth models do not employ such detail. Consequently, in order to create a spine growth model that is physiologically accurate, it is first necessary to ensure that the created geometry responds to loading conditions in a similar manner to the natural spine. The following studies are unrelated to scoliosis research but provide a basis of how to properly create a spine model that is comparable to a natural healthy spine.

4.1.1. Image Acquisition Techniques/Base Geometry Creation

Maintaining correct spine geometry plays a critical role in modeling as the inclusion or exclusion of particular geometric features can alter the stress distribution within the vertebra due to stress concentration factors or stress redistributions. Currently, there are a variety of different methods in which spine models are created; the most common being the use of computer tomography (CT) images. Studies conducted by Chiang et al. [2], Sairyo et al. [3], Goto et al. [4], Lee et al. [5], Totoribe et al. [6], Li et al. [7] and Schmidt et al. [8-9] all utilized CT images to create a FSU of the lumbar spine. This technique allowed for all studies to utilize patient data as a basis for the FSU geometry creation, providing an anatomically accurate model. The model developed by Schmidt in particular demonstrates the effectiveness of utilizing CT images as a basis for geometry creation as shown in Figure 4-1 below.
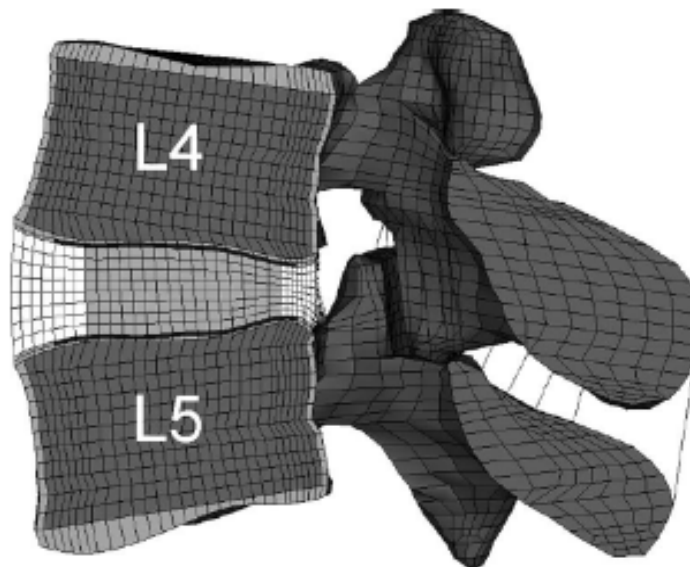
Figure 4-1: The finite element model utilized by Schmidt et al. Notice the high degree of geometric detail in the spine model

Despite the inherit advantages of utilizing CT images to create spine geometry there are several disadvantages that can result in a loss of geometric

quality. A common limitation is the use of relatively thick CT image slices. Studies conducted by Goto and Totoribe for example utilize CT slices of 2mm, a thickness that is nearly 10% of the total vertebra height (usually 28 to 30mm) [37-39]. This thickness resulted in a loss of geometric data which reduces the physiological accuracy of the model. Studies conducted by Sairyo and Lee on the other hand utilized small CT image slices but assumed vertebra symmetry either about the sagittal line or the transverse plane. Both assumptions reduce the accuracy of geometric models.

An alternative to CT images is to create the vertebra geometry manually. This is either done by selecting key landmarks on the vertebral body and connecting them using a series of spline or quadratic lines as Little et al. [40] did, or by approximating the vertebral body shape using idealized geometry such as Yao et al. [41] and Denozière et al. [42]. These methods of FSU geometry creation allow for rapid model assembly and reduce the complexity of the model in general. However these models do not take into account the unique shape of vertebra and when combined with some of the symmetry assumptions discussed above, these particular models lose a great deal of geometry data.

Neglecting unique vertebra features such as the concave lateral profile or the concave superior/inferior surface of the vertebral body can weaken the patient specificity and the clinical applicability of the model.

4.1.2 Selection and Allocation of Material Properties

Proper allocation of model material properties is as vital as geometry in the development of an accurate FSU. As previously discussed, bone is best modeled as an anisotropic slightly visco-elastic material while the disk itself is a

heterogeneous visco-elastic material. Modeling anisotropic materials in computer software however can be difficult; and consequently, simplifications are often made.

If analyzed in small sections, bone can be idealized as an isotropic, linear elastic material, a property that is often expanded to the rest of the vertebral body. Little [40], Chiang et al. [2], Sairyo et al. [3], Goto et al. [4], Lee et al. [5], Totorbie et al. [6] and Li et al. [7] all utilized isotropic linear elastic material properties for the cortical and cancellous bone regions. An improved representation of bone mechanical characteristics would be to model it as transverse isotropic as Yao et al. [41] and Schmidt et al. [8-9] have done. Denozière et al. [42] modeled the vertebral body with heterogeneous isotropic material properties since the center of the vertebra endplate are softer than the outer rim.

The behavior of the intervertebral disk is also critical in accurately evaluating the behavior of a FSU. The disk should be modeled as two distinct regions: the annulus fibrosus and the nucleus pulposus.

The annulus fibrosus region of the disk is best described as series of fibers embedded in a nearly incompressible fluid. Studies conducted by Little, Yao, Chiang, Denozière, Goto, Lee and Schmidt, all utilize a composite annulus fibrosus design with fibers embedded in a ground substance. Researchers such as Sairyo however, assumed that the annulus fibrosus was a solid entity with no fibers. While the latter option improves computational speed, it does not accurately reflect the mechanical properties of the disk. Schmidt and Little further

improved upon intervertebral disk models by utilizing Mooney-Rivlin hyperelastic material properties for the annulus ground substance.

4.1.3 FSU Components

FSU are commonly modeled as two vertebras, an intervertebral disk, cartilage endplates on each vertebral body and ligaments. The exclusion of any of these components has the potential of altering the stress distribution of the modeled FSU, causing deviation between the model and a physiological setting. One of the most commonly neglected components in a FSU, as demonstrated by Little, Denozière, Lee, and Li, is the cartilage endplate. Currently, no studies have been conducted to determine the effects of neglecting the cartilage endplates in FEA.

A far more critical exclusion in a FSU would be neglecting dual structural composition of vertebral body in cortical or cancellous bone. While Li chose to replace the cortical and cancellous bone with a single continuous entity with an 'adjusted' modulus, studies conducted by Cao et al. [43] and Eswaran et al. [44] demonstrate the important load sharing characteristics of the cortical and cancellous bone.

Ignoring the two unique components of the intervertebral disk can alter the natural biomechanics of the spine such as changing stress distributions within the disk. Li for example chose to model the disk as a single entity with a 'bulk' modulus while Goto and Sairyo chose to model the annulus region as a solid material as opposed to a gelatin substance with fibers imbedded within it.

While certain components, such as the posterior elements or muscle attachments can be ignored depending on their role in the study, components such

as the cortical and cancellous bone cannot be neglected without risking incorrect load response behavior. Neglecting certain components of the FSU is often done to reduce computation time and processor demands.

4.1.4 Model Meshing Density

A high degree of geometric accuracy utilizing CT scans as a basis can be rendered ineffective if the mesh density utilized in the FE program is too coarse. A coarse mesh, and consequently large element sizes, results in geometric simplifications between the actual geometry and the finite element (FE) model which is demonstrated in Figure 4-2 below.
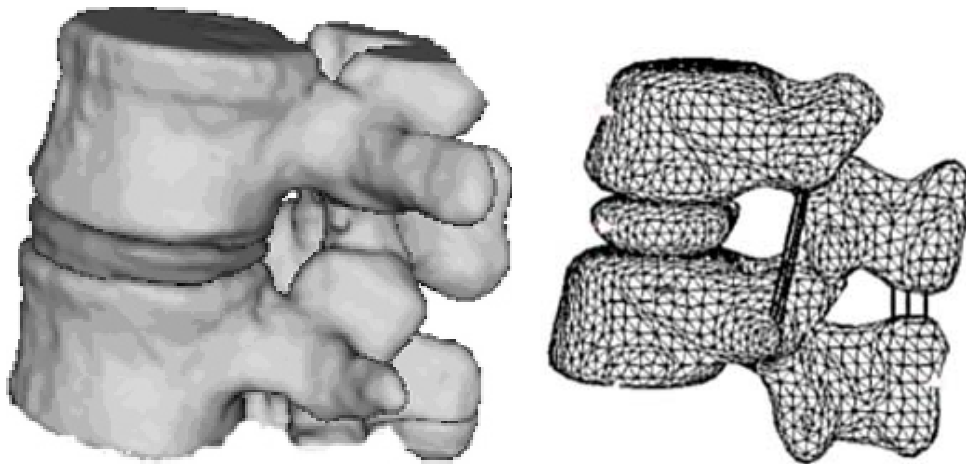
Figure 4-2: An example of a coarse mesh reducing geometric accuracy, the model developed by Li [7] on the left is the original geometry taken from CT scans and the same model seen on the right is the FE model with a coarse mesh

As can be clearly seen, a low mesh density results in a great number of lost geometric data, even if the underlying geometry utilizes highly accurate CT scans as a basis. For example the intervertebral disk now appears to be more elliptical in shape as opposed to cylindrical as shown in the CT image and the vertebral bodies no longer have a concave lateral profile. The use of a coarse mesh, as well as incorrect allocation of disk material properties may have resulted

in differences in disk bulging from in vitro studies conducted by Heuer et al. [45]. Studies conducted by Chiang, Goto, Totoribe and Li all suffered from the use of low element count which reduces the accuracy of their models. It should be noted that while model accuracy may be reduced with such a low element count, computational time is greatly decreased and the demands on the processor decreasing significantly. Comparing the model created by Schmidt (Figure 4-1) with the one done by Li, it can be seen that a higher number of elements ensures that the FE model maintains the original CT geometry more effectively.

4.2 Finite Element Scoliosis Growth Models

Current scoliosis models are capable of simulating scoliotic curves with limitations. Some of the more common limitations of current scoliosis growth models are the lack of geometric detail, low mesh density and/or inappropriate material property definition. Idealizations in geometry or material properties are made due to the need by researchers to model the entire or large sections of the spine. Should physiological detail be maintained in such models, the processing time and computational power required would increase significantly. Consequently, a balance between the two must be made. Models developed by Villemure et al. [32, 46], Lafortune et al. [33], Van der Plaats et al. [10], and Stokes [30-31] all demonstrate how idealized geometry is often employed. In these instances, individual vertebra are often simplified as either a single beam element, a 'wireframe' model arranged in an octagonal format (Figure 4-3) or just as a solid cylinder (Figure 4-4). The intervertebral disk is also often simplified by modeling them as a spring or beam elements with no distinction between the

annulus fibrosus or the nucleus pulposus. While the disks themselves do not affect bone growth directly, if they are not properly defined there is a chance that the intervertebral disks will not transfer vertebral body loads correctly. In other cases, the intervertebral disk is completely ignored, as studies conducted by Stokes show. This can affect the response of the spine to loads, causing an inaccurate representation of the spine.
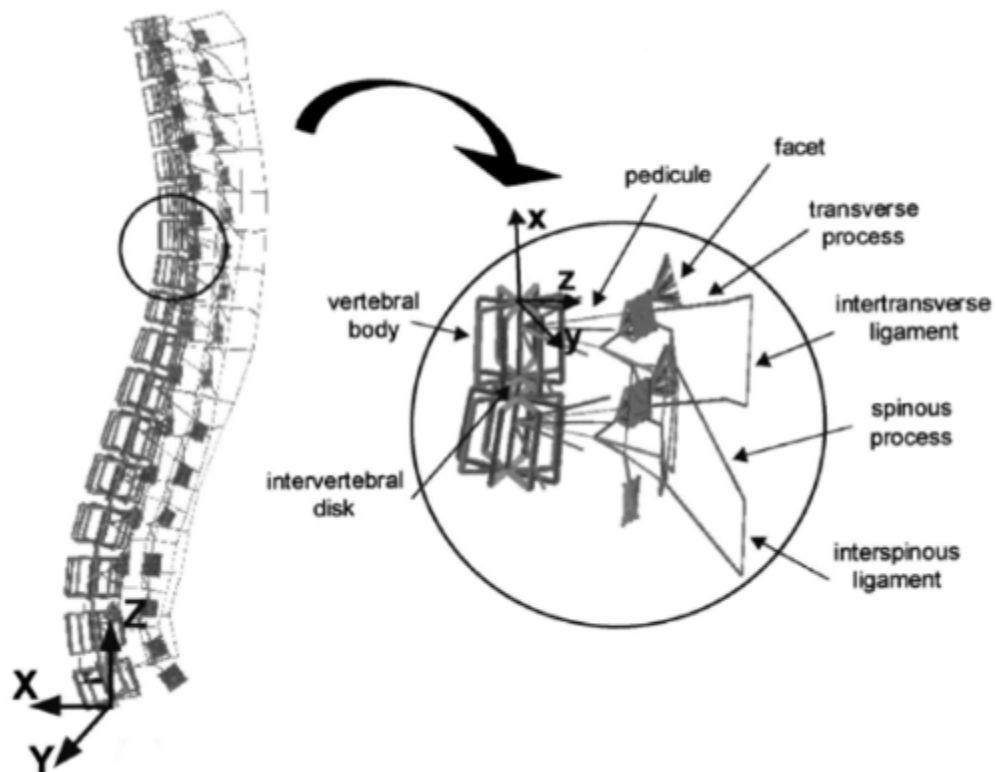
Figure 4-3: An example of a wireframe spine model utilized by Villemure, Lafortune and Van der Plaats. Adapted from Villemure [32]
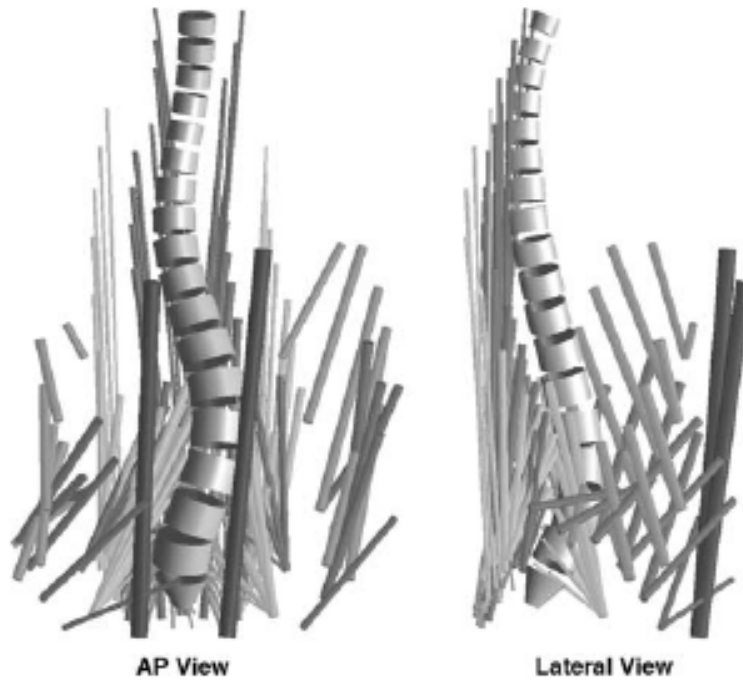
Figure 4-4: An example of the cylindrical spine model utilized by Stokes. The long slender cylinders are modeled ligaments [30]

There are studies however, that attempt to construct geometrically accurate models. Azegami et al. [47] and Goto et al. [48] for example, utilized radiograph images of the spine to create a three dimensional computer model of not just the spinal column but the attached ribcage as well. These advances in geometric accuracy however, are somewhat mitigated by the low mesh density used, resulting in the loss of geometric detail. Figure 4-5 displays an example of the spinal column developed using radiograph images.
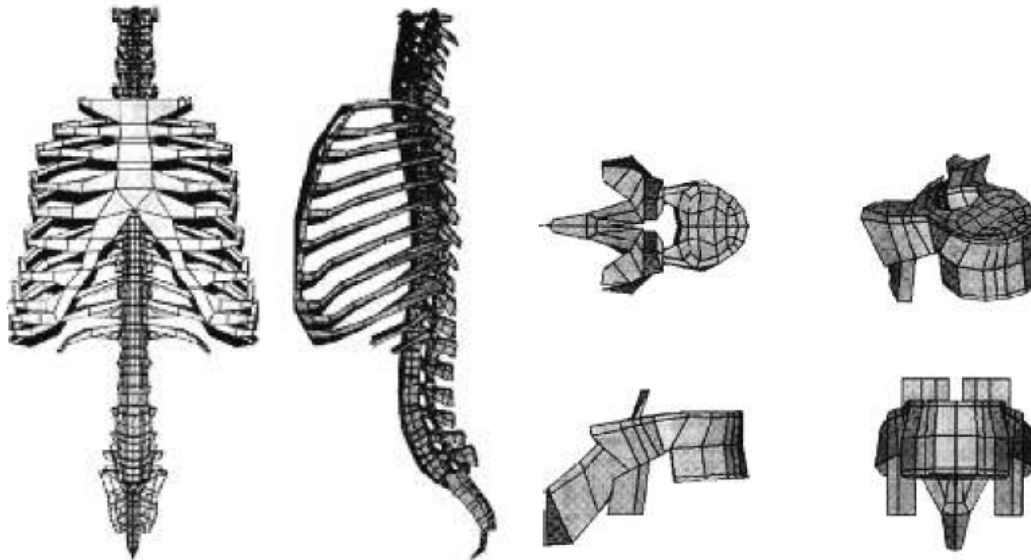
Figure 4-5: Radiograph based FE spine models. The left image displays the entire spinal column modeled by Azegami [47] while the right image displays a single vertebra. Notice how a low mesh density results in the loss of geometric detail

In addition to geometric limitations, current spine models also suffer from the inappropriate definition of material properties. Many models, such as the ones developed by Villemure and Azegami assume linear isotropic cortical and cancellous bone properties. Other studies such as those by Van der Plaats utilized a single bulk modulus of the vertebral bodies. The intervertebral disks were also commonly inadequately modeled and were often assigned a single 'bulk' modulus that was an average value of the entire disk.

A variety of different elements have been used to model the spine in FEA programs. For the vertebra itself, researchers have used elements ranging from a linear eight node brick elements to a more complex twenty node quadratic brick elements. When modeling biological tissues however, quadratic tetrahedral elements are more often employed due to their increased ability to model irregular geometry [41].

Since modeling the cancellous bone as a porous type material as discussed in Chapter 2 is a difficult procedure, certain researchers have introduced the use of 'void' elements [5]. Most often used to model soil, void elements specify the ratio of open spaces or gaps to solid material. The Mooney-Rivlin formulation is sometimes used to model the 'fluid-like' properties of the intervertebral disk [8-9]. Commonly referred to as a hyperelastic material, Mooney-Rivlin material properties provides a non-linear relation between stress and strain in a material that is capable of undergoing large deformations. Generally such materials possess an initial linear behavior before reaching plateau in the stress strain curve due to the release of heat energy. After a certain point the elastic modulus will continue to rise. More commonly however, the cancellous bone is assumed to be a solid entity and the assigned material property adjusted to reflect the porous nature of the bone.

4.3 Requirements of Physiologically Accurate Scoliosis Growth Model

Current growth models have effectively demonstrated that FEA software is capable of modeling scoliosis progression. Models such as those developed by Villemure, Lafortune and Stokes demonstrate how asymmetric loading can cause scoliosis while Azegami, Goto and Van der Plaats showed how buckling is the source of the progression. Regardless of the theory behind the initiation of scoliosis, all current spine models lack the appropriate physiological response to loading due to simplified geometry and material property assignment. These simplifications limit current models capabilities in a clinical setting.

In order for scoliosis growth patterns to be adequately modeled so they are applicable in a clinical setting, they must:

- Possess geometric accuracy as can be achieved by using CT images or some variation of this as a basis;

- Include all relevant functional spinal unit components. This includes a cortical and cancellous bone component, an appropriately modeled annulus fibrosus and nucleus pulposus. Ligaments, muscle attachments, posterior elements of the vertebra and the inclusion of a ribcage on the spine model can be excluded only if they will have no bearing on the scoliosis theory being studied; and

- Have appropriate assignment of material properties on all components of the spinal column. Cortical and cancellous bone should be modeled as anisotropic if the data is available, otherwise it should be modeled as transverse isotropic. The annulus fibrosus should be modeled as a composite element with appropriate fiber orientation while the nucleus pulposus modeled as an incompressible or nearly incompressible solid.

Only when these conditions are met and their physiological response to loading behavior validated by comparing them with available literature, can the model be applied to scoliosis growth models that utilize the 'vicious cycle' theory. As the vicious cycle theory is directly dependent on the stress levels within the vertebral bodies, it is critical that the spine components respond in a physiologically accurate manner in order to properly utilize the vicious cycle theory.

While these conditions will ensure accurate results in FE studies, the added level of detail can significantly increase the processing time and computation power required.

Chapter 5
Spine Biomechanics Model Development and Validation

Currently, finite element analysis can be used to model the complex geometry and accurately simulate natural spine biomechanics. Despite this, there are currently no physiologically accurate spine models designed specifically to test the vicious cycle scoliosis theory. This section will detail the procedure undertaken in the development of a biomechanically accurate spine model for the use in scoliosis research. Validation through comparison with literature values include: disk displacement under loading, disk bulge under loading, stress distribution throughout the intervertebral disk, stress distribution throughout an individual vertebral body as well as total displacement of a single FSU under varying loads. Additional studies will include the effects of the cartilage endplate on the model as well as the effects of mesh density.

5.1 Modeling Assumptions

Ideally, it would be desirable to create a finite element model which is patient specific so any results can confidently be applied to the patient without fear of adverse physiological conditions that could potentially render the calculated results inadequate. However, given the current technology, there are several factors which limit the use of patient specific modeling in both clinical and laboratory settings.

The first is the time required to generate a geometrically accurate spine model. This process involves scanning each individual, transforming the two

dimensional images into three dimensional models and then importing the models into FEA software for load application and analysis. As this entire process is extremely time consuming, until custom software is designed to incorporate all the steps into one program, patient specific geometry is simply not feasible.

The amount of processing power available is also a limiting factor. While supercomputers have aided, a great deal of time is still required to solve complex models, particularly full vertebral columns if a highly detailed geometry and high element count is used.

Disk degeneration, osteoporosis, injuries or other such conditions can dramatically affect the physiological behavior of the spinal column under identical loads. Consequently if patient specific models are to be developed, material properties unique to each patient must be taken and applied to the model. This procedure would not only be time consuming but invasive and detrimental as biological specimens would need to be extracted from the spine so that appropriate testing can be conducted.

Finally, the type of loading varies between individuals. For a model to truly be patient specific, loading conditions and constraints must account for an individuals activity level, body weight and other such factors that can affect the type of loading seen by the spine.

Thus while FEA has yet to reach the technological stage where it can be applied to specific individuals in an effective manner, CT images can be utilized to provide a basis in which a generalized model can be built upon. Such models can then simulate results expected from the general population which can provide

researchers with an overall idea of what typical physiological response to loading should be.

5.1.1 Geometric Assumptions

Although previous scoliosis studies all model large sections, if not the entire spine, none of them possessed the level of geometric detail developed in this study, such as the presence of concave lateral profiles, kidney bean cross section and other such surface features. Consequently, due to limitations in processing power and time constraints, only a single FSU will be modeled. As a result, the simulation will be unable to calculate Cobb angle; however, should the application of the vicious cycle theory in this simulation prove to be successful, there will be evidence of vertebral body wedge, a characteristic that can be quantified and compared with literature.

In order to properly test the vicious cycle theory, all extraneous factors that can affect the vertebral body stress aside from asymmetric loading must be eliminated. This will ensure that differences in stresses within the vertebral body will only be due to loading conditions and not geometric factors.

To simplify the analysis the posterior elements are neglected from the model. While in some severe cases of scoliosis, the axial rotation of the spine causes growth deformities in the posterior elements of the spine (Figure 2-14: A severe case of scoliosis which results in deformation of the vertebral body and posterior elements. Notice the differences of this vertebra compared to that of Figure 2-1. Adapted from White et al. [11]) [11]; as only axial loading will be placed upon the FSU, the type of loading introduced in this analysis is not expected to affect the posterior elements of the spinal column. While it is possible

to evaluate twisting of the vertebral bodies, should posterior element distortion occur, it would be difficult to evaluate spinous process curving given standard x-rays.

As one of the principle theories behind this study is the presence of asymmetric loading about the midsagittal plane causing asymmetric growth, great efforts were taken to ensure that additional variables that could potentially skew the results are eliminated. As such, the FSU was assumed to be symmetric about the mid region. As the model geometry is based upon CT scans, to generalize the model, surface imperfections unique to the individual will be removed. In addition, the model will be smoothed to idealize the FSU. These two conditions would reduce the likelihood of higher stresses in one region of the vertebra due to geometric effects unique to the individual.

While it is possible to create a variable thickness cortical bone with CT images, this wall thickness will be unique to the individual. As such, a constant thickness cortical shell was used as a simplification and defined as the 0.5mm, the average thickness taken from several anthropometric sources [3-4, 42]. This particular modeling method would also allow future studies to investigate the effects of cortical bone thickness on scoliosis growth patterns.

As discussed in Chapter 2, cancellous bone is a porous bone best described as a series of vertical columns reinforced by horizontal links. However, creating the FE model in such a manner would require large amount of processing power that is currently not available. In addition, this type of geometry is difficult to model, as developing the cancellous bone structure from CT scans will result in

patient specific models that cannot be applied to the general population. Available CT scans also did not provide adequate cancellous bone imaging. Micro-CT scans would be capable of providing the appropriate cancellous bone imaging; however current technology is incapable of accommodating most sizes of human vertebra. While Ladd et al. [49] has successfully modeled the porous structure of the cancellous bone, in this study the bone will be modeled as a continuous solid entity and assigned a 'bulk' elastic property to reduce model complexity.

While ideally an annular epiphysis, a bony ring located on the perimeter of the inferior and superior of the vertebral bodies would be present in any FEA, it was determined through trial and error that such geometry would not be capable of thermal growth due complications arising from geometry meshing. As such, in order to eliminate such errors the annular epiphysis is neglected such that the superior and inferior surfaces of the vertebral body are flat.

As CT images provide little information regarding soft tissue, particularly the thickness and shape of the cartilage endplates and intervertebral disk, these components are manually created. For modeling simplicity, the cartilage endplates are modeled as a flat surface that extends towards the center over the vertebral body. The thickness of the plate will vary depending on its location on the vertebral body although a thickness of 0.5mm is specified in accordance with literature [50]. While physiologically these endplates do vary in thickness depending on its location on the vertebral body, this method will allow for an easy application of model loads, boundary conditions and the creation of an intervertebral disk. The shape of the cartilage endplates will depend directly upon

the shape of the vertebral body surface to which it is attached. The intervertebral disk will be placed between the two adjacent vertebra and possess a maximum average height of eleven millimeters as specified in literature [51].

As with bone, the intervertebral disk possesses variable geometric characteristics, including a different number of lamellae layers in the annulus region. To ensure that there is a good balance between processing time and accuracy, the number of annulus layers will be identical to the model developed by Denozière and Sharma et al. [52] Consequently, eight layers would be developed with the fiber material properties identical in the outer most two layers. The next two layers will possess slightly weaker fiber stiffness while the innermost two annulus layers will possess the weakest fiber stiffness. The volume ratio of annulus fibers to annulus ground substance has varied in different studies. Schmidt chose to vary the concentration from 5% in the inner most layers to 23% in the outermost layers [8-9]. An intervertebral disk model developed by Wong et al. [53] however, utilized a constant volume ratio of 16% throughout the annulus layers. For this study a constant volume ratio of fibers to ground substance of 20% was used, identical to values utilized by Denozière and Shirazi-Adl et al. [54]. This would result in an intervertebral disk that will maintain physiological accuracy while ensuring that model complexity and the resulting computational time would remain reasonable. The nucleus pulposus is assumed to be healthy and non-degenerative.

These assumptions will allow the FSU to be geometrically accurate while still maintaining a sense of generality to allow for the model to be applied to the

general population. The presence of endplates and unique fiber layers with varying properties in the intervertebral disk should provide a more accurate representation of the human FSU.

These simplifications, serve to improve upon current scoliosis models such as Stokes [30] and Villemure [32] where the vertebral bodies are oversimplified as cylinders or octagonal wireframes. However they are also designed to maintain generality so that the results can be applied to the general population and are not unique to a single individual.

5.1.2 Material Property Assumptions

As discussed previously, both cortical and cancellous bones are best described as an anisotropic material with slight viscoelastic effects. However, as anisotropic properties are not only difficult to model but could potentially increase model complexity and thus computational time, bone properties were assumed linear elastic transverse isotropic.

The exact mechanics of the cartilage endplates have not yet been analyzed in detail and as such the endplates are assumed to be isotropic as done by others (Yao et al. [41], Chiang et al. [2], Sairyo et al. [3] and Schmidt et al. [8]).

As the annulus region of the intervertebral disk shares many characteristics with composite materials, the annulus is approximated by a composite element type with tension only fibers embedded in a linear elastic ground substance. The nucleus region of the disk will be assumed to be nearly incompressible. Since static analysis will be focused upon in this study, the intervertebral disks changing properties depending on viscoelastic and creep effects are not considered.

Table 5-1 provides a range of the material properties utilized by other researchers while Table 5-2 details the material properties utilized in this study.

Table 5-1: Range of Material Properties use in Spine FEA Studies

	Young's Modulus (MPa)		
	E_{xx}	E_{yy}	E_{zz}
Cortical Bone	200 [4] – 17,000 [37]	200 [4] – 17,000 [37]	200 [4] – 17,000 [37]
Cancellous Bone	100 [33] – 330 [37]	100 [33] – 330 [37]	100 [33] – 330 [37]
	Isotropic Young's Modulus (E)		
Annulus Fibers	550 [9] – 450 [33]		
Ground Substance	1 [32] – 7 [8]		
Nucleus Pulposus	1 [32] – 4 [12] Incompressible [31]		
Endplates	10 [37] – 50 [9]		
	Shear Modulus (MPa)		
	G_{xy}	G_{xz}	G_{yz}
Cortical Bone	241.4 [32] – 5,000 [8]	241.4 [32] – 5,400 [30]	241.4 [32] – 5,400 [30]
Cancellous Bone	41.7 [32] – 48.3 [5]	48.3 [5]	48.3 [5]
Annulus Fibers	-		
Ground Substance	-		
Nucleus Pulposus	-		
Endplates	-		
	Poisson's Ratio		
	ν_{xy}	ν_{xz}	ν_{yz}
Cortical Bone	0.2 [31] – 0.484 [5]	0.315 [32] – 0.203 [5]	0.315 [32] – 0.203 [5]
Cancellous Bone	0.45 [5] – 0.315 [5]	0.45 [5] – 0.315 [5]	0.45 [5] – 0.315 [5]
	Isotropic Poisson's Ratio (ν)		
Annulus Fibers	0.30 [9] – 0.45 [37]		
Ground Substance	0.3 [37] – 0.4999 [4]		
Nucleus Pulposus	0.4999 [4]		
Endplates	0.3 [34] – 0.4 [5]		

Table 5-2: Selected Material Properties

	Elastic Modulus (MPa)			Poisson's Ratio			Shear Modulus (MPa)		
	E_{xx}	E_{yy}	E_{zz}	v_{xy}	v_{xz}	v_{yz}	G_{xy}	G_{xz}	G_{yz}
Cortical Bone [8]	11,300	11,300	22,000	0.484	0.203	0.203	3800	5400	5400
Cancellous Bone [8]	140	140	200	0.45	0.315	0.315	48.3	48.3	48.3
Annulus Fibers [42]	550/485/420/360			0.30			-		
Ground Substance [42]	4.2			0.45			-		
Nucleus Pulposus [7]	4			0.4999			-		
Endplates [8]	23.8			0.40			-		

Recall that in order to better simulate the gradual decrease in stiffness of the annulus layers, the annulus fibers will decrease in stiffness the closer they are positioned to the nucleus. Thus the outer two annulus layers will be the stiffest (a Young's Modulus of 550MPa) and the closest two annulus layers will be the softest (360MPa).

The thermal expansion coefficient of bone, while not directly relevant to the mechanical loading of the spine, is used for the growth model. The thermal expansion coefficient of bone in the longitudinal direction was taken to be 27.5×10^{-6} mm/^{o}C, a value experimentally determined by Singh Ranu [55]; thermal expansion coefficients in other directions were set to zero as the focus of this study was asymmetric growth in the axial direction. Note that given how the thermal expansion equation is applied, the actual value of the thermal expansion coefficient is not critical to the analysis however; the experimentally determined value by Singh Ranu will be utilized for accuracy purposes.

5.1.3 Growth Model Assumptions

To replicate bone growth utilizing the vicious cycle theory, growth would be modeled using a slightly altered growth modulation equation developed by Stokes [30-31]. Equation 5-1 would receive information regarding stresses within individual elements due to symmetric and asymmetric loads and determine the amount of strain within the elements resulting from both biological growth as well as the mechanical loads.

$$\dot{\varepsilon} = \dot{\varepsilon}_m (1 - \beta(\sigma - \sigma_m)) \qquad \textbf{5-1}$$

Where, $\dot{\varepsilon}$ is defined as the total bone growth rate in millimeters per millimeter per year, $\dot{\varepsilon}_m$ is the baseline growth of a healthy spine, β is the growth sensitivity factor, σ is the compressive stresses along the superior-inferior axis in the vertebra under asymmetric loading and finally, σ_m are the stresses in the vertebral body under normal symmetric loading conditions. Compressive stresses are designated as positive while tensile stresses are negative.

To simulate an individual undergoing puberty, the strain rate of the vertebra will vary depending on the year. The values for the strain rate taken from literature are summarized in Table 5-3 [56]. Note that strain rates listed in Table 5-3 are for the baseline growth only. A growth sensitivity factor (β) of 1.5MPa^{-1} will be utilized in accordance with literature [30].

Table 5-3: Vertebra Baseline Growth Rates ($\dot{\varepsilon}$)

Age	Spinal Column Height (mm)	Spine Growth Velocity (mm/year)	Strain/year
8	205.9	16.5	0.080311
9	220.9	15.4	0.069927
10	235.1	14.2	0.060333

To model functional spinal unit growth under different loading conditions, thermal growth will be used as it can both expand and contract a volume much like bone growth and resorption [4]. The thermal growth equations used are defined as:

$$\varepsilon = \alpha \Delta T \qquad \textbf{5-2}$$

and

$$\varepsilon = \dot{\varepsilon} \Delta t \qquad \textbf{5-3}$$

where, ε is thermal strain, ΔT is the thermal load, Δt is the time period, $\dot{\varepsilon}$ is the strain rate determined from the growth equation above (Equation 5-1), and α is the thermal expansion coefficient as specified in the previous section. Since a one year basis was used, the magnitude of the strain (ε) and strain rate ($\dot{\varepsilon}$) are always the same. By applying different thermal loads to different regions of the spine it is possible to achieve different levels of growth in these regions. In summary the use of thermal growth equations are as follows:

(1) Determine the baseline strain rate given the 'age' of the FSU ($\dot{\varepsilon}_{m}$) from Table 5-3.

(2) Solve Equation 5-1 for the total strain at that specific year due to biological and loading conditions ($\dot{\varepsilon}$) using stress values achieved from FEA.

(3) Use of the calculated strain over one year from step two into Equations 5-2 and 5-3 to determine the thermal load required to achieve the desired strain growth in one year.

(4) Application of the calculated thermal load onto the FE model.

(5) Change and update in geometry due to thermal loads and repeating steps

1-5 for three years.

While bone growth would occur in all directions, as the chief interest of this study is longitudinal growth along the superior/inferior axis of the vertebra, thermal expansion coefficients in all other directions are set to zero.

The effects of the preceding vertebral body mass, i.e. the mass of the L3 vertebra on the L4 vertebra are assumed negligible compared to the applied loading.

5.2 Model Creation Methodology

Model development possessed two major phases: creation of an accurate geometric model and the implementation of the finite element growth model. Please refer to the previous section regarding stated assumptions.

5.2.1 Vertebra Surface Topography Creation

The geometry of the lumbar spine was based upon CT images (Ethics Project Number R-2777) taken of a healthy individual from the Glenrose Rehabilitation Hospital, Edmonton provided in Dicom file format. The base geometry of the vertebra was created with the 3D imaging conversion software Simpleware™ (Simpleware Ltd. Exeter, UK). Although the most prevalent instances of scoliosis occur in the thoracic region of the spine, the provided CT images mapped only the lower thoracic spine and the entire lumbar region. Due to image clarity the L3 and L4 vertebra were selected out of the lumbar region of CT Images. Note that this procedure only creates surface topography.

To reduce memory demands, CT slices were first cropped to the appropriate size. The original scans included the entire lumbar region as well as some thoracic vertebra. All slices that did not contain any portion of the L3/L4 vertebra were removed. Slices were cropped such that only the vertebral body and the posterior elements remained as shown in Figure 5-1. Cropping did not increase or decrease the resolution of the images, it only served to reduce the processing time needed to create a three-dimensional model from the 2D slices.
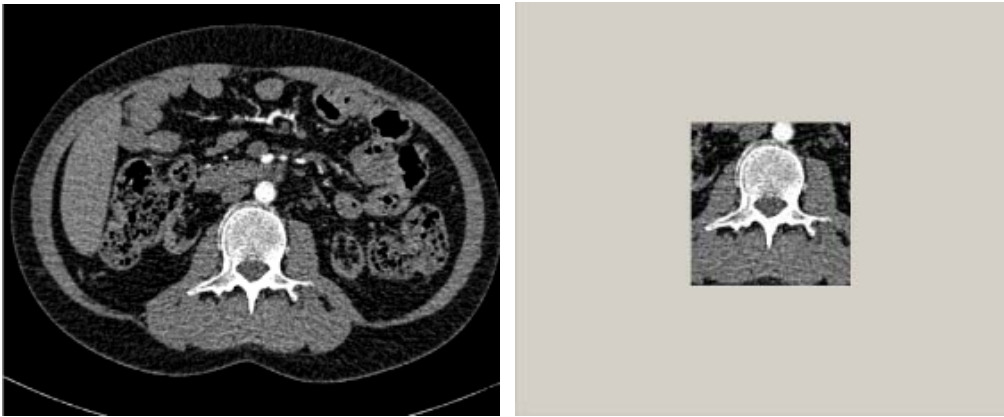
Figure 5-1: A sample CT scan of the L3 vertebra. The image on the left is the original CT slice while the image on the left is the cropped image

Simpleware converts two dimensional CT scans into three dimensional models by manually highlighting regions of interests on each of the scans. These highlights, called 'masks', are created much in the same way as a conventional paint program.

Several different methods were used to create the cortical/cancellous bone masks in Simpleware. The most automated method required the use of a Simpleware built algorithm called 'Confidence Connected Region Growing' (CCRG). By manually selecting an initial pixel (known as the seed point), the software then automatically samples the grayscale values of the pixels immediately adjacent to the seed point. The mean and standard deviation of the

sample is then calculated. Pixels that are connected to the seed point and fall within a user specified boundary (by default ±1 standard deviation) are automatically selected.

This particular method was successful in not only outlining the boundaries between the cortical and cancellous bone but determining the outer perimeter of the vertebra. Both of these objectives were completed with very little user input, thus reducing any individual biases manual mask creation would incur. Figure 5-2 displays the results of this CCRG algorithm. While visually accurate, this method made it difficult to import into modeling software such as Pro-Engineer™. In particular, complications arise due to volume overlap, gaps within certain regions of the cortical/cancellous interface and difficulties in creating a volume out of the cortical bone shell. As such, this particular method of geometry creation was not used in this study and will require future investigation in order to be properly implemented.
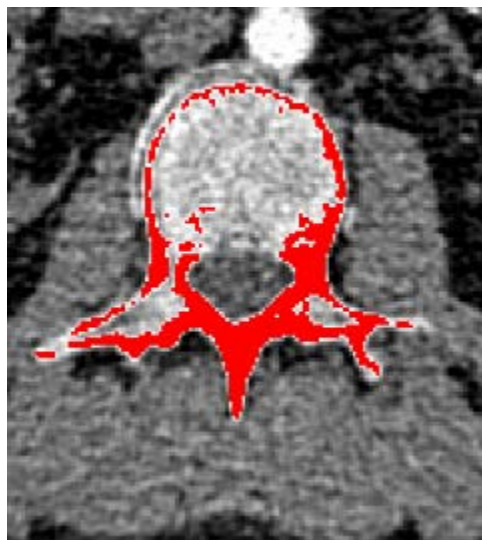
Figure 5-2: An example of the Simpleware CCRG algorithm. The method automatically highlighted the predicted cortical bone region in red

As a constant thickness cortical bone wall was determined to be an important aspect in this particular study, it was decided that Simpleware would be used primarily to establish the surface topography of the vertebral bodies themselves as opposed to determining the cortical/cancellous bone interface. Instead, the cortical and cancellous bone interface would be modeled in a separate program as it would ensure a constant thickness boundary. As such, vertebral bodies in Simpleware were modeled as single continuous entities as shown in Figure 5-3. In accordance with the assumptions listed in the previous section, only half of the vertebra was modeled and then mirrored to ensure symmetry within the vertebra. As no 'mirror' function was built into the Simpleware software, the other half of the vertebra was manually masked so that it was identical to the original. Differences in rendering however did cause slight differences in the form of bumps and divots between the two vertebra halves. These differences however were deemed negligible as they could be corrected and removed during volume creation. The boundary between the vertebral body and the surrounding tissue was determined visually, as was boundary between the posterior elements (in particular the pedicles) and the vertebral body. Consequently there are certain regions of the mask that do not appear to coincide with the actual vertebral body shape.
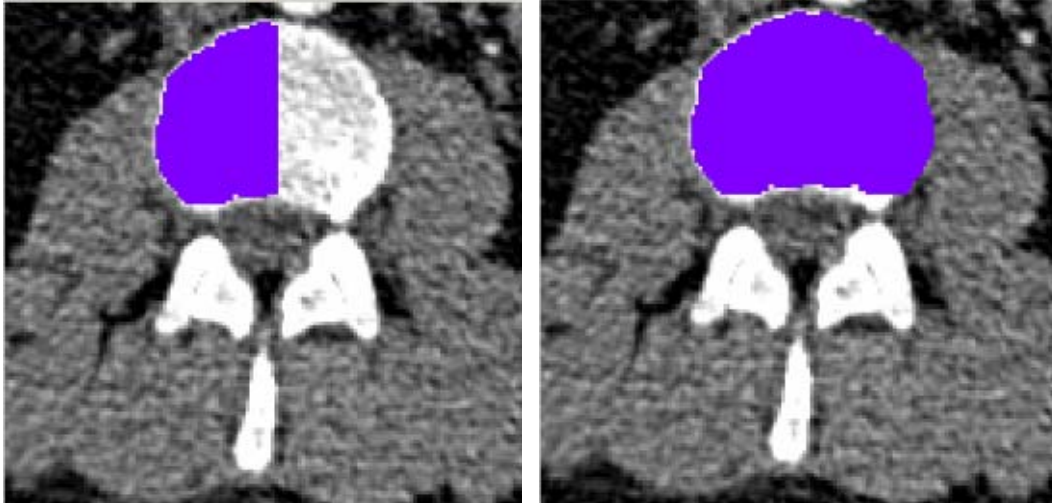
Figure 5-3: The final model created in Simpleware. The left image shows the half model created while the right image shows the mirrored result

The final Simpleware model is shown in Figure 5-4. Note that both the L3 and L4 vertebra were created and imported independently (i.e. not as an assembly consisting of both vertebra in one model) into a separate modeling software called Pro-Engineer™ (PTC, Massachusetts, USA). In addition, as can be seen in Figure 5-4, several unique surface features (bumps and holes for example) are present due to patient specific features or modeling rendering is removed at the next stage.
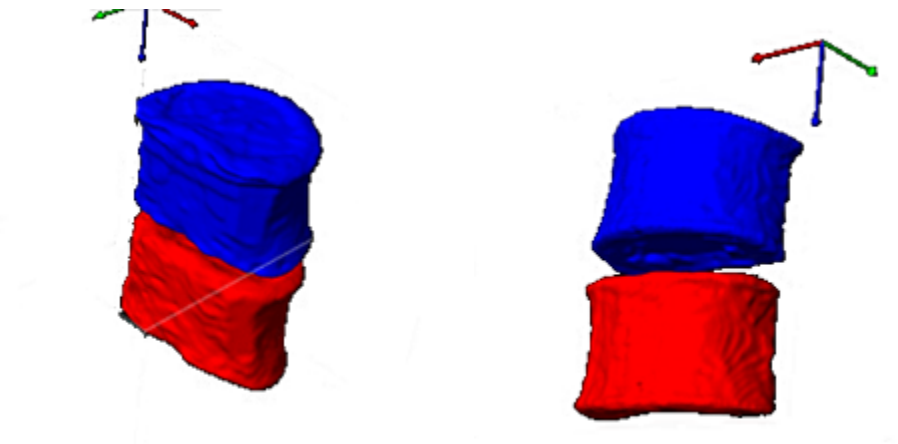
Figure 5-4: The L3/L4 vertebra model created in Simpleware. The L3 vertebra is shown in blue while the L4 vertebra is shown in red

The coordinate system introduced can be seen in Figure 5-4. The axial direction (straight up and down through the two vertebral bodies) is defined as the z-axis (blue arrow) with the positive direction extending downwards. The x axis is the medial-lateral axis (red arrow) with the positive direction pointing to the right when viewed from the front while the y axis is the anterior-posterior plane (green arrow) with the positive direction directed towards the back of the vertebra. The model is then saved as a stereo lithography (STL) file which transforms the surface topography into a series of triangular facets. The STL file does not provide surface structure data aside from geometry, meaning that it does not create a volume and is not composed of surfaces.

5.2.2 Surface Smoothing and Creation

Once the geometry was established in Simpleware it was imported into a 3D modeling software, Pro-Engineer in which the faceted file can be fitted with surfaces in which volumes can be created. All of the smoothing and surface creation features are done using Pro-Engineering 'Reverse Engineering' add-on software. Prior to any surface creation, the STL files are first smoothed to eliminate patient specific surface features to generalize the model and reduce the number of potential stress concentration point, as can be seen in Figure 5-5.
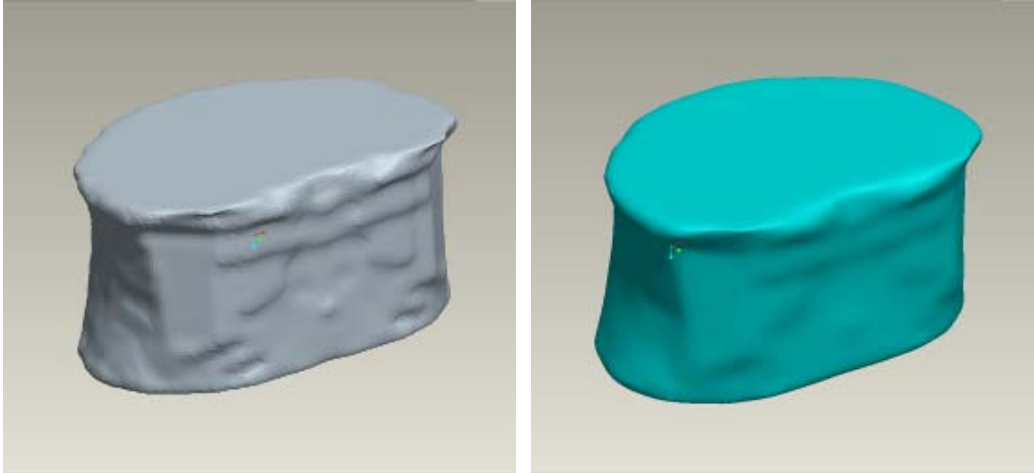
Figure 5-5: The original stl file of the L3 vertebra imported from Simpleware (left) and the smoothed version created in Pro-Engineer (right)

Smoothing the original STL file required the use of several different functions, all used in combination with one another. The first step is to eliminate any abnormal folds that the STL file may contain (Figure 5-6), achieved by simply manually deleting the offending facets and filling in the gap by manually creating replacement facets. Following this step would be the application of several different functions which would serve to smooth the surface of the vertebra as well as increasing the facet count to better model the natural curves in the vertebral body.

(a)   (b)
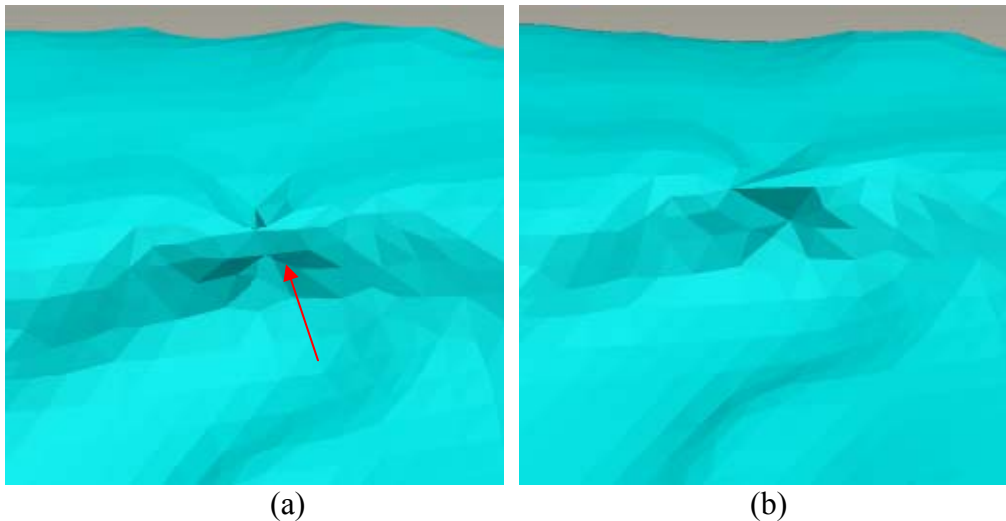
Figure 5-6: The first step of the smoothing process. Image (a) shows an overlap of facet features (pointed in red). Image (b) shows the resulting correction where the overlap is removed and manually created facets replace it

The following functions were applied in no particular order but they may have been applied multiple times in order to achieve the desired model appearance.

- Clean: used to reduce the facet count on the model by smoothing geometry with respect to the curvature of the model. Provides minor reduction in patient specific surface features.

- Refine: replaces each of the facets with four smaller ones. Prepares model for further smoothing options.

- Relax: primary means to smooth the model. It uses an iterative method to smooth the facet model and the strength of the smoothing procedure can be adjusted to suit the users need. The greater the strength of the smoothing procedure the greater the loss of patient specific data.

- Decimate: reduces the number facets on the model and is usually the last function to be employed in the smoothing process.

Once smoothing of the vertebra is complete, the facet model is then fitted with infinitely thin surfaces. The reverse engineering software allows for the creation of surfaces manually or through its automated process. Due to the complexity of the vertebra, the automated process was used as it ensured that the resultant surfaces were molded as closely to the facet model as possible.

The automated process requires two inputs from the user, namely, the approximate number of surfaces the model is to be covered with and the resolution (how closely the surfaces match up with the underlying facets). For the vertebral bodies, it was determined through trial and error that about four hundred and fifty to five hundred triangular or quadrilateral surfaces would be needed to accurately fit to the underlying facet model. Figure 5-7 displays the created surfaces placed over the green facet model. Note that the green patches indicate regions where the facet model is above the created surfaces (shown in grey) and vise versa. The continuous change in color indicates that the created surfaces closely mimic that of the underlying facet model. At the conclusion of the surface creation, the L3 vertebra contained 476 surfaces while the L4 vertebra contained 495 surfaces. The differences in number can be attributed to the differences in shapes between the two vertebral bodies.
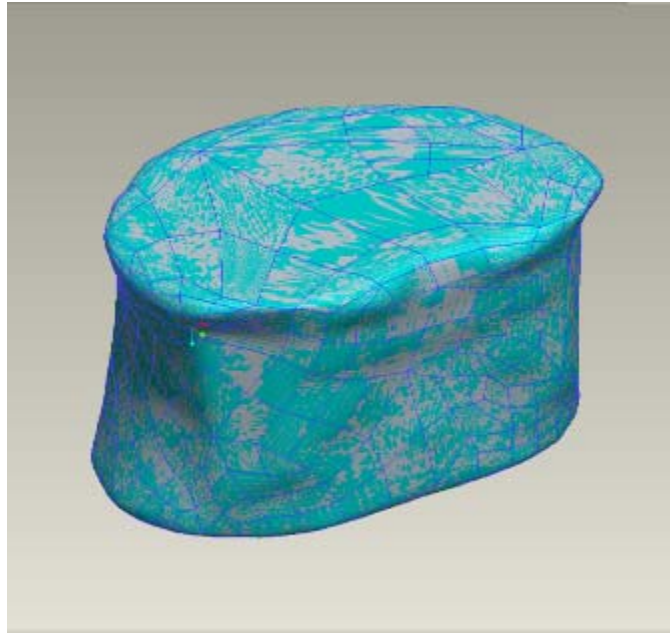
Figure 5-7: Surface creation over the base STL model. The surfaces are shown in grey and are outlined by blue lines. The STL base is shown in green

As with the original facet model however, the automatically created surfaces do at times suffer from unexpected geometric characteristics. Despite being infinitely thin, a small number of surfaces (usually numbering no greater than twenty per body) suffer from inexplicable 'folds' or 'ripples'. These particular surfaces are deleted from the model and replacement ones are manually created. These manually created surfaces also have to undergo additional algorithms to ensure that they not only adhere closely to the underlying facet model, but also maintain a consistent boundary condition with the adjacent surfaces. Figure 5-8 below displays an example of a 'rippled' surface along with the manually created and corrected surface.
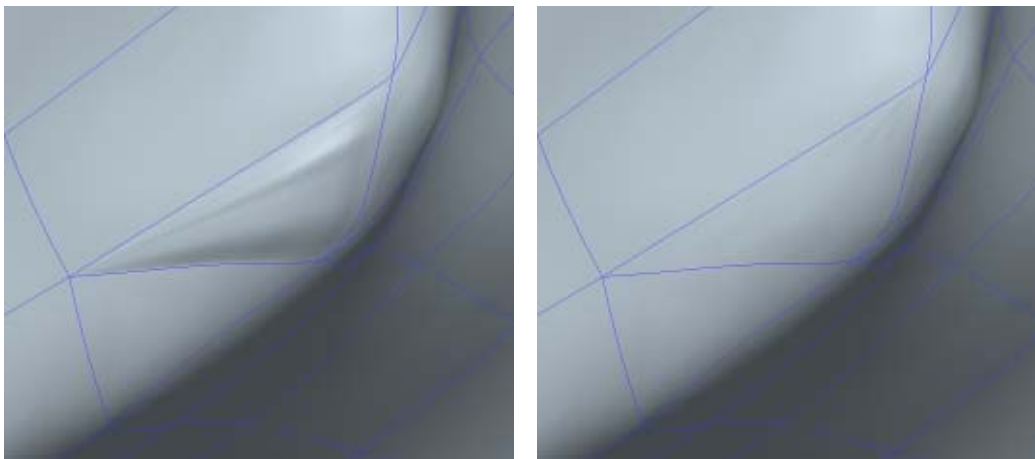
Figure 5-8: An example of surface correction in Pro-Engineering. The left image shows a rippled or bulging surface while the right image displays the corrected flattened surface

At this point it is vital to ensure that there are no gaps or holes in the model (which are usually a result of inaccurate surface creation). Gaps in the surface model will result in the inability to create the cortical/cancellous bone as discussed below.

5.2.3 Cortical and Cancellous Bone Creation

Once surfaces are mapped, it is possible to turn them into volumes. Volume creation using the surfaces as a basis can be created in two different ways: thickening, which thickens the surfaces to a user specified amount or solidification, which fills in a void completely enclosed by a group of surfaces with a single continuous solid entity. In order to create the cortical and cancellous bone, these volume creation methods were employed separately.

To ensure a constant thickness shell, both the cortical and cancellous bone was 'solidified' as shown in Figure 5-9. Once complete, the size of the cancellous bone was scaled down so that once placed in the center of the cortical bone, a constant thickness 0.5mm space between the cortical and cancellous bone remained. Figure 5-10 displays the cancellous bone placed within the cortical

71

volume with the green/gray regions indicating overlapped regions of the two volumes. Note that the surface lines seen in Figure 5-7 and Figure 5-8 have been removed for clarity purposes only.
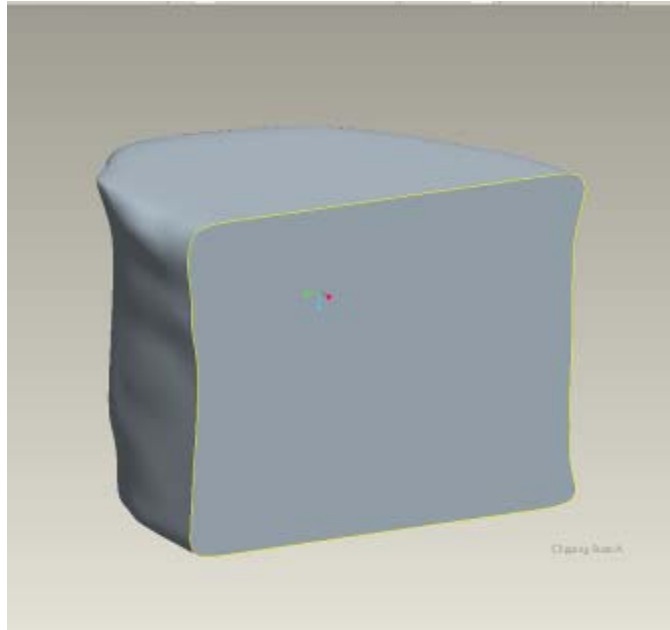
Figure 5-9: A sectioned view of the L3 vertebra cortical bone model
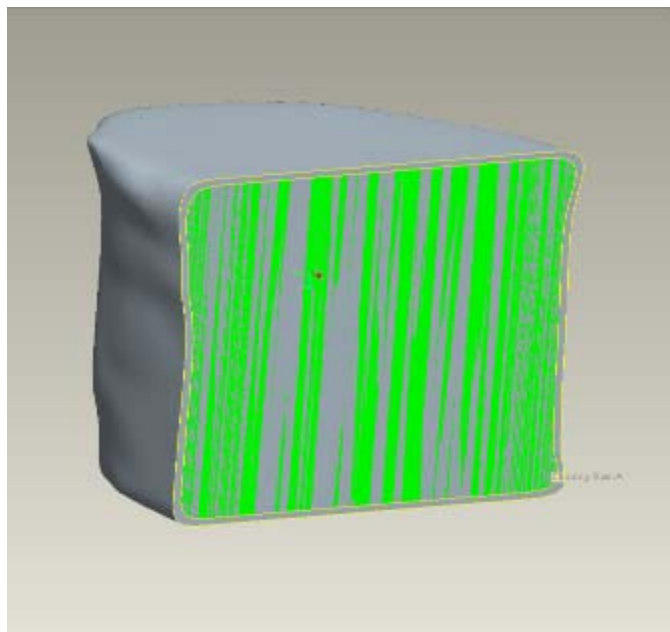
Figure 5-10: A sectioned view of the L3 vertebra cortical bone model with the cancellous bone placed within the cortical bone (the green/gray coloring)

An alternative model creation method would be the use of a shell command to create a constant thickness cortical shell and 'filling' the interior volume with cancellous bone. This method was not utilized in this particular model due to software errors.

In preparation for the creation of the vertebral endplates, two additional datum planes were created. These planes were placed on the most distal points of the superior and inferior surfaces of the vertebral body. From these planes the vertebral endplates would extend towards the vertebral body to create an endplate. Figure 5-11 displays the superior and inferior endplate planes on the vertebral body.
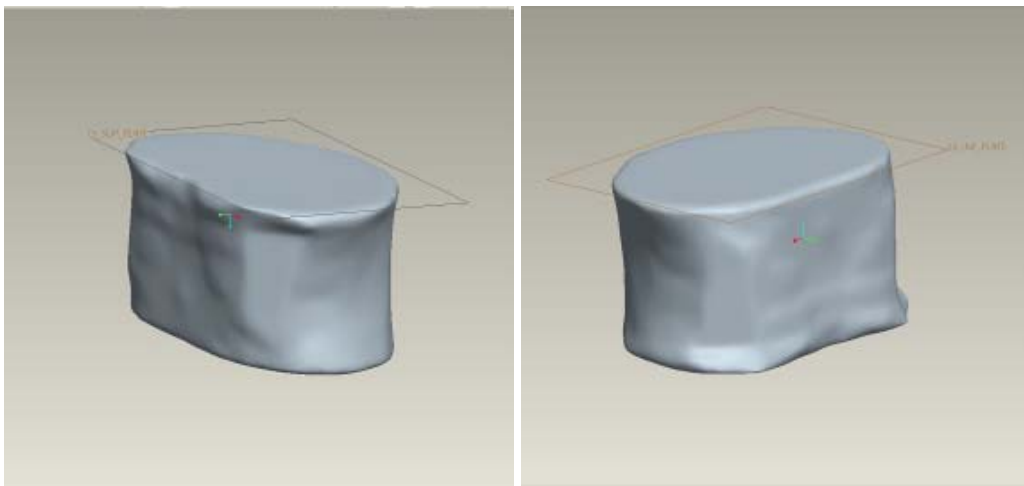
Figure 5-11: The superior (left) and inferior (right) endplate planes on the L3 vertebra

Once all planes are defined and a check to ensure that a constant thickness of 0.5mm exists between the outer cortical surface and the inner cancellous areas is complete, the overlapping cortical material is subtracted. This final geometric model, as shown in Figure 5-12 resulted in a constant thickness cortical shell with a perfect interface between the cortical and cancellous bone. This process was repeated for the second vertebra.
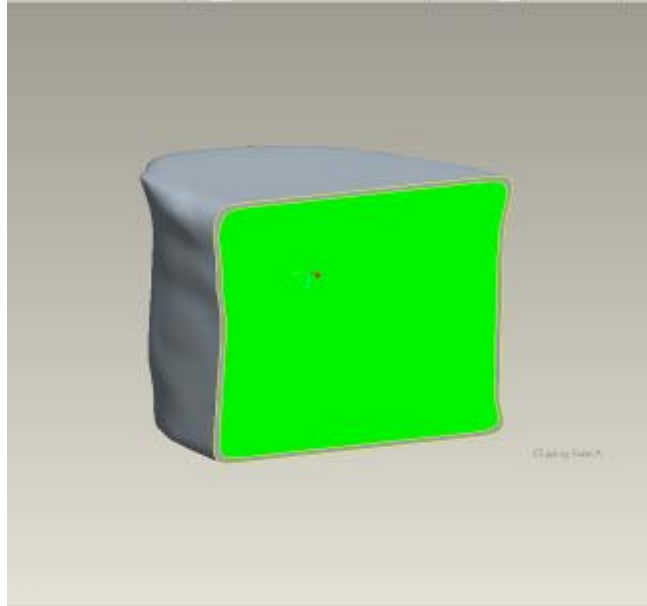
Figure 5-12: The cancellous bone (shown in green) within the outer (gray) cortical shell

5.2.4 Endplate Geometry

As soft tissue is not readily visible in CT images, the cartilage endplates as well as the intervertebral disk are created manually. The endplate shape always follows the shape of the vertebral body it is attached to; thus, a rough outline of the superior/inferior surfaces of the vertebra is defined using the planes created in the previous section as that of the perimeter of the endplate (Figure 5-13).
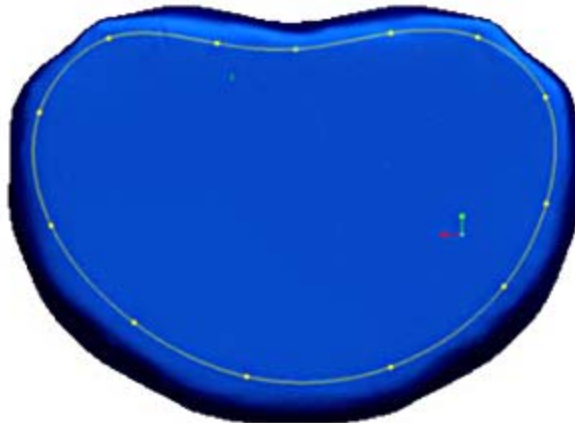
Figure 5-13: The outer perimeter of the L3 superior endplate (sketched in yellow)

Using the sketch at a basis, the enclosed area is then turned into an infinitely thin surface thickened in the same manner as described in the previous section to the average minimum endplate thickness 0.5mm [41-42, 57]. In order to ensure that this thickness is maintained, the endplates are extended away from the center of the vertebral body by 0.5mm as well as extended towards the center of the vertebral body such that there was significant overlap between the newly created endplate and the cortical/cancellous bone underneath. Figure 5-14 below displays the endplate creation process.
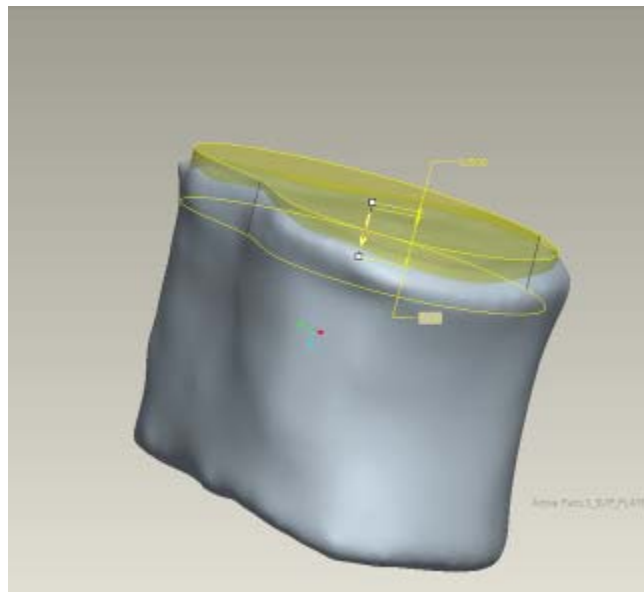
Figure 5-14: The creation of the endplate volume. Notice that a thickness of 0.5mm was extended distally from the vertebral body surface. The yellow region indicates the original endplate volume

As done with the cortical/cancellous interface, the overlapping endplate material was subtracted from both bone types such that a perfect mesh between the endplate and the cortical bone could be achieved. An example of the final endplate model is presented in Figure 5-15 while the final vertebra model, complete with endplates, is shown in Figure 5-16.
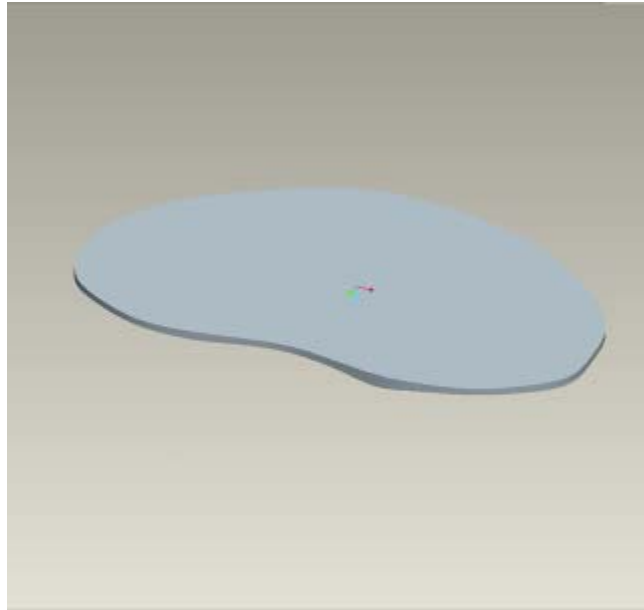
Figure 5-15: The L3 superior endplate once the overlapping volumes have been removed, notice the irregular edge at the bottom of the plate. This irregular edge is due to the curves on the vertebral body itself
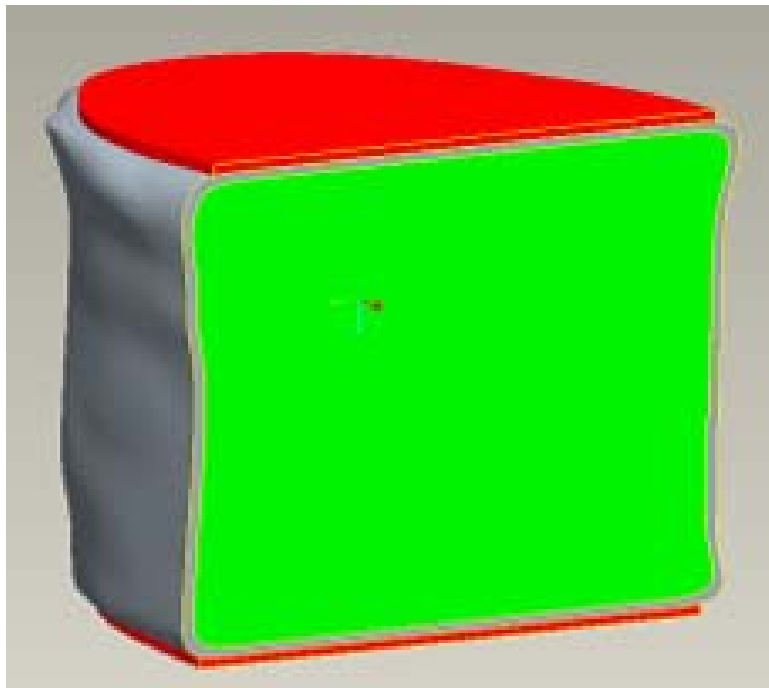
Figure 5-16: The complete L3 vertebra with both superior and inferior endplates (red), cortical bone (grey) and cancellous bone (green)

As the endplates models imported directly from Pro-Engineer result in meshing errors in Ansys, it was necessary to make some minor adjustments to the volume. As with the creation of vertebral body surfaces outlined in section 5.2.2,

the process of correcting the cartilage endplates was an interactive procedure. The first step involves meshing a single endplate to determine where the 'troubled' areas are located as shown in Figure 5-17. Once the areas that cause mesh failures are isolated, the volume is unmeshed and the offending area deleted and replaced (Figure 5-18). The endplate is once again remeshed to isolate any other additional troubled areas. This process is repeated until the endplate meshing procedure yields no element errors or warnings. Care was taken to ensure that the finite element model still matched the vertebral body surface
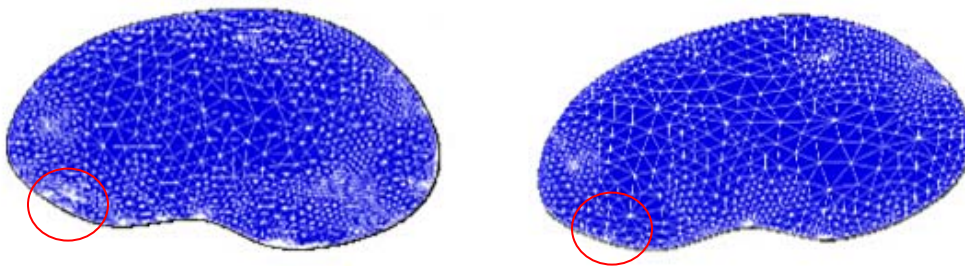
Figure 5-17: The superior L3 with the default mesh (left) and the corrected, error free mesh (right). Notice the unnecessarily high mesh density due to abnormal area shapes, manual area corrections reduced the mesh density in these areas and consequently removed the number of elements with aspect ratio or other such warnings
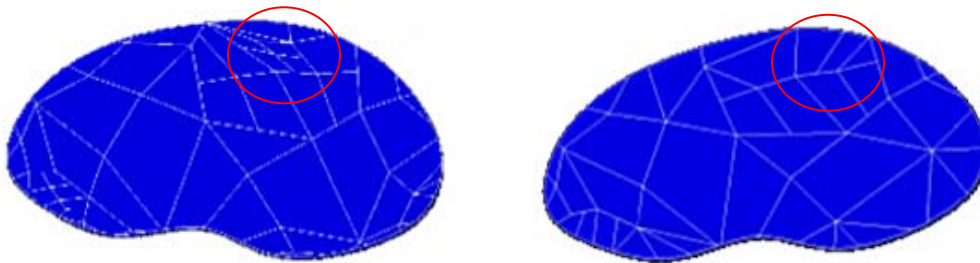
Figure 5-18: The left image shows the original endplate area formation while the right image displays the corrected image which results in the corrected mesh structure. Notice the difference in the area shapes

Both L3 and L4 vertebras were created in exactly the same manner.

5.2.5 Functional Spinal Unit Creation

The vertebras are assembled together as a single unit. The anterior end of the vertebral bodies were separated by eleven millimeters, and due to the natural incline of the vertebral bodies with respect to one another, the posterior end of the vertebral bodies were separated by ten millimeters. The vertebra separation distance was acquired through the available CT data. The assembled model without the intervertebral disk can be seen in Figure 5-19.
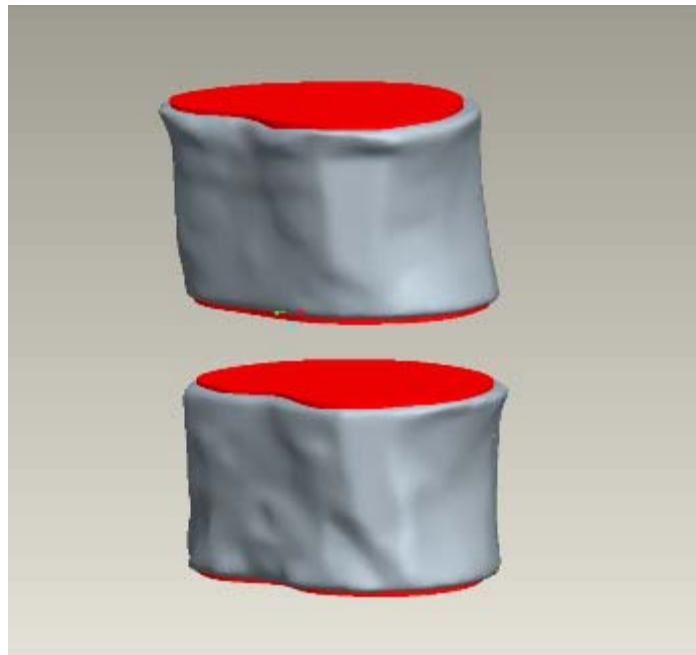
Figure 5-19: The L3 and L4 vertebra assembled together prior to the placement of the intervertebral disk

Once the vertebras were assembled, they were then exported as an Initial Graphics Exchange Specification or IGES file into the finite element modeling program ANSYS™ (Ansys Inc. Pennsylvania, USA). As opposed to an STL file which contains only surface topography data a no physical geometry, an IGES file contains information regarding the volumetric geometry and surfaces for easy manipulation of solids.

5.2.6 Intervertebral Disk Geometry

To ensure ease of material property assignment, particularly in regards to the annulus fibers, the intervertebral disk was created entirely in Ansys.

The first step was the creation of the outer surfaces of the disk. By using the perimeter of the inferior L3 endplate and the superior L4 endplate, it was possible to create surfaces to represent the outer surface of the intervertebral disk as seen in Figure 5-20 (a). By 'capping' the open ends of the surface, it is then possible to create a volume. Figure 5-20 (b) displays the total disk volume, complete with variable cross section.

(a)   (b)
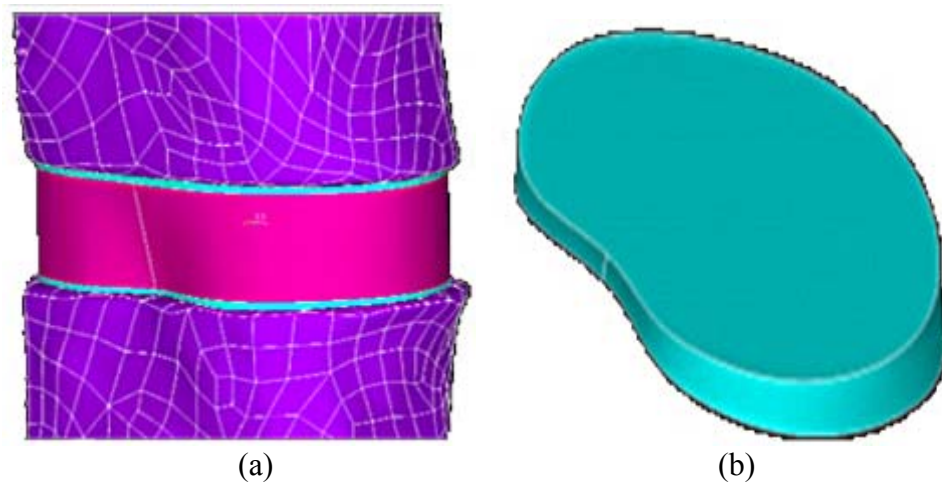
Figure 5-20: Image (a) The outer surface of the intervertebral disk shown in pink and Image (b) the total intervertebral disk volume

Once the gross volume has been established, the annulus layers are then created. Using the disk volume as a reference, a new volume is created and scaled back such that it would create approximately 1.1mm thick layer when placed co-axially with the base volume as seen in Figure 5-21. This processes of copying and scaling is then repeated with the new volume until eight additional volumes are created as shown in Figure 5-22. Alterations in the scaling factor ensured that

each subsequent layer was thinner than the previous one, reflecting the characteristics seen in physiological disks. Once the volumes are appropriately placed, the overlapping material is deleted leaving the final intervertebral disk geometry seen in Figure 5-23. The nucleus was modeled such that it occupied approximately 50% of the total disk volume, a value in agreement with literature [10].
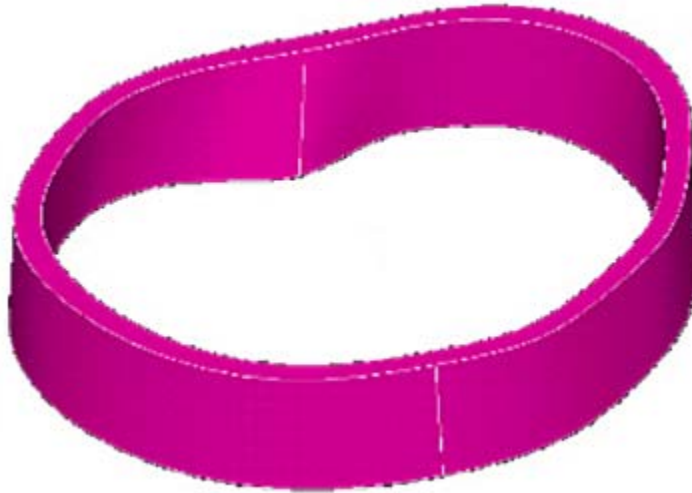
Figure 5-21: A single annulus layer created in Ansys
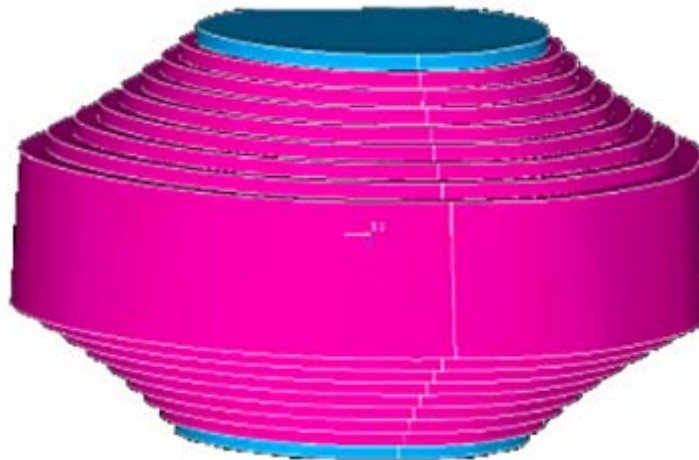
Figure 5-22: Eight annulus layers as well as the nucleus created in Ansys, the gross but temporary exaggeration of each layer height is required for easy manipulation
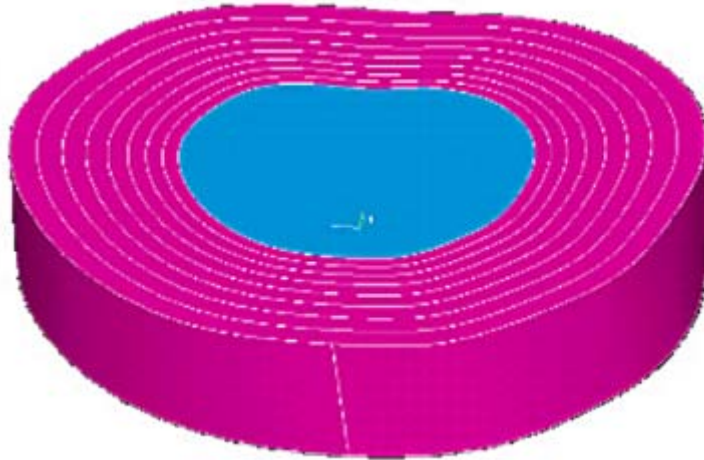
Figure 5-23: Final intervertebral disk model used in the FSU

5.3 Finite Element Model Creation Methodology

For the model utilized in this study, the quadratic tetrahedral element seen in Figure 3-2(b) will be utilized to model the cortical bone, cancellous bone, nucleus pulposus and cartilage endplates. The annulus region of the intervertebral disk will be modeled using composite elements. To reduce the number of elements found within the center of the cancellous bone, element expansion will be utilized effectively increasing the size of the elements as they progress towards the center of the cancellous body.

5.3.1 Material Property and Element Assignment

The material properties for the cortical bone, cancellous bone, cartilage endplates and the nucleus pulposus were applied to the model with values outlined in section 5.1.2. All of the models utilized Ansys Solid92 elements which are 10-node tetrahedral elements capable of modeling irregular meshes seen by the vertebra and the endplates. While the element count could have been reduced by utilizing brick shaped elements in the interior of the cancellous bone, this caused an increase in element shape errors. Consequently, measures were taken to

reduce element numbers by gradually increasing the element size towards the center of the cancellous bone.

In order to properly reproduce the fiber orientation of the annulus, the region was modeled using a reinforced concrete element (Solid 65). This particular element type allows for fibers to be orientated at user defined angles within an isotropic medium. In order to ensure that the fibers are orientated thirty degrees from the horizontal axis of the spine, a local cylindrical coordinate system was first defined at the center of the intervertebral disk. The x-y axis lying on the transverse plane while the z-axis maintained the same convention as the global coordinate system and was placed along the axial axis with the positive direction running superior to inferior.

In Ansys, the rebar (or annulus fibres in this particular case) within the solid element are defined by the convention system seen in Figure 5-24. Notice that the angle φ represents the angle from the y-axis on the y-z plane while the angle θ represents the angle from the x axis on the x-y plane.
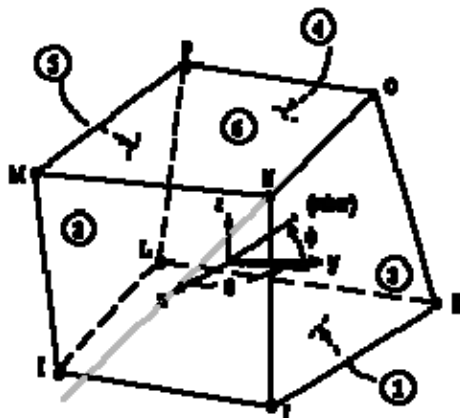
Figure 5-24: The angle definition of the reinforced concrete solid in Ansys. Adapted from the Ansys help files

Using the local coordinate system as a basis, the fibers are orientated such that the angle θ is 60° and the angle φ is 30°. This angle system was used for all

odd numbered layers (layers 1, 3, 5 and 7) while the angles of 120° and 150° for θ

and φ respectively were used for all even numbered layers with the layer count

beginning at the exterior working in. This angle orientation is necessary to ensure

that the fibres are appropriately angled throughout the entire annulus layer. In

agreement with previous studies and as mentioned in section 5.1.1, the ratio of

fibers to ground substance was specified as 0.2 or 20%. Figure 5-25 displays the

fibre element orientation in the outermost fibre layer while Figure 5-26 displays

the fibre element orientation in the innermost fiber layer.
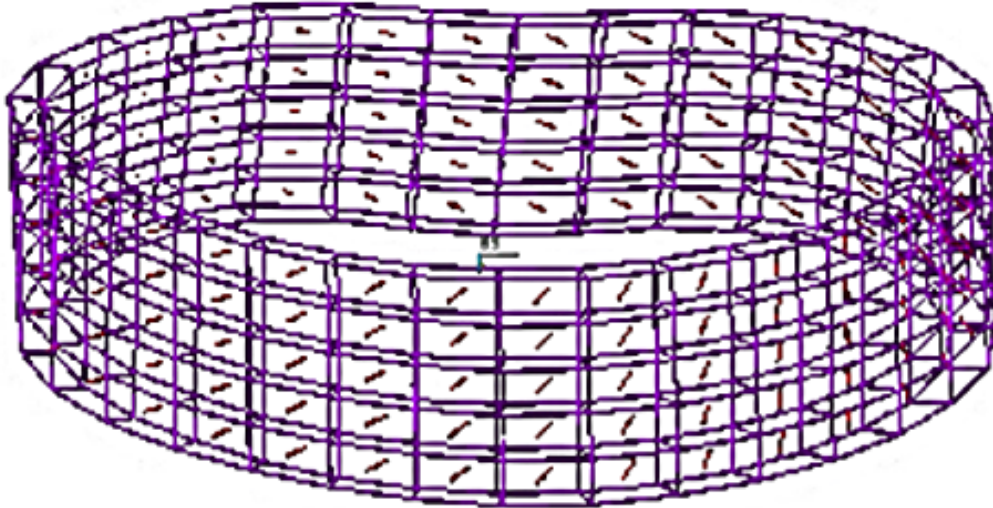
Figure 5-25: The outermost fiber layer of the annulus region. The lines within the layers indicate the direction of the fibers as well as the concentration. Notice how the fibers are angled with respect to the local coordinate system seen in the center of the screen
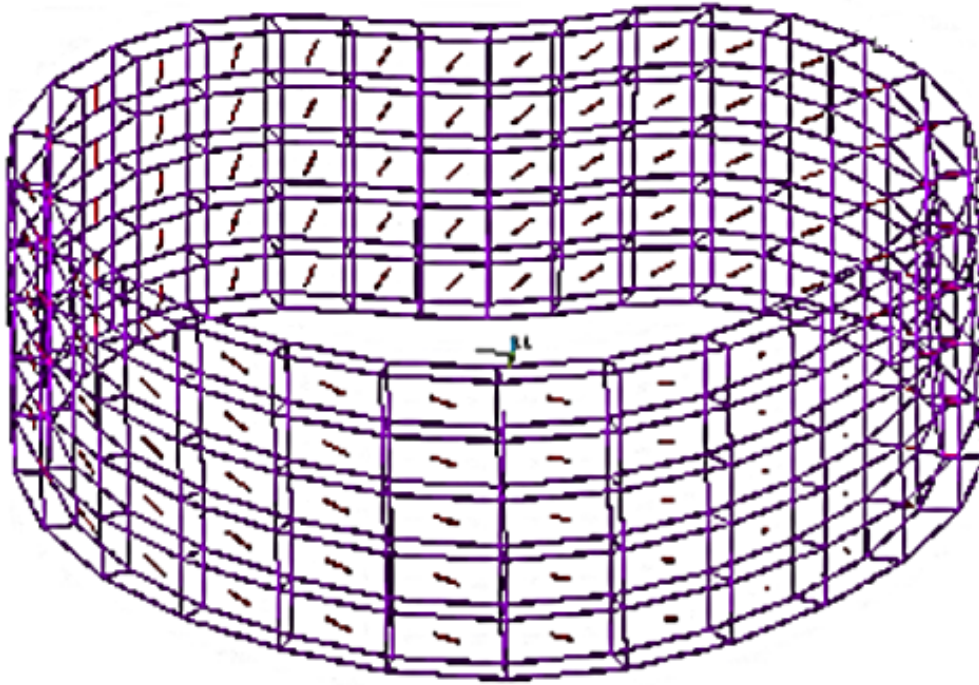
Figure 5-26: The innermost fiber layer of the annulus region. Notice how the fibers are orientated at the different angle than the ones seen in Figure 5-25

Note that the fibers on the far left and right side of the layers appear to be orientated vertically. This is merely due to the viewing angle of the layers and if viewed from the side it can be seen that the fibers are still angled 30° from the horizontal axis. Figure 5-27 displays the functional spinal unit geometry. Different colored regions indicate volumes with different material properties.

Figure 5-27: The L3/L4 functional spinal unit geometry in Ansys. The intervertebral disk is shown in purple

5.3.2 Volume Meshing

Due to the complexity of the model geometry, in order to maintain geometric accuracy, the creation of a custom made mesh would be unreasonable and inefficient. Consequently, the meshing done on the finite element model was generated automatically by Ansys. This automatic meshing included all the endplates, the cortical bone and the intervertebral disk. While defaults were used in a majority of the meshing, the mesh density within the cancellous bone was altered slightly such that fewer elements were located within the core. As the majority of bone growth occurs on the outer surface of the bone it was critical to acquire accurate and sufficient data for the cortical bone and the outer surface of the cancellous bone. In contrast, the interior of the cancellous bone will not be highly sensitive to biomechanical loading meaning that a lower mesh density

would be sufficient. This mesh transition from high density to low also aided in the reduction of element count and thus decreasing computational time.

To ensure that geometric accuracy was preserved and to reduce the number of element aspect ratio errors, a high number of elements (524,916) were utilized. Figure 5-28 displays the meshed FSU.
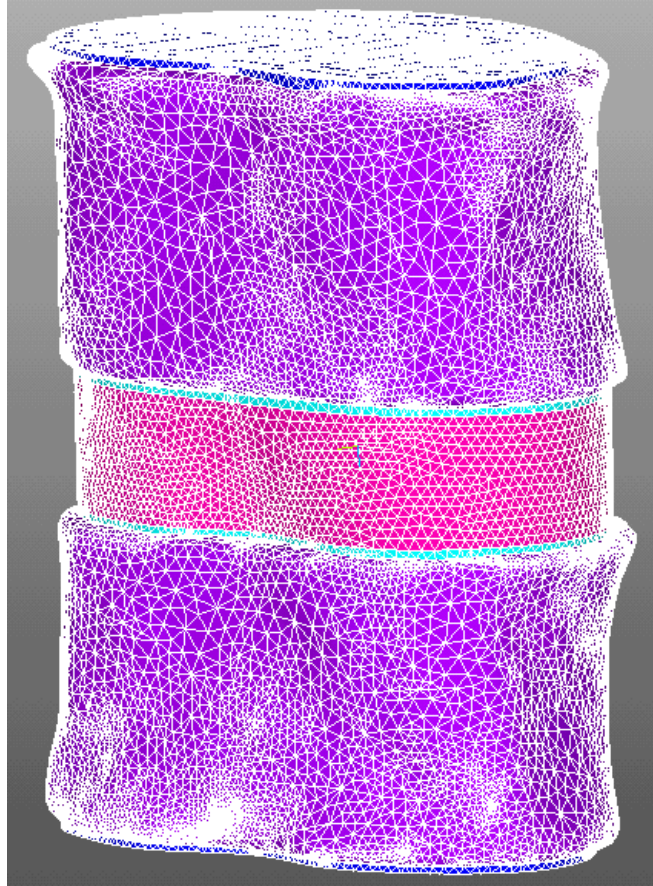
Figure 5-28: The L3/L4 functional spinal unit once meshing was applied

5.3.3 Contact Elements

As Ansys does not import any part interaction from Pro-Engineer, the FSU model requires information as to where contact between the cortical/cancellous and the cortical/endplate boundaries occurs. This step was particularly important for the finite element model as it was necessary to ensure that the endplate volume did not move into the cortical bone during loading. In contact element cases, all

regions where two adjacent volumes came in direct contact with each other were designated as contact element pairs.

The first four contact element pairs created dealt strictly with the cortical bone-endplate boundary while another two contact element pairs focused on the part interaction between the cortical and cancellous bone. In this particular case, the entire outer surface area of the cancellous bone and the inner surface area of the cortical bone were selected. In total, six different contact pairs were created.

In order to ensure that the endplates and the vertebral body bones remained in continuous contact with each other throughout the simulation, regardless of the type of loading, each of the contact pairs were setup so they remained bonded.

As the importing process from Pro-Engineer to Ansys may have inadvertently created some small gaps or overlapping between the cortical/cancellous region and cortical/endplate region, the contact elements were designed so any slight gaps or geometric penetrations were reduced automatically. In addition, steps were also taken to reduce gaps/penetrations that were somehow left out during the contact element creation process by physically moving individual elements to reduce gaps or penetrations.

Contact elements were also defined elements between the superior intervertebral disk surface and the inferior L3 endplate, and between the inferior disk surface and the superior L4 endplate. Figure 5-29 (a) displays the contact elements of the endplate and the cortical bone while Figure 5-29 (b) displays the

contact elements between the endplates and the intervertebral disk. Figure 5-30 displays the cortical/cancellous bone contact element interaction.

(a)   (b)
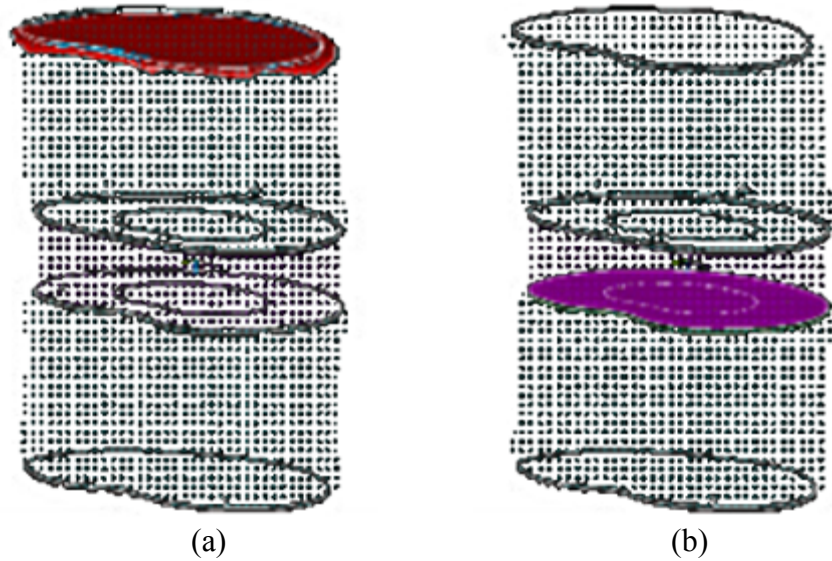
Figure 5-29: Image (a) displays the L3 cortical/superior endplate contact elements shown in red and (b) shows the L4 endplate and intervertebral disk contact elements shown in purple

(a)   (b)
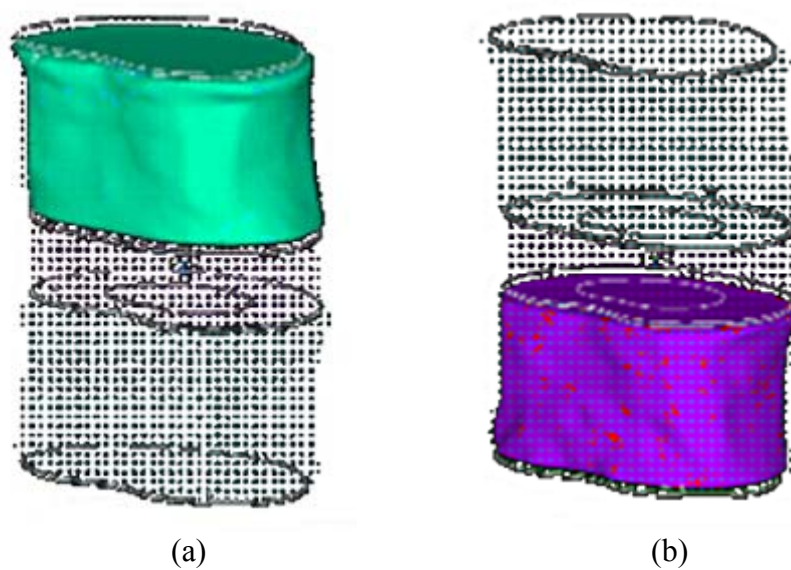
Figure 5-30: The green L3 (a) and purple L4 (b) cortical and cancellous bone contact elements the multicolored region indicates the target/contact elements in direct contact with each other

Finally, the surface areas between the nucleus and the innermost annulus layer were also designated a contact surface as shown in Figure 5-31. As the

layers of the annulus fibrosis were meshed as a single unit, no contact elements were required between adjacent layers.
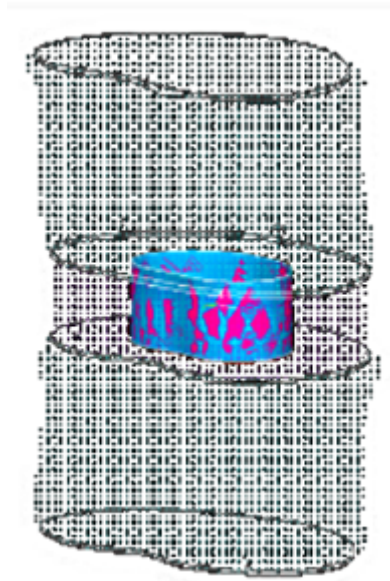
Figure 5-31: The contact elements between the innermost annulus layer and the nucleus of the intervertebral disk

5.4 Thermal Growth Code

Physically growing the FE model is not feasible given the current state of the Ansys software; therefore, it was determined that thermal expansion caused by thermal loads would be used as a growth mimicking procedure. In order to improve efficiency, a custom made code based in Matlab™ (Mathworks Inc., MA, USA) was created which could solve equations 5-1 and 5-2 for both vertebra bodies. Using compressive stresses in the z-axis of the cortical and cancellous bone for both asymmetric and symmetric loading as inputs, the code determines the growth of each element and thus the thermal load required to achieve that growth. The thermal loads are saved into a notepad file for each element so that a custom made macro can be created to allow for automatic thermal load

application into the FE model in Ansys. Appendix A provides a sample of this code and custom macro utilized to apply the thermal loads.

5.5 Finite Element Loading Conditions

5.5.1 Mesh Convergence Study

A mesh convergence study was conducted to determine mesh validity. The first part of the study involved the application of a uniform 1500N (1.274MPa) pressure load applied to the superior L3 endplate using a coarse and fine mesh of the geometry created directly from the Simpleware model.

Figure 5-32 provides a comparison of the fine and coarse mesh utilized for the mesh convergence study while Figure 5-33 and Figure 5-34 displays a comparison of the stress magnitude/distribution of the two cortical and cancellous bone models respectively. Figure 5-35 provides a plot of the total vertical displacement seen by the L3 vertebra for both mesh densities. Although there are slight variations in geometry between the mesh convergence model and the final model utilized in the scoliosis study, the coarse mesh model possessed similar element counts to the final model while the fine mesh model had nearly double the number of elements.
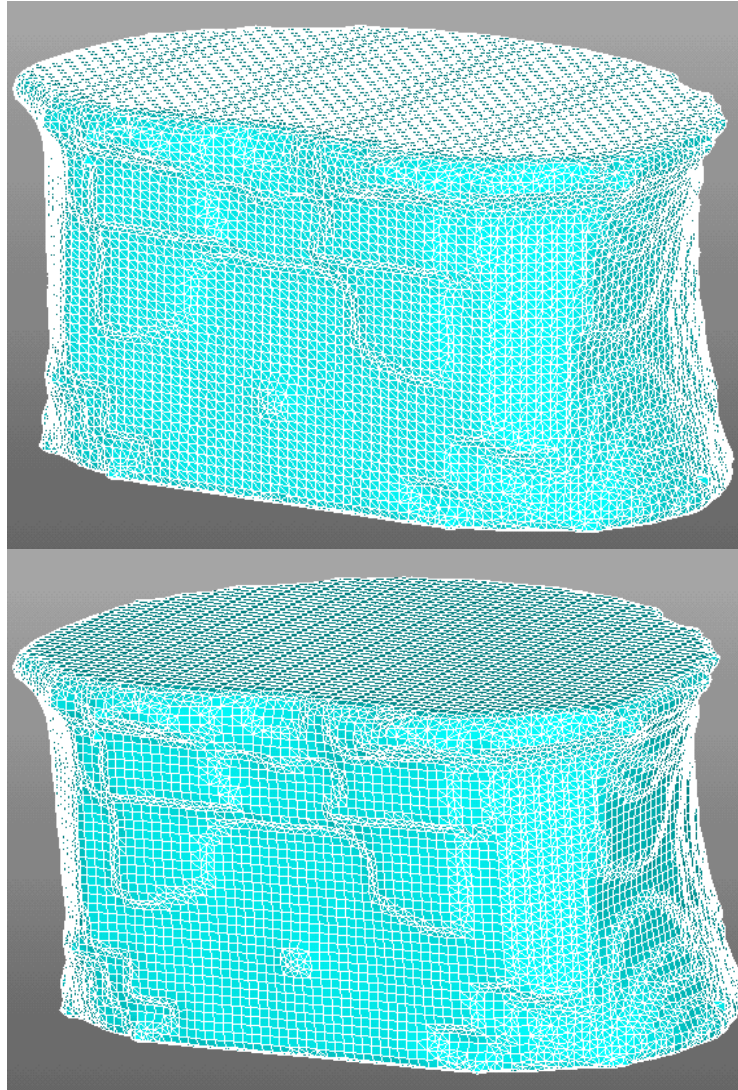
Figure 5-32: The L3 vertebral body with a fine mesh (top) and coarse mesh (bottom) applied

<div align="center">(a)   (b)</div>
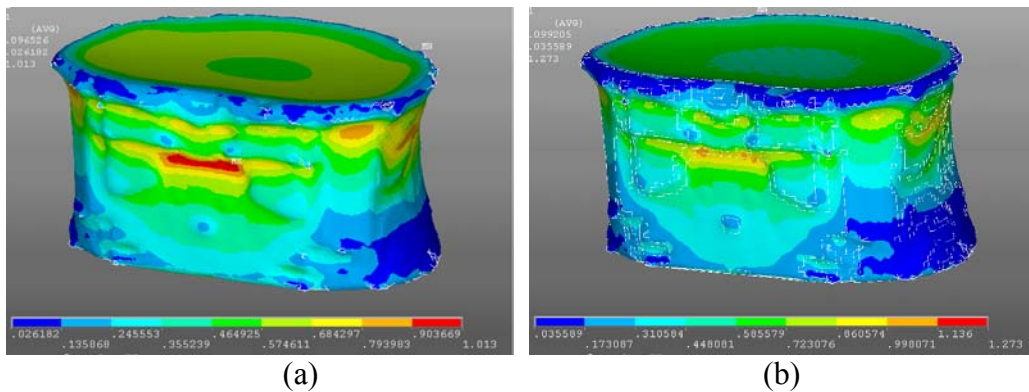
Figure 5-33: Images of the cancellous bone Von Mises stress distribution (MPa) under a (a) fine and (b) coarse mesh when placed under identical 1500N loads

(a)   (b)
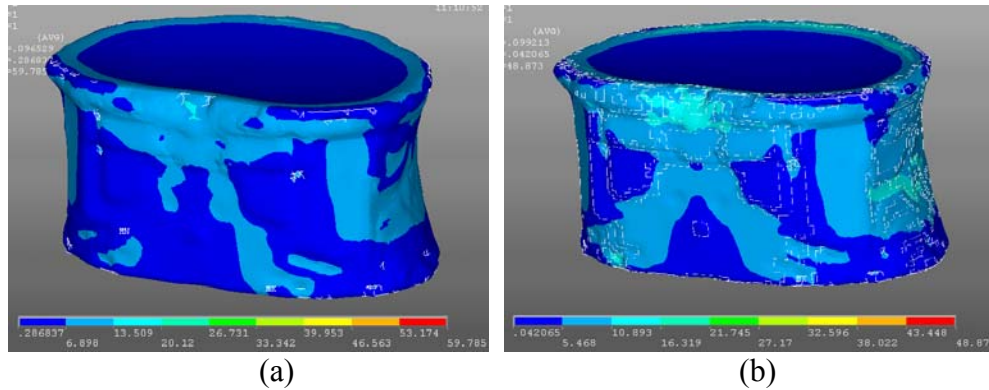
Figure 5-34: Images of the cortical bone Von Mises stress distribution (MPa) under a (a) fine and (b) coarse mesh when placed under identical 1500N loads

(a)   (b)
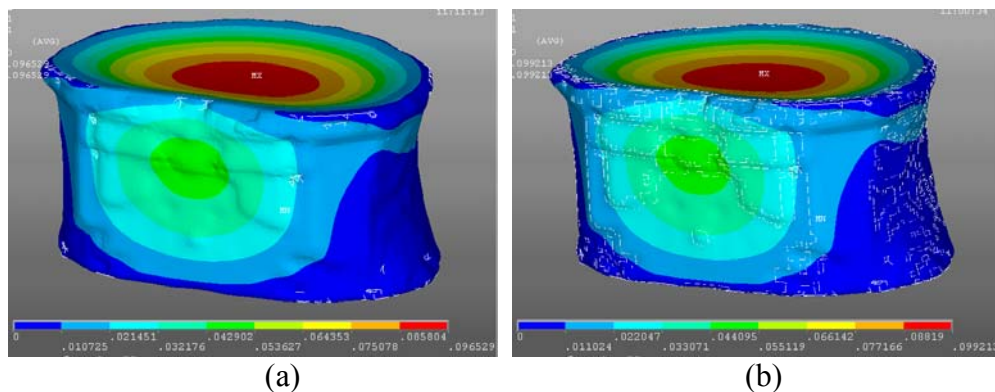
Figure 5-35: Images of the total displacement (mm) seen by the (a) fine mesh and (b) coarse mesh vertebral body when under identical loading conditions

As can be seen from Figure 5-33 and Figure 5-34, the general stress distribution between the two models remained constant regardless of the mesh density. A majority of variation between the coarse and fine mesh arose due to the differences in geometry created due to element sizes. Stress magnitudes also remained relatively consistent with the most predominant stresses in the cortical bone (the light and dark blue areas) and cancellous bone (teal and green regions) having a maximum variation of 15%. From the displacement plot shown in Figure 5-35, it can be seen that the total displacement seen by the two models are nearly

identical with a difference of less than 3%. Theoretical hand calculations[1] seen in Appendix B demonstrate the expected stress of the similarly sized cylinder when placed under a 1500N pressure load is 16.43MPa for the cortical bone and 0.29 MPa for the cancellous bone while the expected total displacement of the vertebral body is approximately 0.96mm. Comparing the stress and displacement values, it can be seen that both FEA models report similar average stress values and displacement magnitudes with the finer mesh reporting slightly more accurate results.

While it could be argued that the idealized co-axial cylinder model provides similar results to the created FSU model and thus should be utilized as it provides similar results with reduced complexity, it should be noted that the co-axial cylinders do not reflect the change in cross section seen in the vertebral body.

Given the dramatically increased computational time and processing power required to solve the fine mesh vertebra body, it was determined that the use of an extremely fine mesh would not yield significantly improved results. Consequently, the coarser vertebral body mesh was used for the remainder of the study.

5.5.2 Vertebral Body Validation Study

Prior to testing the entire functional spinal unit, a pilot study tested the L3 vertebra to determine if the defined contact elements functioned as expected. This is done to ensure that the cartilage endplates did not move into the vertebral body

---

[1] Theoretical stress is defined as $\sigma = F/A$, theoretical displacement is defined as $\delta = FL/AE$

bone when loading is applied to it. If the contact elements responded to loading correctly, then a full study of the FSU would be conducted. To guarantee convergence of the model, a displacement of 0.5mm was applied to the superior endplate while the inferior endplate was fixed in all directions.

As can be seen in Figure 5-36, the vertebral body behaved as expected with the softer endplate deforming under the displacement load. This in turned causes deformation and stresses within the vertebral body itself. This behavior indicates that the contact elements utilized in the study functioned correctly and can be applied to the entire FSU in future studies.
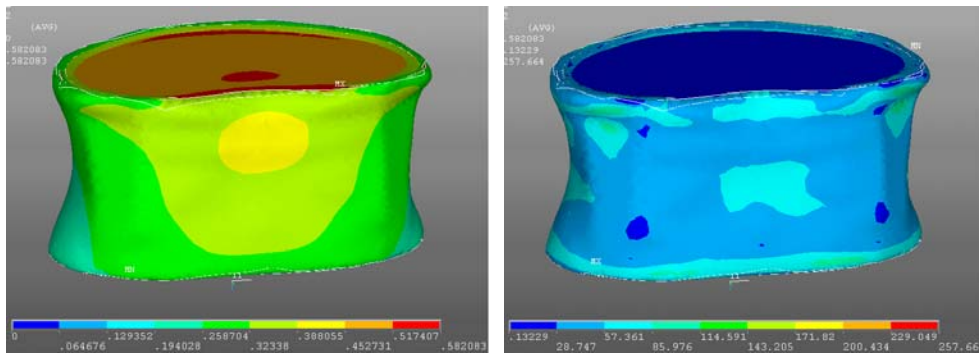
Figure 5-36: A deformation plot (left) and von Mises plot (right) of the L3 vertebra placed under a 0.5mm displacement. As can be clearly seen on right image, even though no direct load is applied to the vertebral body internal stresses are emerging. This indicates that the loads are being transferred from the endplate to the vertebral body

Once the behavior of the contact elements are established, a stress analysis can then be conducted. In order to ensure no point loads (loads applied at an infinitely small area on the model surface, thereby causing stress concentration factors) were generated, a pressure or distributed load was used. This method applies a perpendicular load on the entire superior surface of the L3 endplate, eliminating the risk of point loads and ensuring that there would be no abnormal vertebra behavior due to the way in which the load was simulated. An equivalent pressure load of 1500N (or 1.274MPa) was applied and compared to available

data. The pressure load was applied perpendicular to the superior endplate while the inferior endplate was fixed in all directions. Figure 5-37 (a) displays the contact element validation study while (b) displays the stress analysis study used in the validation procedure.

<div align="center">(a)   (b)</div>
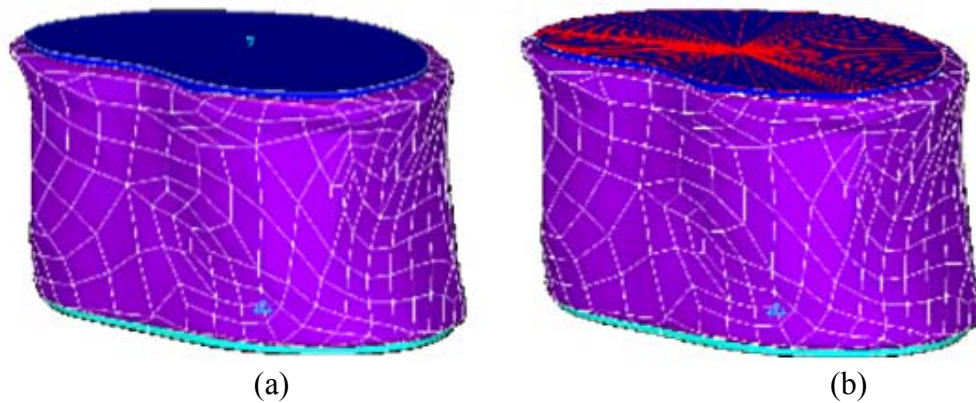
Figure 5-37: The displacement (a) and pressure (b) loads applied to a single vertebra. The displacement constraints/loads are shown in blue and the pressure loads shown in red

Once the stress distribution data is collected, the L3 model is compared to the L1 model developed by Li et al. Figure 5-38 displays the two results when placed under an identical 1500N pressure load.
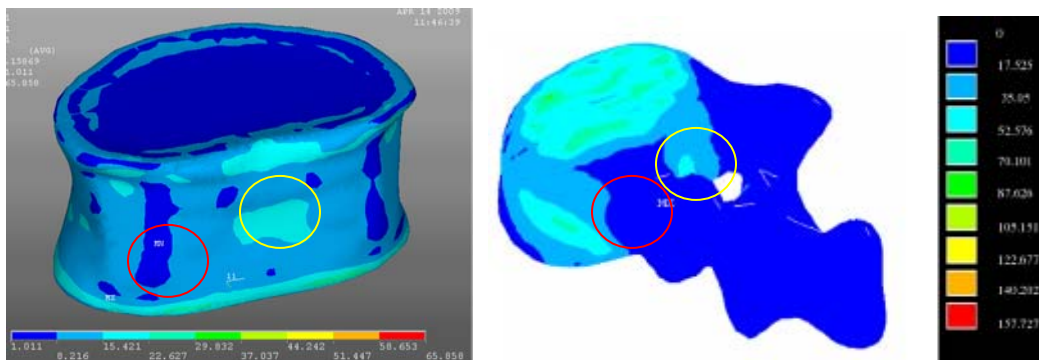
Figure 5-38: The von Mises stresses (MPa) of the L3 (left) vertebra developed in this study compared with the L1 vertebra (right) developed by Li [7] when placed under identical loads. Note that the L3 vertebra has the endplates stripped, showing just the bone.

As can be seen, while there are some similarities between the two cortical bone models such as low stresses at the point of pedicle attachments (circled in red) and a high stress pocket in the vertebral body region between the pedicle

attachments (circled in yellow), there are a great deal of discrepancies. The most evident is the radical differences in stress values. Temporarily ignoring the maximum stress values that arise due to geometric artifacts that create stress concentration factors, it can be seen that the average stress of the vertebral body determined in this study is approximately 12MPa while the model developed by Li possesses an average stress value of 52MPa. Note that the average stress values were compared as opposed to the maximum stress value so that stress concentration factors due to geometry are not considered.

When only analyzing the cancellous bone component and comparing the von Mises stress distribution between the two models (Figure 5-39), it can be clearly seen that the stress distribution better resembles Li's. Unlike the cortical bone model, it is evident that the superior surface of the cancellous bone undergoes greater stress relative to the rest of the cancellous body. In addition, there are still visible peaks of stress on the lateral sides of the vertebral body, a result which is in agreement with Li's model. Nevertheless, the 'average' stress magnitudes between the two models continue to differ greatly (about 0.5MPa achieved in this study versus 52MPa determined by Li).

Again referring to theoretical stress[2] calculations shown Appendix B, it can be seen that under identical loading conditions, an idealized vertebra represented by an outer cylinder enclosing a smaller cylinder would yield a stress value of 16.43MPa for the hollow cylinder and 0.29MPa for the smaller solid cylinder (if similarly sized to the L3 vertebra developed in this study). These

---

[2] Theoretical stress equation defined as $\sigma = F/A$

results indicate that the current modeling method and the applied material properties yield appropriate results. The results are further supported by literature which states that cortical and cancellous bone cannot be neglected during FEA [43, 44].
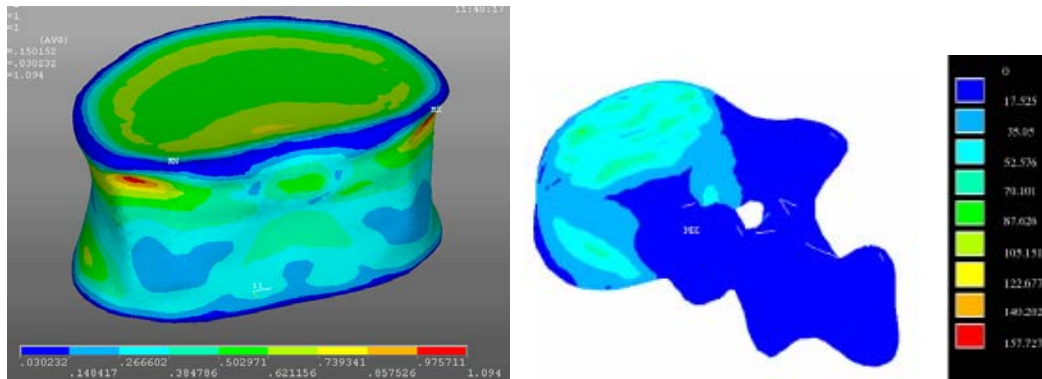
Figure 5-39: Von Mises stresses in the cancellous bone (left) of the L3 vertebra compared to the L1 vertebra created by Li (right). Units are in MPa

In addition to simplifications in material property allocation, Li's model also lacks surface definition. This in turn can cause differences in stress distribution. Figure 5-40 displays a side by side comparison between the FSU developed during the course of this study and Li's. As can be seen, due to the relatively low element count for each vertebra, there is a loss of geometric definition that could cause the discrepancies.
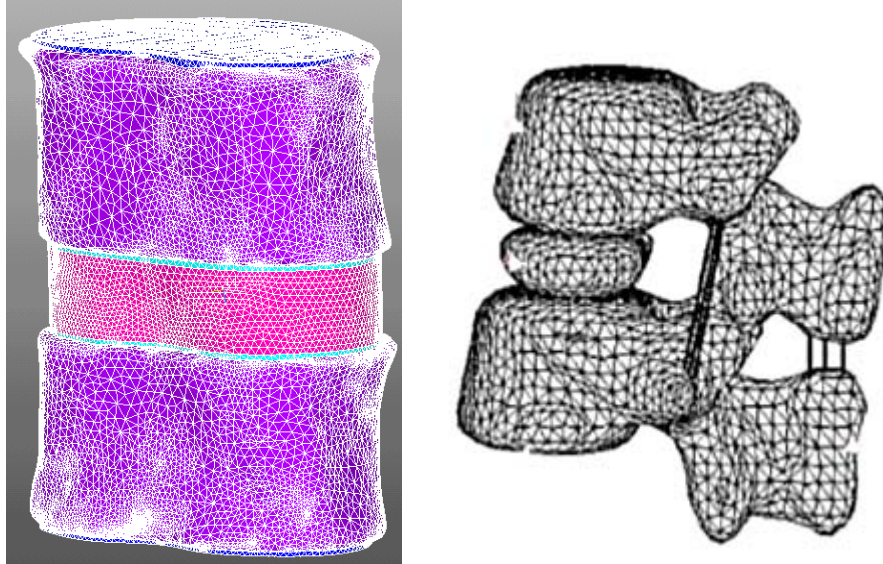
Figure 5-40: The FSU developed during this study (left) and the FSU developed by Li [7] (right)

It could be argued that Li's model provides a more accurate representation of the vertebral body geometry due to the presence of posterior elements. However, as demonstrated in Figure 5-38 and Figure 5-39, the posterior elements played no part in the vertebral body stresses due to the uniform compressive loading utilized by Li and given that the same loading conditions are applied, there is no reason to suspect that this model will produces stresses in these elements as well. Consequently, when focusing on just the vertebral body stress distribution and magnitude for axial loading only, the addition of posterior elements appeared to have no effect on the model.

Although the stress values achieved from this study do not agree with the values reported by Li, they are in agreement with theoretical hand calculations. In addition, the stress distribution with the cancellous bone does appear to follow Li's results. This demonstrates that the geometry of the vertebra responds appropriately to loading. The differences in stress magnitudes however, reinforce

what has been previously stated in literature regarding the importance of modeling both the cortical and cancellous bone during FEA analysis.

5.5.3 Effects of Cartilage Endplates on Vertebral Body Stresses

As there have been no previous studies conducted on the effects of the cartilage endplates on vertebral body stresses, a preliminary study into the importance of the endplates was first conducted. Using a 1500N equivalent pressure load, the endplates of the L3 vertebra were stripped from the cortical bone and the load/constraints were applied directly to the bone. The resulting stresses of the cortical and cancellous bone are then compared as well as total vertical displacement. Figure 5-41 displays the cortical bone stress, Figure 5-42 displays the cancellous bone stress levels and Figure 5-43 displays the total vertical displacement of the model with endplates and without endplates attached.
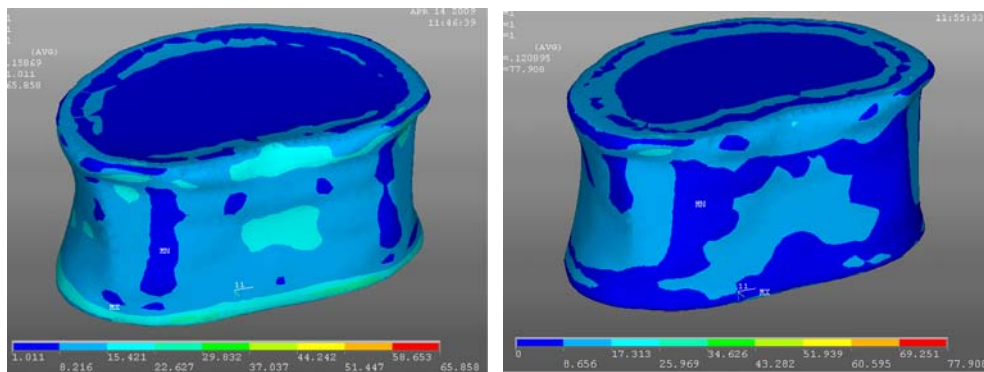
Figure 5-41: Von Mises stress (MPa) of the vertebral body with endplates (left) and without endplates (right)
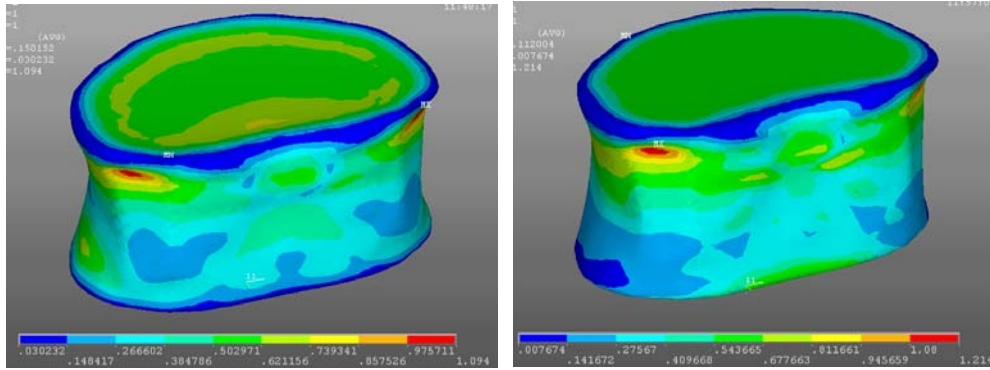
Figure 5-42: Von Mises stress (MPa) of the cancellous bone with endplates (left) and without endplates attached (right)
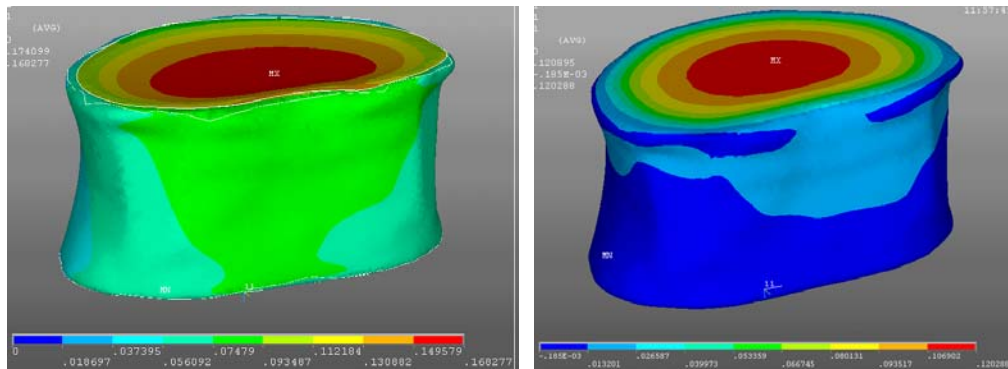
Figure 5-43: Total vertical displacement (mm) of the vertebral body with endplates (left) and without endplates attached (right)

As can be seen from the above images, the presence of the endplates moderately affects the stress distribution within the vertebral body. However, it is suspected this is due more to the manner in which the loading conditions were applied. For the vertebral body with an endplate attached, the pressure load was applied to the flat surface of the superior endplate. In the instance of no-endplate, the pressure load was applied to all flat surfaces on the superior vertebra surface. This may result in load application that is not on the same area. Despite this discrepancy, stress magnitudes remained relatively constant with the 'average' cortical bone stress of 8.2MPa in the model with endplates versus 8.6MPa in the model without endplates and an 'average' cancellous bone stress of 0.32MPa with

endplates and 0.34MPa without endplates. These values translate to a less than 6% difference in stress magnitude.

The greatest discrepancy between the two models can be seen in the vertical displacement. Without the endplates, the maximum vertical displacement of the vertebral body is 0.12mm. At the same location with endplates this value increases to 0.168mm. This increase is due to the flattening of the endplates as a result of the applied load and consequently, can affect the response of the FSU during applied loading.

In order to maintain as much physiological accuracy as possible, the endplates will continue to be utilized for the remainder of this study.

5.5.4 Intervertebral Disk Validation Study

The contact elements found within the intervertebral disk serve to simply ensure that the contact between the nucleus and the annulus regions of the disk are both displaced the same amount under loading. As a result, no displacement study was required as a simple pressure load would be sufficient. The inferior surface of the disk was constrained in all directions while the superior surface of the disk is constrained in the x-y plane only. This additional constraint is included to simulate the presence of a cartilage endplate on the disk which would limit the disks' motion in the transverse plane. This will ensure that the intervertebral disk 'bulges' as oppose to flatten (turning into a regular trapezoid) as the former is a physiologically geometric characteristic. An equivalent pressure load of 1000N was applied to the disk to determine stress magnitude and distribution while disk displacement and bulging was tested using an equivalent 500N load. The resulting values are recorded and compared to literature values.

For the disk modeling to be considered valid, several key features must be observed after loading: 1) Lateral disk bulging, 2) vertical deformation in agreement with literature values and 3) stress distribution/magnitude values in agreement with literature values.

As demonstrated in Figure 5-44, lateral bulging clearly occurs when the disk is placed under uniform compression load, a characteristic that has been observed and discussed in Chapter 2. The value of the lateral bulging is compared with *in-vitro* studies recorded by Heuer et al. [45].
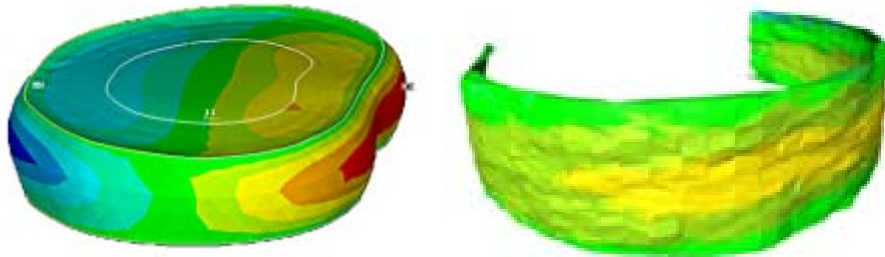
Figure 5-44: The amount of annulus bulging seen by the intervertebral disk under uniform pressure load. The image on the left is the disk created in this study and the image on the right the disk created by Heuer [45] displacement plot

Heuer determined that under a 500N load, the disk bulge will be approximately 0.7mm radially. This model possesses a disk bulge of roughly 0.55mm. This corresponds to about a 20% difference between the finite element model and the biological specimen, a value that is not unreasonable for biological tissues and with the assumptions used. This is indicative of the annulus fibers responding to the loading appropriately. A potential source of discrepancy between this FE model and the *in vitro* study is the orientation of the fiber angles. From the Heuer's study it was determined that the fiber angles vary depending on their location within the annulus region (26^0 to 46^0 with respect to the x-y plane). In addition, the material properties of the FE model are an approximation of the

visco-elastic behavior of actual intervertebral disks. Differences could also be attributed to differences in geometry and disk sizes.

Another test of the disks response under compressive loading is the analysis of total vertical displacement. Figure 5-45 below displays the vertical displacement seen by the disk when placed under a 500N pressure load.
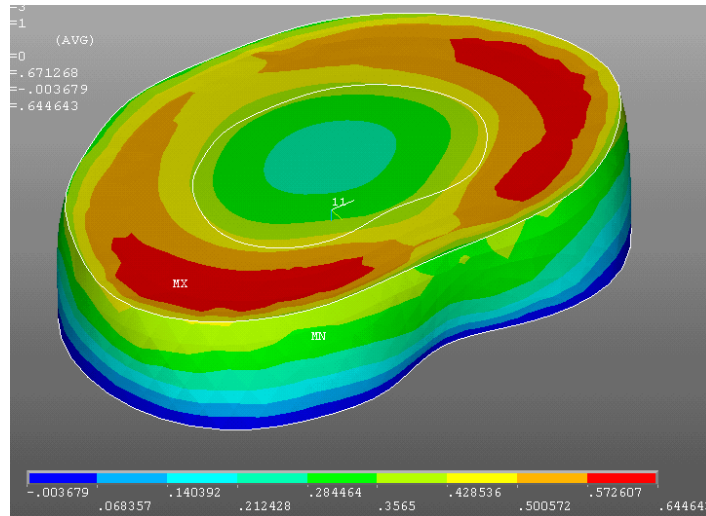
Figure 5-45: A vertical displacement plot of the intervertebral disk under a uniform pressure load

From studies conducted by Li, Yao, Wong and Fagan under a 500N uniform load the disk should deform anywhere between 0.4 to 0.6mm. According to Figure 5-45, the average vertical deformation observed by the disk is approximately 0.64mm, well within the range provided by the literature.

Using Li's disk modeled as a basis for stress distribution/magnitude validation, Figure 5-46 displays the resulting von Mises stress plots of a disk placed under a 1000N load.

103
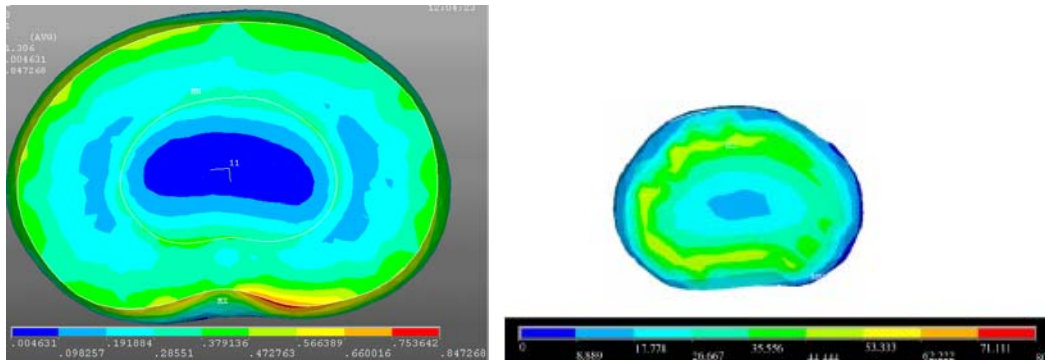
Figure 5-46: A comparison between the von Mises stresses (MPa) in the intervertebral disk developed during the course of this study (left) and the model developed by Li (right).

As with the vertebral body, Li chose to model the intervertebral disk as a single material, neglecting the annulus fibers and the differences between the nucleus and the annulus regions. As can be seen from the two models, the stress distribution within the disks are similar despite the fact that Li chose to model the intervertebral disk as a single uniform substance with no distinction between the annulus layers and nucleus pulposus. This simplified geometric and consequently, material property allocation of the intervertebral disk also resulted in Li achieving different von Mises stress readings. The 'average' stress value seen in the intervertebral disk modeled in this study is approximately 0.50MPa while the average stress observed by Li was 45MPa. As done with the vertebral body and shown in Appendix C, theoretical calculations[3] utilizing idealized geometry yielded a stress result of approximately 0.85MPa if the cross sectional area is assumed to remain constant. However, in order to get a more accurate comparison between theoretical stress magnitude and the values achieved by the FE study, then the increase in cross sectional area must also be taken into account. If the

---

[3] The theoretical stress is defined as $\sigma = F/A$, where σ is the stress value, F is the applied force and A is the cross sectional area of the intervertebral disk at the region interest.

effects of bulging are included in the calculation it can be seen that the resulting theoretical stress will be approximately 0.80MPa[4], a result that is similar to the FE model.

This significant difference in stress values suggests that that Li's reported values were mistakenly labeled. Despite this, it can be seen that the stress distribution achieved in this study appears similar to the one developed by Li with the nucleus possessing lower stress values than the surrounding tissue and a higher stress ring around the nucleus.

With the stress distribution of this study matching the one developed by Li, and the stress magnitudes comparable to theoretical hand calculations, it is believed that the disk will respond appropriately within the functional spinal unit and will adequately transfer the forces from the upper vertebral body to the lower.

5.5.5 Functional Spinal Unit Validation Study

After evaluating individual components, the entire functional spinal unit is evaluated. As with the previous studies, the inferior endplate surface of the L4 vertebra is fixed in all directions while a pressure load is placed on the superior endplate of the L3 vertebra. No additional constraints are required on the intervertebral disk as the contact elements restrain motion in all directions. Load increments of 500N, 1000N and 1500N are placed on the FSU and the displacements recorded for comparison with the literature ([7, 41, 53, and 58]). Figure 5-47 displays the FSU finite element model with an equivalent 500N

---

[4] This assumes a disk bulge and consequently a radius increase of 0.55mm. The disk is assumed cylindrical

pressure load applied to the L3 superior endplate along with all relevant constraints.

Figure 5-47: The FSU loading conditions with a pressure load shown in red and the constraints shown in teal

Figure 5-48 displays a sample displacement and stress reading of a uniform 500N equivalent pressure load applied to the FSU. Figure 5-49 displays the graphical results of the study along with comparisons with other research data.
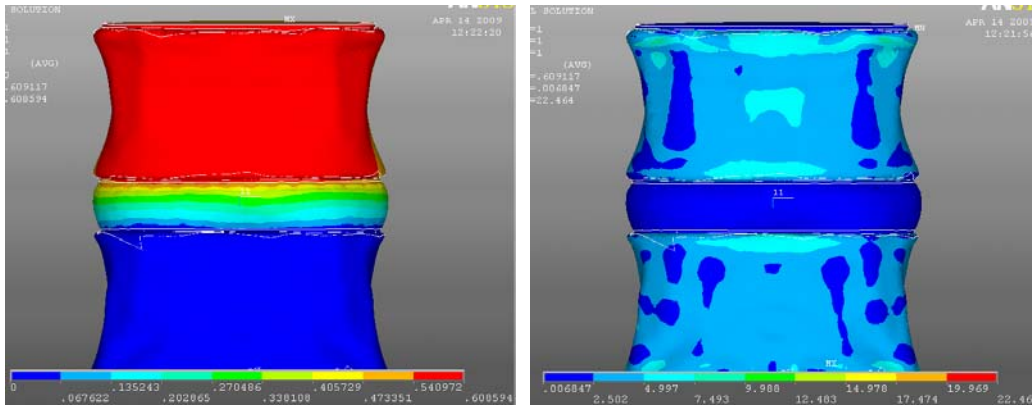
Figure 5-48: Displacement plot (left) and von Mises stress plot (right), in mm and MPa respectively, of the functional spinal unit under a uniform pressure load
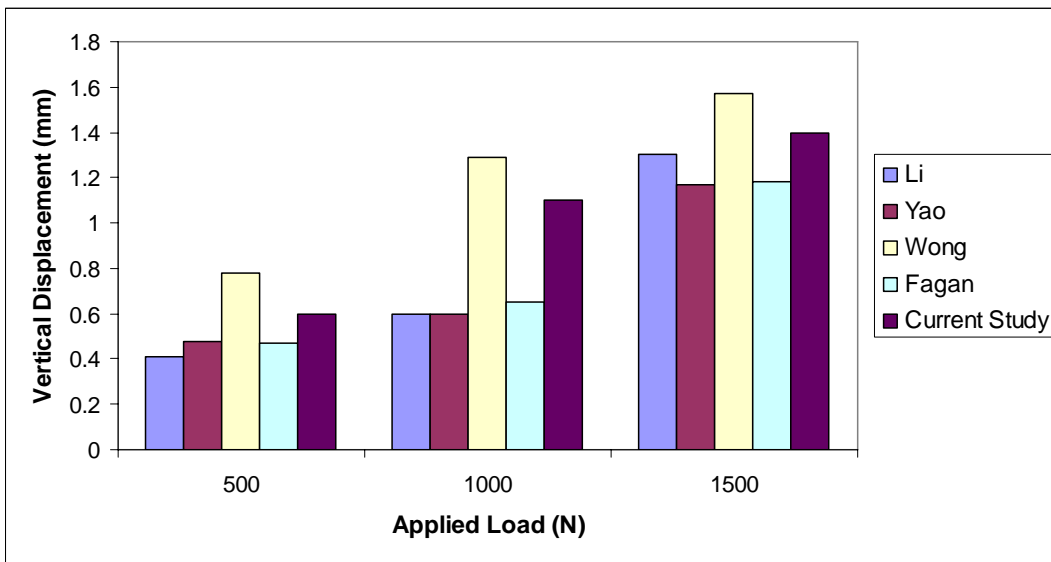
Figure 5-49: Graph of FSU displacement versus applied load comparisons

As can be seen from Figure 5-49, the FSU developed in this particular study responds to compressive load in a similar manner as the models developed by other researchers. Variations of data can be attributed to differences in material property assignment to the intervertebral disk as well as the presence of endplates on this particular model. While total FSU stress values could not be independently verified from literature as done with the vertebral body and Li's model, the displacement results achieved in this study, in addition to the stress comparison done on a single vertebral body, suggests that the current model setup adequately

107

models the biomechanical response of the spine in accordance with previously established literature.

5.5.6 Conclusion

With the biomechanical model verified and demonstrating that it is physiologically similar to previously established spine biomechanics models, the FSU can now be applied to scoliosis research, more specifically the 'vicious cycle' theory. This procedure would involve the application of the symmetric and asymmetric loading on the vertebral body, solving and comparing the stress levels to determine the amount of biomechanical growth each region of the vertebral body undergoes.

Chapter 6
Scoliosis Growth Pattern – Case Study

With the accuracy of the spine biomechanics of the generated model established, it is now possible to apply the FSU to a scoliosis model. This section will detail the procedure utilized to test the vicious cycle theory as well as the results achieved from the case study. The resulting model will be compared with available literature data from Villemure, Stokes and other researchers. Model limitations in terms of its applicability to scoliosis research will also be discussed.

6.1 Scoliosis Growth Model

6.1.1 Growth Procedure

Unlike the spine biomechanics validation studies, physiological loading conditions that reflect the spine loads of an adolescent can be applied. The growth model requires five steps to simulate each 'year' of study:

(1) Application of physiological symmetric loading conditions as seen in healthy, non-scoliotic spines;

(2) Application of asymmetric loading conditions as seen in scoliotic spines;

(3) Applying the acquired stress data of each element achieved in steps 1 and 2 into equation 5-1 as σ_m and σ respectively. The resulting values are then used in equations 5-2 and 5-3 to determine the temperature needed to achieve the required growth measured as strain. The baseline biological growth used in this step varies as outlined in Section 5.1.3;

(4) Application of the temperature loads on the original FE model; and,

(5) Geometry update to the 'grown' FE model.

These steps are then repeated using the newest element geometry.

To accurately characterize forces applied to the L3 vertebra from gravitational forces, as well as stabilizing muscle forces; and to reduce load application complexity, it was determined that an equivalent load of 614.3N [32, 46], equaling to about 0.52MPa of pressure on the superior L3 endplate would be applied. This value is valid for an adolescent with a mass of approximately 45kg at the L3 vertebra level. For asymmetric loading conditions, a distributed load was applied to the superior endplate with minimum of 614.3N is applied at one side of the vertebral body, increasing linearly to a maximum of 637.65N or 0.54MPa of pressure. This maximum value represents the load applied on the healthy L4 vertebra, calculated by Villemure and Nachemson [59] by placing a pressure transducer within the intervertebral disk at the region of interest. An example of the asymmetric loading conditions can be seen in Figure 6-1.
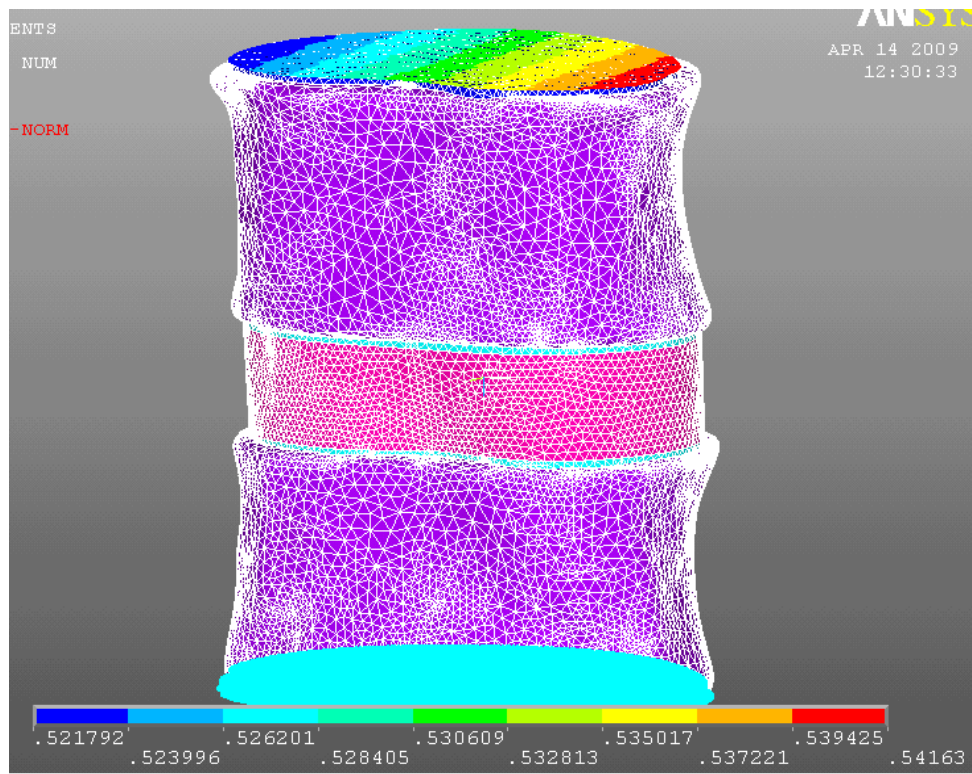
Figure 6-1: Asymmetric loading of the FSU. Red indicates a higher load while blue indicates the lightest load value.

In accordance with the available data seen in Table 5-3, a total of three 'years' of growth iterations were applied to the spine model.

6.1.2 Scoliosis Growth Model Results and Validation

For the scoliosis growth model to be accurate, it must be validated against both actual patient data as well as previous scoliosis FE studies, especially growth models that focus on asymmetric loading as a cause of scoliosis growth. Based on studies done by Stokes [30-31], Villemure [32, 46] and Lafortune [33], scoliotic spines could be created through the use of asymmetric spinal loading and all researchers used a variation of the growth modulation equation discussed in Chapter 5.

Figure 6-2 displays the effects of asymmetric loading on the spine with the region undergoing greater loading resulting in less growth relative to the lighter

loaded areas, a growth pattern that follows scoliosis progression. Figure 6-3 provides a direct comparison of the change in height of the vertebral bodies as the study progressed from year zero to year three.
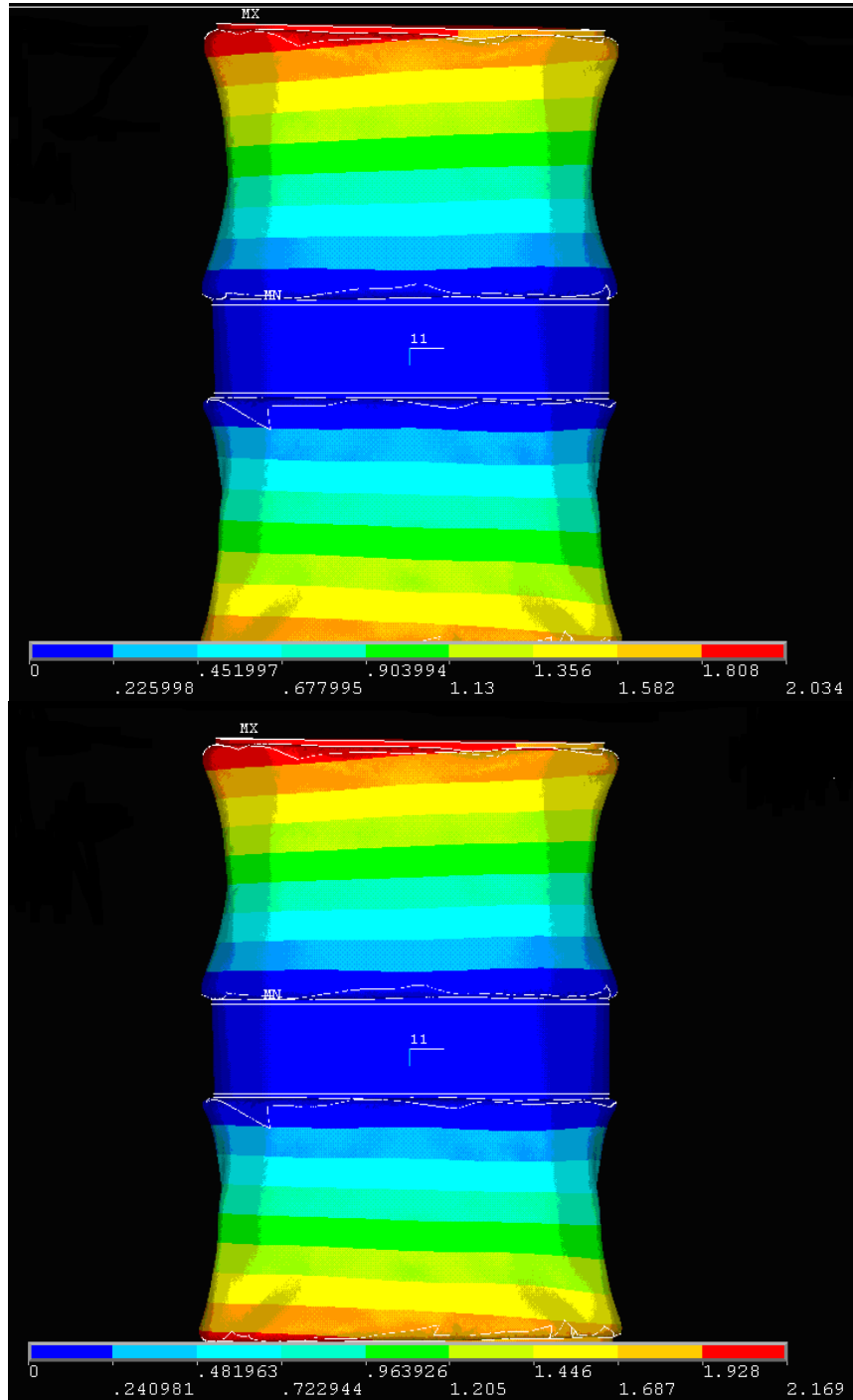
Figure 6-2: Deformed growth plots of the vertebral bodies after one year (top) and two years (bottom) from the previous year. The red region indicates increased growth. Units are in mm
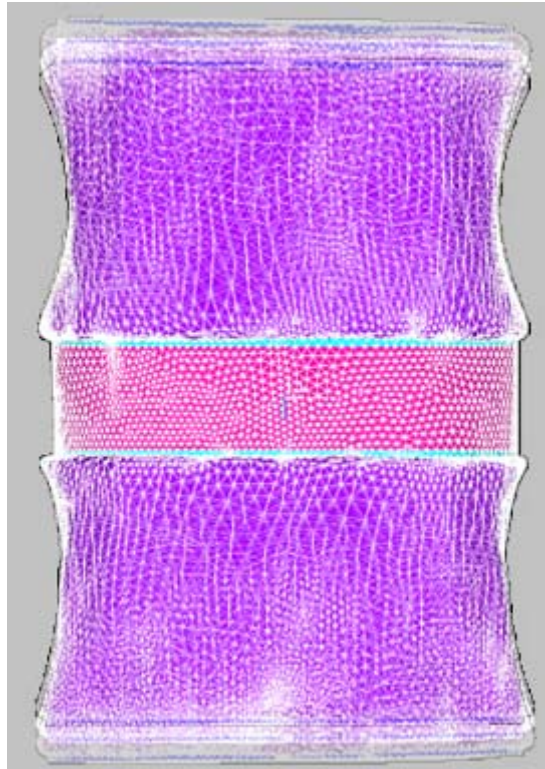
Figure 6-3: Change in vertebra height from year zero to year three

While using different loading conditions and only showing the final model after five years of growth, the two dimensional profile of this model does demonstrate similarities to the L3/L4 vertebra of Stokes model as shown in Figure 6-4.

When comparing Figure 6-3 and Figure 6-4, it can be seen that both models form a wedge shape towards the right. However, noting that the inferior surface of the L4 vertebra in Stokes' model is parallel to the horizontal plane, the same result can be achieved with this study by simply tilting the modeled FSU by the L4 wedge angle. This will produce a far more pronounced tilt as seen by Stokes model.
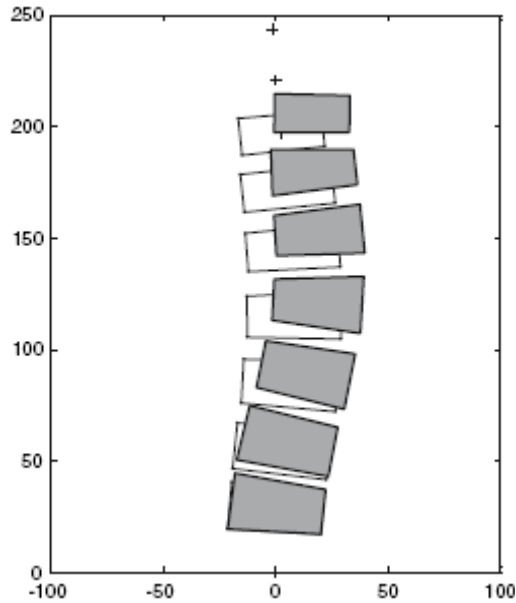
Figure 6-4: Scoliosis growth model of the T9-L4 vertebral column as developed by Stokes [31]. The outlined regions indicate the original scoliotic curve at year 1 and the grayed region indicates the curve after 5 years of growth

When a three-dimensional plot is used, as shown in Figure 6-5, it can be seen that asymmetric growth in the spine is not limited to the sagittal plane. While the anterior regions of the vertebra appears to grow slightly less than the posterior, it is evident that the asymmetric loading condition causes three-dimensional deformation. This type of three-dimensional growth behavior is consistent with scoliosis growth (referring back to Figure 2-14).
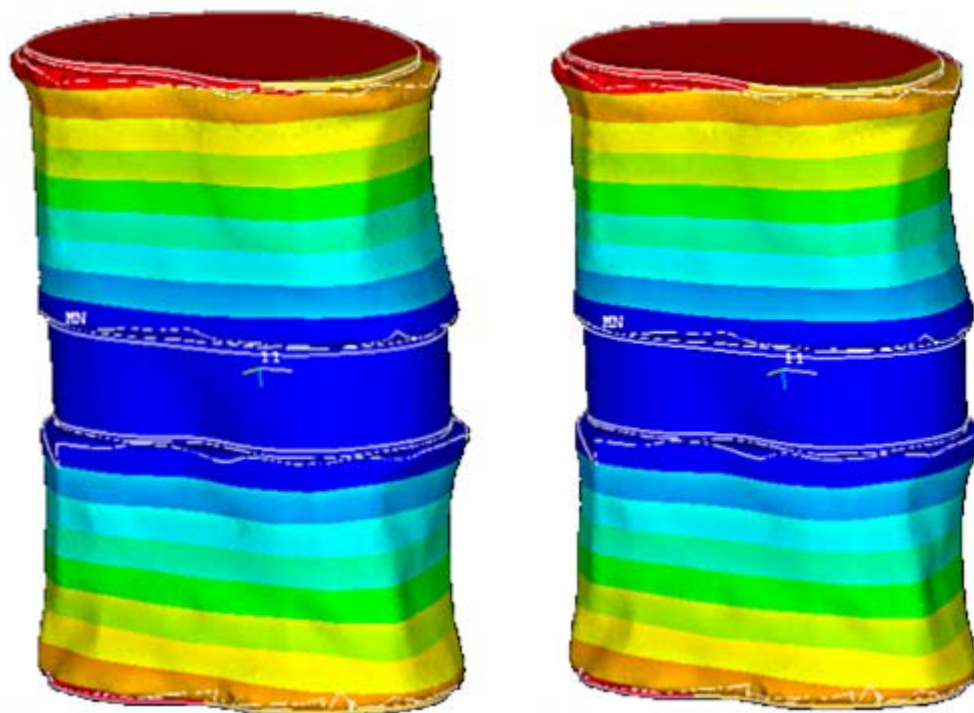
Figure 6-5: Vertical displacement plots of the FSU after one year of growth (left) and two years of growth (right)

As only a FSU was modeled in this study, a Cobb angle calculation is not possible. However, a study conducted by Lafortune analyzed the wedge angle of each vertebra of a scoliosis spine. The wedge angle was measured by finding the angle between a horizontal plane and the superior/inferior endplate surfaces. This measurement was achieved through the use of ImageJ™ (National Institutes of Health, US). Horizontal lines were first drawn on an image screen shot and then a slanted line that ran parallel to the endplate surfaces. The angle between the two lines is then calculated. Table 6-1 provides a summary of the angles achieved and Figure 6-6 provides a sample image.

Table 6-1: Annual FSU Wedge Angle Summary in Degrees

Year of Growth	Superior Wedge Angles	Inferior Wedge Angles
0	0	0
1	0.635	0.379
2	0.653	0.396
3	0.675	0.407
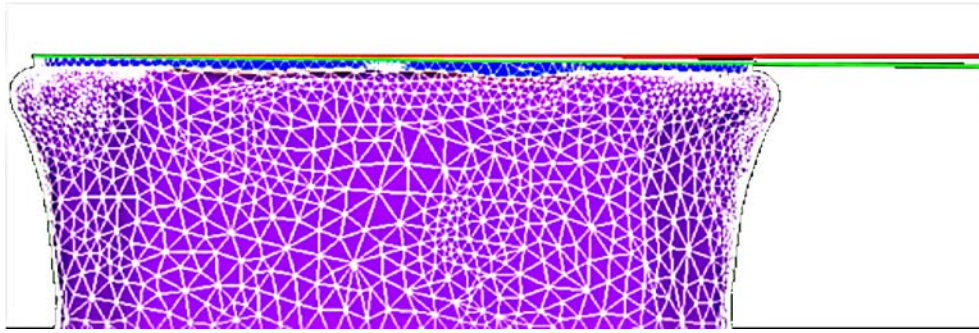
Figure 6-6: Wedging angle between two vertebral bodies before initiation of scoliosis. The green lines indicate the horizontal plane while the red lines indicate the slope of the endplates

As can be seen from Table 6-1, the wedge angle of both vertebral bodies increases steadily, as expected from consistent loading conditions.

Both Lafortune and Villemure measured the wedge angle at each level of the vertebra as a measure of scoliosis progression under various loads. Figure 6-7 provides a comparison of the wedge angles from each of the studies.
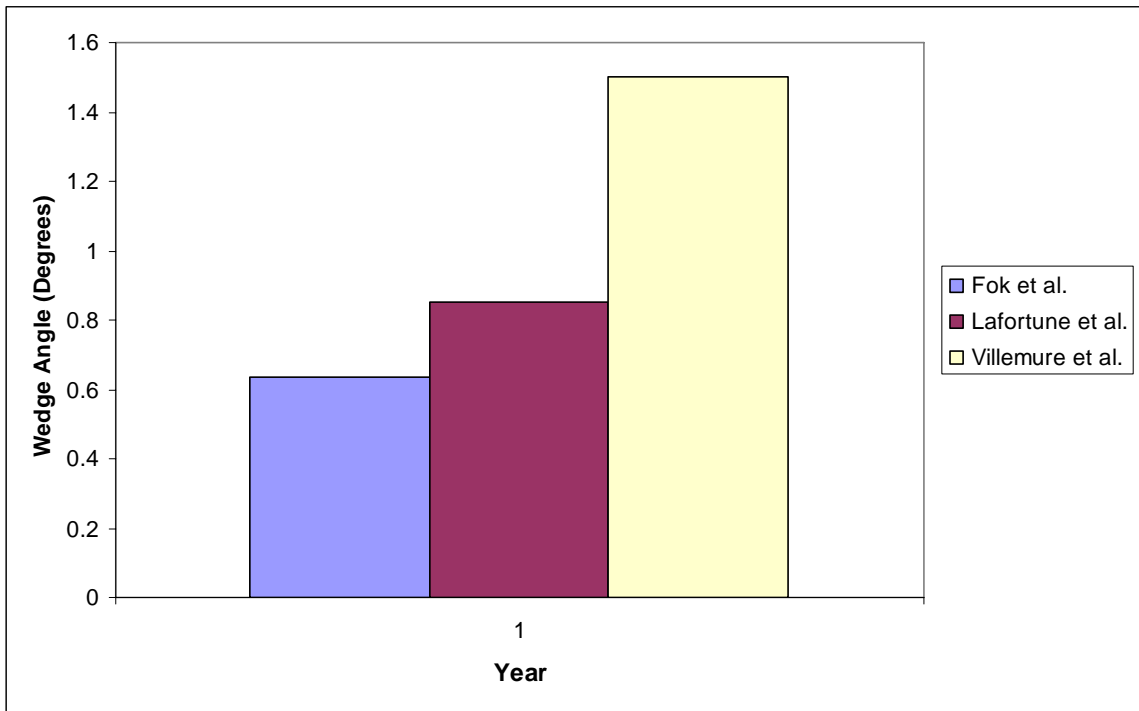
Figure 6-7: Wedge angles comparisons

116

As shown in Figure 6-7, the wedge angle of the L3/L4 vertebra in Lafortune's study translates to about 0.85º after a period of one year. No additional data was provided after a period of one year. Villemure's model indicates a maximum wedge angle of the entire scoliotic spine after one year is approximately 1.5º and after two years, a maximum wedge angle of 9º. This sudden increase in wedge angle is most likely due to the accumulation of wedging from multiple vertebral bodies as opposed to a single vertebra. In addition, Villemure gave no mention of where the maximum wedge angle was located and most likely reflects the accumulation of multiple vertebra wedge angles as opposed to a single vertebral body. If the cumulative wedge angles for this particular study are taken into account, then this study would see a maximum wedge angle of approximately 1.014º, a value similar to that of Villemure. Additional areas that could cause loading differences can be attributed to slight variations in loading conditions and differences in material properties, vertebra location, geometry and growth sensitivity factor.

6.1.3 Non-Progressive Scoliosis Growth

While scoliosis growth is clearly modeled by this spine model after three years, the simulation also suggests that given the current loading conditions, this particular scoliotic spine would be non-progressive. This hypothesis is most evident when viewing the temperature distributions of each vertebral body. Figure 6-8 displays a comparison of the spine model growth from year one to year three.
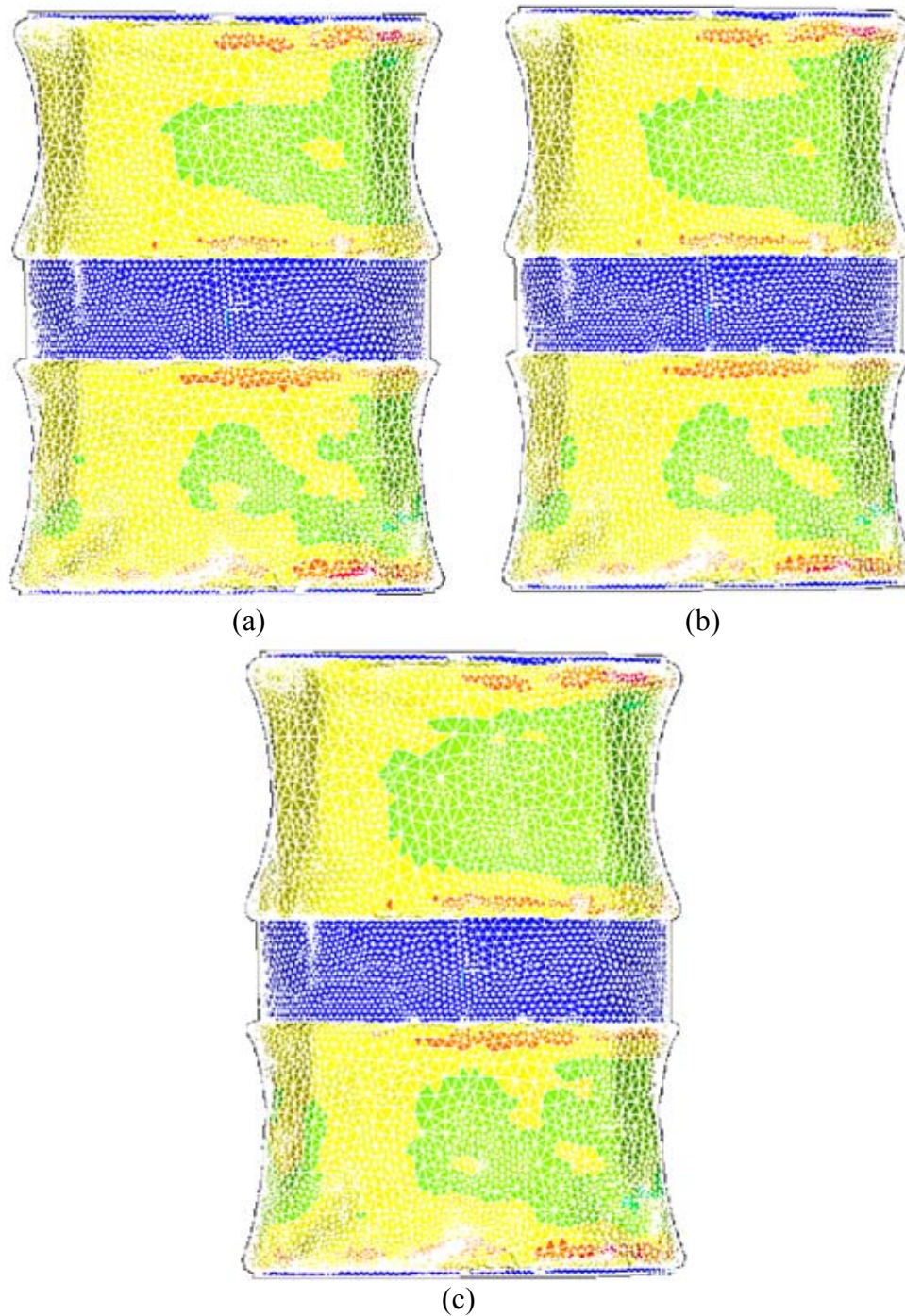
Figure 6-8: The temperature distribution of the spine after year one (a), year two (b) and year three (c). Temperature loads increase from blue (coldest) to green, yellow and finally orange/red (hottest).

The different colored regions indicate differences in thermal loading with yellow regions having a higher thermal load (and thus increased growth) than the green regions. As can be seen from image (a), it is evident that after one year the

left region of the spine is undergoing greater growth than the right due to the higher concentration of yellow. This type of growth behavior suggests the presence of a c-shaped scoliosis curve.

When viewing the thermal loads applied in year three however, it can be seen that the thermal distribution is becoming more uniform throughout L3 and L4 vertebras, with the green thermal regions (lower temperature) progressively getting larger. This indicates that a greater portion of the vertebral body is undergoing slower growth. Should this pattern continue, it can be suggested that at a certain wedge angle, the thermal load and therefore the growth rate throughout a region of the vertebra will be uniform. Consequently, this implies that the asymmetric load is potentially self correcting scoliosis curve should the simulations continue on past three years. This loading condition may also imply that the c-shaped curve seen by this FSU may also develop into an s-shape curve.

This hypothesis of a non-progressive or s-shaped scoliosis spine is supported by theoretical calculations (Appendix D). Referring to Figure 6-9 below, it can be seen that for uniform growth to occur the stress distribution along the entire cross section of the curved beam must be equal and constant throughout the entire length of the beam. Consequently, the moment due to the horizontal force (designated as P_x) must counteract the force due to the asymmetric load moment (M_a) and the moment due to the vertical force (P_y). Recall that the resultant load P is always applied perpendicular to the top surface of the cylinder/vertebra.
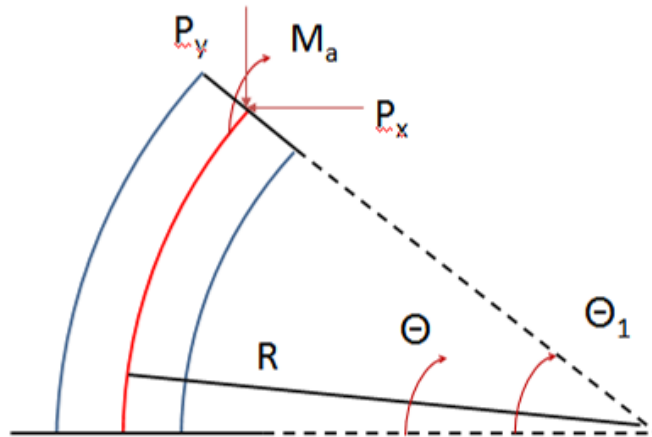
Figure 6-9: A curve cylinder with asymmetric loading applied to it. The compressive load (P) is broken down into vertical (P_y) and horizontal (P_x) forces. R represents the radius of curvature, M_A is the moment caused by asymmetric loading, θ_1 is the wedge angle and θ is the angle at the cross section of interest

As illustrated in Figure 6-9, as the beam curve or wedge angle (θ_1) progressively increases, so does the value of P_x and its moment arm while the value of P_y and its moment arm decreases. Consequently so long as the loading remains constant, there will be a wedge angle in which the summation of moments due to the applied loads and the moment due to asymmetric loading equals zero at a certain cross sectional area of the cylinder. At this region, only stress due to pure axial compression is present and therefore, the presence of uniform body growth.

In order to test this hypothesis, the stress values across the entire length of the cylinder (set as the same height as a single vertebral body), seen in Figure 6-9 was calculated using Microsoft Excel$^©$. It was determined that at a wedge angle of 0.511°, the bending stresses at the base (i.e. the fixed end) of the cylinder equaled zero. As this does not necessarily mean that the stresses throughout the vertebral body are also zero, stress calculations must be made along the entire length of the

120

curved beam. Figure 6-10 displays a plot of the compressive stress distribution along the cylinders' outer and inner edges, across its entire length. These calculations were conducted using identical loading conditions to that of the FE model and assuming that the body is composed of two co-axial cylinders: a smaller cylinder encompassed by a larger one. The applied loading was adjusted to reflect the load seen by only the cortical bone so that the theoretical stress values could be compared to that of the FE model. Figure 6-11 and Figure 6-12 provide a stress distribution plot of the same cylinder with a 0.311° and 0.711° wedge angle respectively.
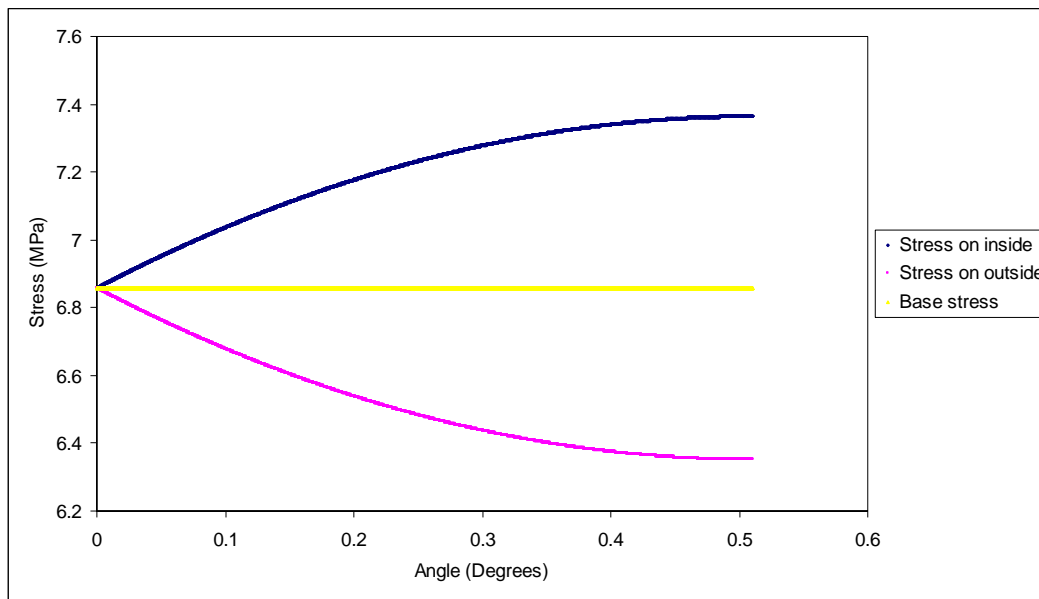
Figure 6-10: Compressive stress distribution of the outer and inner surface of the cylinder along its entire length with a wedge angle of 0.511°. The straight centerline indicates the stress due to purely axial loading only
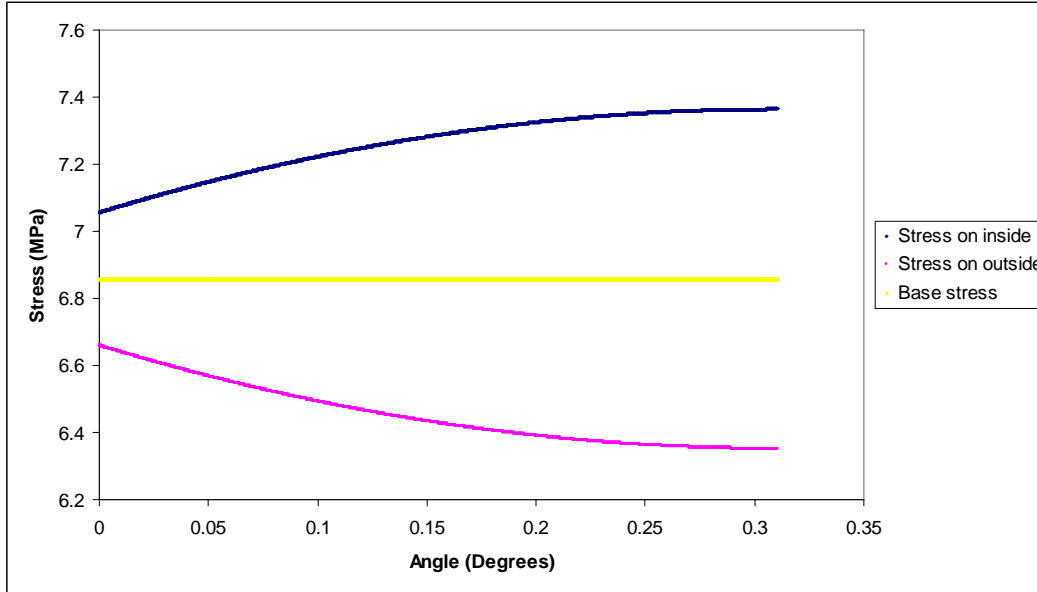
Figure 6-11: The stress distribution across the entire length of a curved cylinder possessing a wedge angle of 0.311°
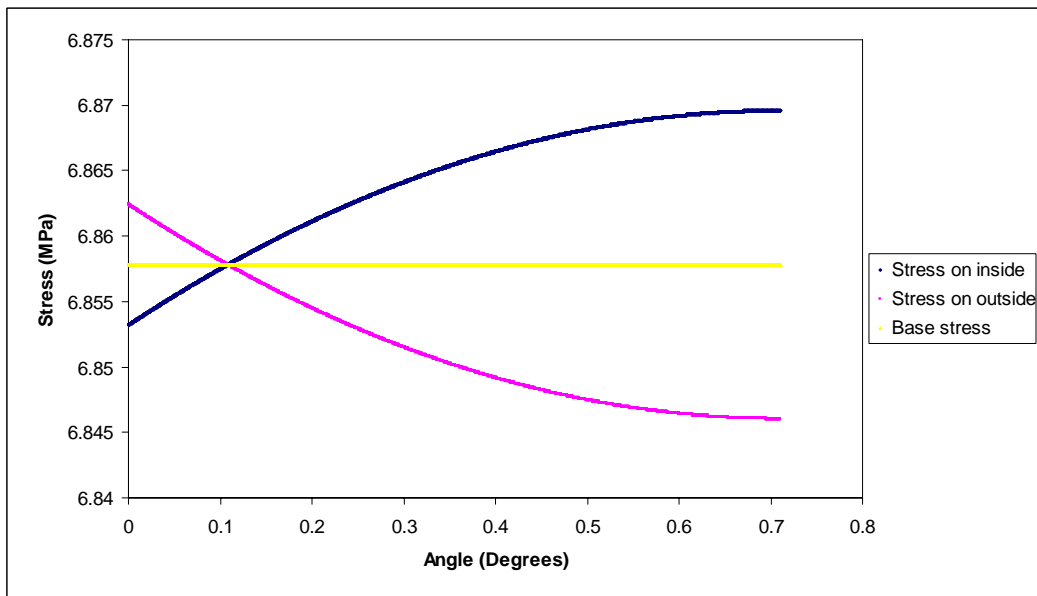
Figure 6-12: The stress distribution across the entire length of a curved beam possessing a wedge angle of 0.711°

Referring to Figure 6-11, it can be seen that the stresses along the inner curve of the cylinder is higher than that of the outer curve, indicating that this region is undergoing slower growth compared to the outer edge. This particular plot is in agreement with the thermal load plots shown in Figure 6-8 and is

indicative of asymmetric growth, with the body growing towards the right. By this analysis alone, it can be concluded that the FE model is responding in a physiologically sound manner.

As the wedge angle increases however, the behavior of the stress plots change. Looking at Figure 6-10, it can be seen that at the base of the cylinder (when $\theta = 0$), the stresses along the outer and inner edges of the cylinder are due to compression only. At this point, there would be uniform (i.e. symmetric) growth along the base of the body. However, as the angle θ increases, it can be seen that the asymmetric stress curve is still present, indicating that although the base of the cylinder is growing at a uniform rate, the upper portion of the body is continuing to wedge towards the right.

Figure 6-12 displays the same cylinder with a wedge angle of 0.711°. As can be seen from the plot, while the upper region of the cylindrical body appears to continue its asymmetric growth towards the right, the lower portion of the body does not follow this trend. As can be seen, the stresses along the inside curve of the cylinder are now lower than the stresses seen on the outside of the curve, essentially reverse from what was previously seen. This means that the inner curve is now undergoing greater growth compared to the outer curve, forcing the body to begin asymmetric growth towards the left. The stress distribution behavior suggests that the cylinder will at first grow towards the right and as the wedge angle continues to increase, the cylinder will then begin to grow towards the left. Should this trend continue there would be a certain angle at which the net growth of the cylinder would be uniform (i.e. non-progressive growth). It was

determined that at a wedge angle of 1.53º, the right asymmetric growth occurring in the top half of the body will be completely offset by the left asymmetric growth occurring in the bottom portion of the body resulting in zero net asymmetric growth. This switch in asymmetric growth direction occurs at roughly the midpoint of the cylinder. Figure 6-13 displays the stress distribution plot at this wedge angle.
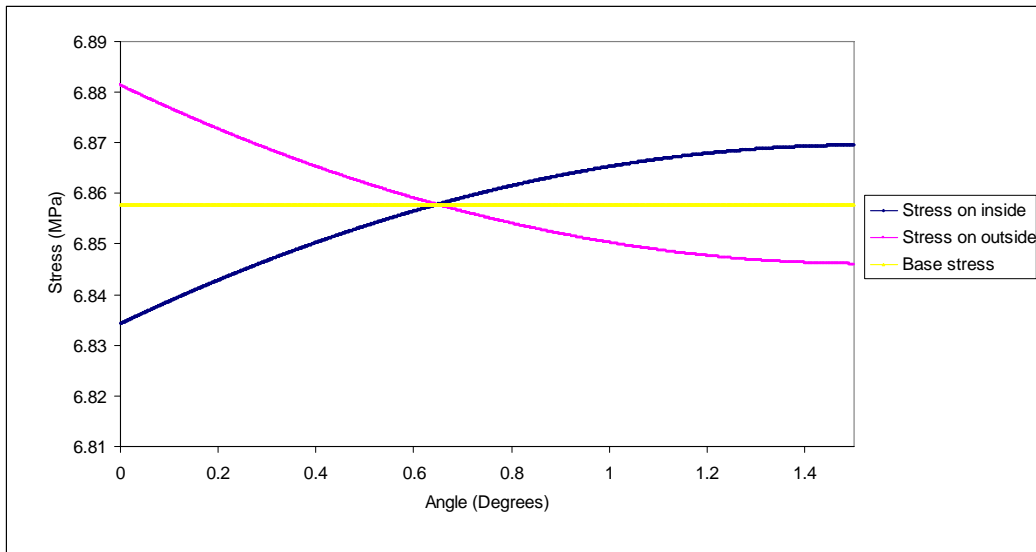
Figure 6-13: The stress distribution across the entire length of a curved beam possessing a wedge angle of 1.53º

It can be inferred from the above theoretical calculations as well as Figure 6-8: The temperature distribution of the spine after year one (a), year two (b) and year three (c) that if the model were to progress beyond the current wedge angle of 0.6°, it is possible that scoliosis progression will halt completely.

This type of growth behavior is based upon one key assumption: the applied load always remains perpendicular to the superior surface of the upper vertebral body. This assumption is founded on the belief that shear loads and any such non-axial loads exerted onto the vertebral bodies are counteracted by muscles, ligaments and other vertebra attachments. For example, recalling Figure

124

2-1, the vertebra facets act to restrict a majority of the motion of the vertebral bodies with respect to one another. Other types of body motion that could potentially induce prolonged non-axial loads would be resisted by ligaments and muscles that serve to stabilize the spinal column. Some of these muscle attachments include, but are not limited, to the multifidus, rotatores (bervis and longus) and constotransverse ligament which aids in spinal stability and maintaining posture [14]. Thus, assuming proper posture is maintained for a majority of the year, spine stabilization muscles, ligaments, as well as facet attachments, should provide enough resistance to prevent the occurrence of substantial shear, torsion and other non-axial loads.

Despite the fact that only a single FSU was modeled, under asymmetric loading conditions there are indications of asymmetric growth, a characteristic of scoliosis growth. In addition, under these particular loading conditions, there is also evidence of a potentially non-progressive, a result not seen in previous scoliosis growth models. Despite the fact that only a single FSU segment was modeled, this study demonstrates that with the correct use of material/element properties and spine geometry, there is a potential that a full spinal column can be developed to predict or estimate scoliosis growth behavior. It is important to note that all previous growth models developed by Stokes and Villemure based their own spine geometry from individuals who were already suffering from the condition as opposed to a healthy spine with no sign of scoliosis. This model fully supports the 'vicious cycle' theory by introducing an asymmetric load to an otherwise healthy spine resulting in asymmetric growth. It also demonstrates the

limitations of this theory as it does not adequately explain non-progressive scoliosis growth.

6.2 Model Limitations

While this particular model was able to adequately simulate growth in a FSU for three consecutive years with characteristics that suggest the onset of scoliosis, it also provides insights into why some scoliosis curves are non-progressive, there are several limitations still present that prevent it from being used in a clinical setting. Some of the more prominent issues in addition to the previously mentioned assumptions are as follows:

- Model scope: Although the current FSU does indicate scoliotic growth, in its current state it provides no information regarding the spine's Cobb angle or the overall growth of the spine. Consequently the current model cannot be directly applied in a clinical setting to model scoliosis growth patterns.

- Loading conditions: The current model assumes that a continuous constant load is applied to the vertebral body. While static loads would have a greater cumulative effect on bone growth as opposed to transient loads that would occur due to bending [33], this model does not take into account the effects of repeated loading that would occur with poor posture, bracing or any other external effect. Also, the loading conditions remain constant from year to year, and do not take into account changes in body mass due to puberty. Finally, this study gives no explanation regarding the initiation or cause behind the asymmetric loading conditions

- Ease of use: In its current form, this model requires familiarity with the Ansys software in order for the appropriate loading conditions, element and contact element assignment in order to solve. In addition, this model also requires the use of a high powered (four processors or above) computer system in order to solve.

- Material/geometric properties: While the model improved upon all known scoliosis growth models by utilizing physiologically accurate geometry, the material properties of the model could be further improved upon by using anisotropic properties for the cortical and cancellous bone. The intervertebral disk could also be improved by using Mooney-Rivlin formulations for the nucleus and annulus ground substance. In addition, this particular model did not take into account the effect of the posterior elements on spine growth. As evident in some extreme cases of scoliosis (Figure 2-14), the posterior elements have to be considered. It can be inferred through comparisons with other scoliosis and spine biomechanics spine models improvements to the geometry of the FSU would have the greatest effect on the finite element model.

- Element type: As discussed previously, a linear elastic element type was utilized for the cortical and cancellous bones. While this element type was adequate in modeling the FSU during the first three years of growth, it proved to be incapable of undergoing any further growth. It is suspected this is due to element distortion due to the growth process. The use of a

different type of element capable of withstanding this type of distortion may allow the model growth to progress further.

- Element mesh: Although the high number of elements within the FSU aided in simulation and geometric accuracy, it also significantly increased the processing time of the model. The introduction of such a high number of elements also resulted in difficulties in maintaining correct element geometry and aspect ratios, especially after each growth iteration. These element geometry errors may have also prevented further model growth.

Chapter 7
Conclusions and Future Work

Through the use of finite element analysis, a functional spinal unit of the L3/L4 vertebra was created to predict spinal growth due to asymmetric loading. While current growth models accurately model scoliosis growth, none of them utilize accurate geometry or material properties. This model builds upon current scoliosis growth models by improving the anatomical and material property accuracy of the spine and evaluating the differences between the model created in this study and the ones developed in past literature.

This current model was designed to improve upon current FEA models by incorporating geometrically accurate vertebra anatomy and tissue mechanical properties. The vertebral body was validated by comparing the stress distributions of the cortical and cancellous bone with an independent study conducted by Li et al. From the study, it was determined that the cancellous bone stress distribution somewhat resembled the model developed by Li. However, in both the cortical and cancellous bone, the von Mises stress values differed significantly. Theoretical manual calculations, on the other hand, demonstrated that the values achieved by this study were reasonable while the ones reported by Li were not. The variations can be attributed to a lack of a cortical shell over the vertebral body in Li's model and also reinforces the importance of modeling both the cortical and cancellous bone components in all FEA as stated in literature.

The intervertebral disk was validated in three ways: comparison of the stress distribution within the disk, lateral disk bulging, and the overall

displacement due to compressive loading. Using Li's model as a comparison for stress distribution, it was found that the two models possessed a similar stress distribution although there were significant discrepancies found with the stress magnitude. Again, theoretical hand calculations were performed to independently verify the stress magnitude values, and it was determined that the FEA provided adequate results. It is suspected that the model developed by Li was incorrectly labeled, but it can also be attributed to the over simplification of material properties of Li's model.

Lateral bulging of the disk was validated by comparing the model with the *in-vitro* studies conducted on cadaveric disks by Heuer. It was determined that under similar loading conditions, the disk bulge achieved in the FEA deviated by the *in-vitro* studies was only 20%, demonstrating that the disk responded to loading appropriately.

Displacement comparisons of the intervertebral disk and the FSU were made against four different FSU models under three different compressive loads. The analysis indicated that under the three different loading conditions, the vertical displacement of the FSU was within the recorded range of results of other spine biomechanics studies.

Once validation studies of the physiological properties of the FSU were completed, scoliosis growth was applied to the model. A uniform compressive load which accounts for the gravitational weight seen on an average L3 vertebra as well as all stabilization muscle forces, was then applied to the model and the z component (vertical axis) stresses data for each element within the vertebra was

recorded. The same process is then repeated for asymmetric loading conditions. The growth modulation equation was subsequently applied to each element to determine element growth based on both biological and mechanical factors. With three years of simulated growth completed, the FSU clearly demonstrated the presence of vertebra wedging due to asymmetric loading. In addition, the progression of this particular model also suggested that under the current loading conditions, the scoliotic curve would develop to become non-progressive. This hypothesis is supported by theoretical hand calculations that demonstrate that at a certain wedge angle, the stress distribution in the lower region of the vertebral body will no longer be the same as the upper portion of the vertebral body, resulting in a change in growth pattern.

While this model was successfully able to simulate scoliosis growth, it had several limitations that prevented it from being directly applicable in a clinical setting. Future work to improve upon this model may include:

(1) The use of hyper-elastic elements as opposed to linear elastic elements. This particular element type better mimics the natural physiological reaction of the vertebra although it would increase the processing time and computational power required.

(2) Modeling of the entire thoracic-lumbar spinal column so that gross spine deformation can be observed. This would provide a more complete picture of spine progression over several years of growth.

(3) Use of anisotropic material properties for the cortical and cancellous bone as well as Mooney-Rivlin formulations to model the intervertebral disk to provide a more accurate physiological model.

(4) Application of bracing forces on a scoliotic spine to determine if external loads on the spine caused by bracing would counter the effects of asymmetric loading. In addition, these simulations may provide insight as to where the ideal placement of loads would be.

(5) Reduction of the number of element meshes to reduce computational time of the model. On average, a single growth iteration for the FSU required two days of computations on a four processor 'super-computer'. Should the entire spine be modeled in the same manner, the simulation could take weeks to complete. If a total spinal column is to be modeled, a reduction in the number of elements is required.

Despite these limitations, this model demonstrated that the use of accurate material properties and spine geometry in scoliosis finite element analysis was capable of not only modeling growth which suggests scoliosis growth, but also demonstrating non-progressive scoliosis growth. It could be argued that simplified models such as the one developed by Stokes and Villemure already model scoliosis growth, none of them provided any evidence of non-progressive scoliosis growth when similar loading conditions were utilized, suggesting that improved geometric properties may have an effect. This information can provide researchers with valuable insight into the type of loading conditions that would cause progressive and non-progressive scoliosis. While this model is not yet ready

to be applied in a clinical setting, the results as seen from a single FSU demonstrate that it possesses great potential, in predicting scoliosis growth behavior. The valuable information may further assist researchers in determining the best course of treatment for those afflicted with this condition. It is hoped that eventually this model will aid researchers in determining the cause of scoliosis, allowing for the implementation of more preventative care.

Bibliography

1. *"Intro to the Human Body."* *SEER's Training Website*. Accessed on: April 14, 2009. <http://training.seer.cancer.gov/module_anatomy/unit1_3_terminology2_planes.html>

2. Chiang MF, Zhong ZC, Chen CS, Cheng CK, Shih SL. Biomechanical comparison of instrumented posterior lumbar interbody fusion with one or two cages by finite element analysis. *Spine*. 2006 September; 31(19):E682-E689

3. Sairyo K, Goel V, Masuda A, Vishnubhotla S, Faizan A, Biyani A, Ebraheim N, Yonekura D, Murakami R, Terai T. Three-dimensional finite element analysis of the pediatric lumbar spine. Part 1: pathomechanism of apophyseal bony ring fracture. *European Spine Journal*. 2006 June; 15(6):923-929

4. Goto K, Tajima N, Chosa E, Totoribe K, Kuroki H, Arizumi Y, Arai T. Mechanical analysis of the lumbar vertebrae in three-dimensional finite element method model in which intradiscal pressure in the nucleus pulposus was used to establish the model. *Journal of Orthopaedic Science*. 2002; 7(2):243-246

5. Lee CK, Kim YE, Lee CS, Hong, YM, Jung JM, Goel VK. Impact Response of the Intervertebral Disc in a Finite-Element Model. *Spine*. 2000 October; 25(19): 2431-2439

6. Totoribe K, Tajima N, Chosa E. A biomechanical study of posterolateral lumbar fusion using a three-dimensional nonlinear finite element method. *Journal of Orthopaedic Science*. 1999 March; 4(2):115-126

7. Li H, Wang Z. Intervertebral disc biomechanical analysis using finite element modeling based on medical images. *Computerized Medical Imaging and Graphics*. 2006 September-October; 30(6-7):363-370

8. Schmidt H, Heuer F, Simon U, Kettler A, Rohlmann A, Claes L, Wilke HJ. Application of a new calibration method for a three-dimensional finite

element model of a human lumbar annulus fibrosus. *Clinical Biomechanics (Bristol, Avon)*. 2006 May; 21(4):337:344

9. Schmidt H, Kettler A, Heuer F, Simon U, Claes L, Wilke HJ. Intradiscal pressure, shear strain and fiber strain in the intervertebral disc under combined loading. *Spine*. 2007 April; 32(7):748-755

10. Van Der Plaats A, Veldhuizen AG, Verkerke GJ. Numerical Simulation of asymmetrically altered growth as initiation mechanism of scoliosis. *Annuals of Biomedical Engineering*. 2007 July; 35(7):1206-1215

11. White A, Panjabi M. Clinical *Biomechanics of the Spine*. Second Edition. Philadelphia: Lippincott Company; 1990

12. Asher M, Burton D. Adolescent idiopathic scoliosis: natural history and long term treatment effects. *Scoliosis*. 2006 March; 1(2)

13. Harris WR, Fleming JFR. "Back Pain" Updated: May 2006. *Workplace Safety and Insurance Appeals Tribunal*. Accessed on: April 14, 2009 <http://www.wsiat.on.ca/english/wsiatDocs/mlo/back_screen.htm>

14. Moore L, Dalley A. *Clinically Oriented Anatomy. Fifth Edition.* Philadelphia: Lippincott Company; 2006

15. "Vertebrae Tutorials Menu." *Get Body Smart*. Accessed on: April 14, 2009 < http://www.getbodysmart.com/ap/skeletalsystem/skeleton/axial/vertebrae/menu/animation.html>

16. "Module 3 – Osteoporosis Management: Pathophysiology of Osteoporosis." *American Medical Association*. Accessed on: April 14, 2009. <http://www.ama-cmeonline.com/osteo_mgmt/module03/02path/02.htm>

17. Ghosh P. *The Biology of the Intervertebral Disk – Volume 2*. Florida: CRC Press; 1988

18. Ghosh P. *The Biology of the Intervertebral Disk – Volume 1*. Florida: CRC Press; 1988

19. Lin H, Aubin CE, Parent S, Villemure I. Mechanobiological bone growth: comparative analysis of two biomechanical modeling approaches. *Medical and Biological Engineering and Computing*. 2009 April; 47(4): 357-366

20. Adeeb S, Herzog W. Simulation of Biological Growth. *Computer Methods in Biomechanics and Biomedical Engineering*. 2009 March; 17(1): 1-10

21. Gille O, Champain N, Benchikh-El-Fegon A, Vital JM, Skalli W. Reliability of 3D reconstruction of the spine of mild scoliotic patients. *Spine*. 2007; 32(5):568-573

22. Regan JJ. "Arthritis and Your Spine: Introduction" Updated: April 10, 2009. *SpineUniverse*. Accessed on: April 14, 2009 < http://www.spineuniverse.com/displayarticle.php/article65.html>

23. "Adolescent Idiopathic Scoliosis" Updated: October 10, 2007. University of Maryland Medical Center. Accessed: April 14, 2009 <http://www.umm.edu/spinecenter/education/adolescent_idiopathic_scoliosis.htm>

24. Grivas TB, Vasiliadis E, Mouzakis V, Mihas C, Koufopoulos G. Association between adolescent idiopathic scoliosis prevalence and age at menarche in different geographic latitudes. *Scoliosis*. 2006 May; 1(9)

25. Greiner KA. "Adolescent Idiopathic Scoliosis: Radiologic Decision-Making." Updated: May 1, 2002. *American Academy of Family Physicians*. Accessed: April 14, 2009 < www.aafp.org/afp/20020501/1817.html>

26. Roaf R. The Basic Anatomy of Scoliosis. *Journal of Bone and Joint Surgery – British Edition*. 1966 Nov; 48-B(4): 786-792

27. MacEwen GD. Experimental Scoliosis. *Clinical Orthopaedics and Related Research*. 1973 June; 93: 69-74

28. Sevastik J, Aaro S, Normelli H. Scoliosis: Experimental and Clinical Studies. *Clinical Orthopaedics and Related Research*. 1984 December; 191: 27-34

29. Pal GP. Mechanism of Production of Scoliosis: A Hypothesis. *Spine*. 1991 March; 16(3): 288-292

30. Stokes I. Analysis and simulation of progressive adolescent scoliosis by biomechanical growth modulation. *European Spine Journal*. 2007 October; 16(10): 1621-1628

31. Stokes I, Burwell R, Dangerfield P. Biomechanical spinal growth modulation and progressive adolescent scoliosis – a test of the 'vicious cycle' pathogenetic hypothesis: summary of an electronic focus group debate of the IBSE. *Scoliosis*. 2006 October; 1(16)

32. Villemure I, Aubin CE, Dansereau J, Labelle H. Biomechanical simulations of the spine deformation process in adolescent idiopathic scoliosis from different pathogenesis hypotheses. *European Spine Journal*. 2004 February; 13(1):83-90

33. Lafortune P, Aubin CE, Boulanger H, Villemure I, Bagnell K, Moreau A. Biomechanical simulations of scoliotic deformation process in the pinealectomized chicken: a preliminary study. *Scoliosis*. 2007 November; 2(16)

34. Adeeb S. CivE 665: Introduction to Finite Element Analysis class notes. 2007 September.

35. Grandin H. *Fundamentals of the Finite Element Method*. Illinois: Waveland Press; 1986

36. Ansys element library

37. Berry J, Moran J, Berg W, Steffee A. A morphometric study of human lumbar and selected thoracic vertebrae. *Spine*. 1987 May; 12(4):362-367

38. Scoles P, Linton A, Latimer B, Levy M, Digiovanni B. Vertebral body and posterior element morphology: the normal spine in middle life. *Spine*. 1988 October; 13(10):1082-1086

39. Zhou SH, McCarthy ID, McGregor AH, Coombs RRH, Hughes SPF. Geometrical dimensions of the lower lumbar vertebrae – analysis of data from digitized CT images. *European Spine Journal*. 2000 June; 9(3):242-248

40. Little JP, De Visser H, Percy MJ, Adam CJ. Are coupled rotations in the lumbar spine largely due to the osseo-ligamentous anatomy? – A modeling study. *Computer Methods in Biomechanics and Biomedical Engineering*. 2008 February; 11(1): 95-103

41. Yao J, Turteltaub SR, Ducheyne P. A three-dimensional nonlinear finite element analysis of the mechanical behavior of tissue engineered intervertebral discs under complex loads. *Biomaterials*. 2006 January; 27(3):377-387

42. Denozière G, Ku DN. Biomechanical comparison between fusion of two vertebrae and implantation of an artificial intervertebral disc. *Journal of Biomechanics*. 2006; 39(4):766-775

43. Cao KD, Grimm MJ, Yang KH. Load sharing within a human lumbar vertebral body using the finite element method. *Spine*. 2001 June; 26(12): E253-E260

44. Eswaran SK, Gupta A, Adams MF, Keaveny TM. Cortical and trabecular load sharing in the human vertebral body. *Journal of Bone and Mineral Research*. 2006 February, 21(2): 307-314

45. Heuer F, Schmidt H, Wilke HJ. The relationship between intervertebral disk bulging and the annular fiber associated strains for simple and

complex loading. *Journal of Biomechanics*. 2008 January; 41(5):1086-1094

46. Villemure I, Aubin CE, Dansereau J, Labelle H. Simulation of progressive deformities in adolescent idiopathic scoliosis using a biomechanical model integrating vertebral growth modulation. *Journal of Biomechanical Engineering*. 2002 December; 124(6):784-790

47. Azegami H, Murachi S, Kitoh J, Ishida Y, Kawakami N, Makino M. Etiology of idiopathic scoliosis: computational study. *Clinical Orthopaedics and Related Research*. 1998 December; (357): 229-236

48. Goto M, Kawakami N, Azegami H, Matsuyama Y, Kenzen T, Sasaoka R. Buckling and bone modeling as factors in the development of idiopathic scoliosis. *Spine*. 2003 February; 28(4): 364-370

49. Ladd A, Kinney J, Haupt D, Goldstein S. Finite-element modeling of trabecular bone: comparison with mechanical testing and determination of tissue modulus. *Journal of Orthopaedic Research*. 1998 September; 16(5):622-628

50. Thomas Edwards W, Zheng Y, Ferrara L, Yuan H. Structural features and thickness of the vertebral cortex in the thoracolumbar spine. *Spine*. 2001 January; 26(2):218-255

51. O'Connell G, Vresilovic E, Elliot D. Comparison of animals used in disc research to human lumbar disc geometry. *Spine*. 2007 February; 32(3):328-333

52. Sharma M, Langrana NA, Rodriguez J. Role of ligaments and facets in lumbar spinal stability. *Spine*. 1995 April; 20(8):887-900

53. Wong C, Gehrchen Martin P, Darvann T, Kiær T. Nonlinear finite-element analysis and biomechanical evaluation of the lumbar spine. *IEEE Transactions of Medical Imaging*. 2003 June; 22(6):742-746

54. Shirazi-Adl SA, Shrivastava SC, Ahmed AM. Stress analysis of the lumbar disc body unit in compression: a three dimensional nonlinear finite element study. *Spine*. 1984 March; 9(2):120-134

55. Singh Ranu H. The thermal properties of human cortical bone: an in vitro study. *Engineering in Medicine*. 1987 July; 16(3):175-176

56. Stokes IA, Windisch L. Vertebral height growth predominates over intervertebral disk height growth in adolescents with scoliosis. *Spine*. 2006 June; 31(14):1600-1604

57. Thomas EW, Zheng T, Ferrara LA, Yuan HA. Structural Features and thickness of the vertebral cortex in the thoracolumbar spine. *Spine*. 2001 January; 26(2):218-225

58. Fagan MJ, Julian S, Siddall DJ, Mohsen AM. Patient-specific spine models. Part 1: finite element analysis of the lumbar intervertebral disk - A material sensitivity study. *Proceedings of the Institution of Mechanical Engineers. Part H, Journal of Engineering in Medicine.* 2002; 216(5):299-314

59. Nachemson A. The Load on Lumbar Disks in Different Positions of the Body. *Clinical Orthopedics and Related Research*. 1966 March-April; 24:107-122

Appendix A

%This script is designed to read text data regarding the stress levels at
  %various element positions. Currently, this script is used for the L3
  %vertebra only although the L4 vertebra data can be easily added (it is
  %currently placed in a separate file.

%This script reads four different files. Symmetric load results for the
  %cortical and cancellous bone and asymmetric load results for the
  %cortical and cancellous bone (again only for L3 at this point).
%---%

%---%
%STEP 1 - read the text files from ansys and create two different matrices,
  %L3symmetric (which stores the symmetric loads and element number) and
  %L3asymmetric (which stores the asymmetric loads and element number)
%Symmetric loads
fid = fopen('L3Cortsym.lis');
L3cor = textscan(fid, '%f %f', 'delimiter', 'whitespace');
fclose(fid);
fid = fopen('L3Cansym.lis');
L3can = textscan(fid, '%f %f', 'delimiter', 'whitespace');
fclose(fid);
L3symmetric = vertcat(L3cor,L3can);
L3symmetric = cell2mat(L3symmetric);
%%This matrix contains the [ELEMENT, Z-DRECTION STRESSES]%%

%Asymmetric loads
fid = fopen('L3Cortasym.lis');
L3coras = textscan(fid, '%f %f', 'delimiter', 'whitespace');
fclose(fid);
fid = fopen('L3Canasym.lis');
L3canas = textscan(fid, '%f %f', 'delimiter', 'whitespace');
fclose(fid);
L3asymmetric = vertcat(L3coras,L3canas);
L3asymmetric = cell2mat(L3asymmetric);
%%This matrix contains the [ELEMENT,Z-DRECTION STRESSES]%%
%---%

%---%
%STEP 2 - Establish the variables used for the rest of the growth analysis
%Base vertebra growth in strain per year, starting with age 8 up to age 20
  %the strain/year values are calculated based on literature. Each
  %subsequent iteration of the simulation will utilize a different

%agegrowth value so that the model responsed accordingly to puberty
%etc.
%Note that a loop was NOT utilized as different stress values are
%required for different age iterations, meaning this script will have
%to be run after each simulation.
%age 8
%base_growth = 0.080311161;
%age 9
%base_growth = 0.06992674;
%age 10
%base_growth = 0.06033324;

%Thermal expansion coefficient in millimeters/millimeter*degree celcius
Alpha = 2.76e-5;
%Growth sensitivity value in 1/MPa
Beta = 1.5;
%--%

%--%
%STEP 3 - Loop to determine the growth rate and the corresponding
    %temperature load required to meet that particular growth value.
%In order for the data to be printed out on excel where it can then be
    %created into a macro, the total data for the L3 model must be broken
    %down into quarters.
%The matrices created by this portion of the script will consist of a
    %single column. All ODD numbered rows are element numbers while all
    %EVEN numbered rows are the temperature load

%First we determine the total dimensions of the matrix we are dealing with
[rows,columns] = size(L3symmetric);
count = 1;
finalrowcount = rows*2;
matrixcount1 = 1;
matrixcount2 = 1;
matrixcount3 = 1;
matrixcount4 = 1;
matrixcount5 = 1;
matrixcount6 = 1;
matrixcount7 = 1;
matrixcount8 = 1;

while (count<=rows)
    if (count<=23115);
        %Assigning the element number into the growth matrix
        Growth_matrix1(matrixcount1,1) = L3symmetric(count,1);

```
    matrixcount1 = matrixcount1+1;
    %Determining growth rate
    growth          =          base_growth*(1-Beta*(-L3asymmetric(count,2)--
L3symmetric(count,2)));
    %Finding the temperature load required to meet the growth rate
    %found above
    Temperature = growth/Alpha;
    %Assigning the temperature load into the growth matrix
    Growth_matrix1(matrixcount1,1) = Temperature;
    matrixcount1 = matrixcount1+1;
  elseif ((count) > 23115 & (count) <= 46230);
    %Assigning the element number into the growth matrix
    Growth_matrix2(matrixcount2,1) = L3symmetric(count,1);
    matrixcount2 = matrixcount2+1;
    %Determining growth rate
    growth          =          base_growth*(1-Beta*(-L3asymmetric(count,2)--
L3symmetric(count,2)));
    %Finding the temperature load required to meet the growth rate
    %found above
    Temperature = growth/Alpha;
    %Assigning the temperature load into the growth matrix
    Growth_matrix2(matrixcount2,1) = Temperature;
    matrixcount2 = matrixcount2+1;
  elseif ((count) > 46230 & (count) <= 69345);
    %Assigning the element number into the growth matrix
    Growth_matrix3(matrixcount3,1) = L3symmetric(count,1);
    matrixcount3 = matrixcount3+1;
    %Determining growth rate
    growth          =          base_growth*(1-Beta*(-L3asymmetric(count,2)--
L3symmetric(count,2)));
    %Finding the temperature load required to meet the growth rate
    %found above
    Temperature = growth/Alpha;
    %Assigning the temperature load into the growth matrix
    Growth_matrix3(matrixcount3,1) = Temperature;
    matrixcount3 = matrixcount3+1;
  elseif ((count) > 69345 & (count) <= 92460);
    %Assigning the element number into the growth matrix
    Growth_matrix4(matrixcount4,1) = L3symmetric(count,1);
    matrixcount4 = matrixcount4+1;
    %Determining growth rate
    growth          =          base_growth*(1-Beta*(-L3asymmetric(count,2)--
L3symmetric(count,2)));
    %Finding the temperature load required to meet the growth rate
    %found above
    Temperature = growth/Alpha;
```

```
    %Assigning the temperature load into the growth matrix
    Growth_matrix4(matrixcount4,1) = Temperature;
    matrixcount4 = matrixcount4+1;
  elseif ((count) > 92460 & (count) <= 115575);
    %Assigning the element number into the growth matrix
    Growth_matrix5(matrixcount5,1) = L3symmetric(count,1);
    matrixcount5 = matrixcount5+1;
    %Determining growth rate
    growth         =        base_growth*(1-Beta*(-L3asymmetric(count,2)--
L3symmetric(count,2)));
    %Finding the temperature load required to meet the growth rate
    %found above
    Temperature = growth/Alpha;
    %Assigning the temperature load into the growth matrix
    Growth_matrix5(matrixcount5,1) = Temperature;
    matrixcount5 = matrixcount5+1;
  elseif ((count) > 115575 & (count) <= 138690);
    %Assigning the element number into the growth matrix
    Growth_matrix6(matrixcount6,1) = L3symmetric(count,1);
    matrixcount6 = matrixcount6+1;
    %Determining growth rate
    growth         =        base_growth*(1-Beta*(-L3asymmetric(count,2)--
L3symmetric(count,2)));
    %Finding the temperature load required to meet the growth rate
    %found above
    Temperature = growth/Alpha;
    %Assigning the temperature load into the growth matrix
    Growth_matrix6(matrixcount6,1) = Temperature;
    matrixcount6 = matrixcount6+1;
  elseif ((count) > 138690 & (count) <= 161805);
    %Assigning the element number into the growth matrix
    Growth_matrix7(matrixcount7,1) = L3symmetric(count,1);
    matrixcount7 = matrixcount7+1;
    %Determining growth rate
    growth         =        base_growth*(1-Beta*(-L3asymmetric(count,2)--
L3symmetric(count,2)));
    %Finding the temperature load required to meet the growth rate
    %found above
    Temperature = growth/Alpha;
    %Assigning the temperature load into the growth matrix
    Growth_matrix7(matrixcount7,1) = Temperature;
    matrixcount7 = matrixcount7+1;
  elseif ((count) > 161805 & (count) <= 184923);
    %Assigning the element number into the growth matrix
    Growth_matrix8(matrixcount8,1) = L3symmetric(count,1);
    matrixcount8 = matrixcount8+1;
```

```matlab
        %Determining growth rate
        growth          =          base_growth*(1-Beta*(-L3asymmetric(count,2)--
L3symmetric(count,2)));
        %Finding the temperature load required to meet the growth rate
        %found above
        Temperature = growth/Alpha;
        %Assigning the temperature load into the growth matrix
        Growth_matrix8(matrixcount8,1) = Temperature;
        matrixcount8 = matrixcount8+1;
    end
    count = count+1;
end
%------------------------------------------------------------------------%



%------------------------------------------------------------------------%
%STEP 4 - Write the data into an excel spreadsheet

%This portion of the code writes the data collected into an excel
    %spreadsheet where it can then be edited as needed and imported into a
    %macro program.

xlswrite('L3growth', Growth_matrix1, 'Growth', 'B1');
xlswrite('L3growth', Growth_matrix2, 'Growth', 'E1');
xlswrite('L3growth', Growth_matrix3, 'Growth', 'H1');
xlswrite('L3growth', Growth_matrix4, 'Growth', 'K1');
xlswrite('L3growth', Growth_matrix5, 'Growth', 'N1');
xlswrite('L3growth', Growth_matrix6, 'Growth', 'Q1');
xlswrite('L3growth', Growth_matrix7, 'Growth', 'T1');
xlswrite('L3growth', Growth_matrix8, 'Growth', 'W1');
%------------------------------------------------------------------------%
```
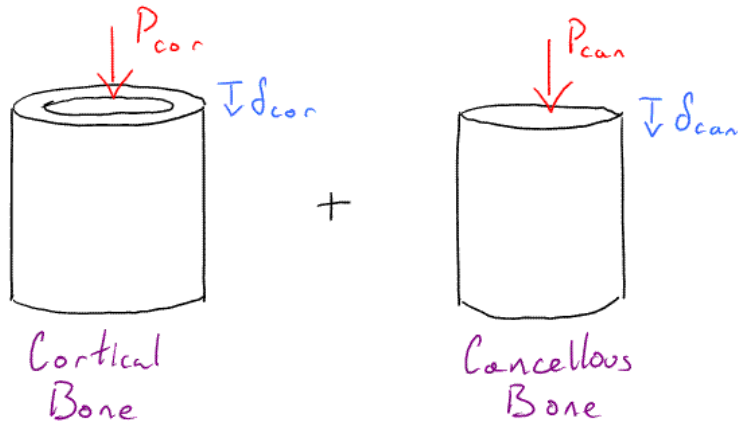
Appendix B

Simplified Bone Stress Values

$$P_{cor} + P_{can} = P_{Total}$$
$$\delta_{cor} = \delta_{can}$$

From displacement analysis

$$\delta_{cor} = \frac{P_{cor} \cdot l}{A_{cor} \cdot E_{cor}} \quad , \quad \delta_{can} = \frac{P_{can} \cdot l}{A_{can} \cdot E_{can}}$$

$$\frac{P_{cor}}{A_{cor} \cdot E_{cor}} = \frac{P_{can}}{A_{can} \cdot E_{can}} \qquad \frac{P_{Tot} - P_{can}}{A_{cor} E_{cor}} = \frac{P_{can}}{A_{can} E_{can}}$$

$$\frac{P_{cor}}{A_{cor} E_{cor}} = \frac{P_{Tot} - P_{cor}}{A_{can} \cdot E_{can}}$$

$$\frac{P_{cor}(A_{can} \cdot E_{can})}{A_{cor} \cdot E_{cor}} + P_{cor} = P_{Tot}$$

$$P_{Tot} = \frac{P_{cor}[A_{can} E_{can} + A_{cor} E_{cor}]}{A_{cor} E_{cor}}$$

$$\therefore \left\{ P_{cor} = \frac{P_{Tot}(A_{cor} E_{cor})}{A_{can} E_{can} + A_{cor} E_{cor}} \right\}$$

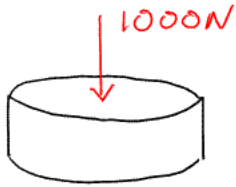$$\left\{ P_{can} = \frac{P_{Tot}(A_{can} E_{can})}{A_{can} E_{can} + A_{cor} E_{cor}} \right\}$$

$\sim\!\!7$ Assuming Simplified geometry and material properties

$P_{Tot} = 1500 N$ $\qquad A_{can} = 1385.44 \, mm^2$

$E_{can} = 200 \, MPa$ $\qquad A_{cor} = 66.76 \, mm^2$

$E_{cor} = 11300 \, MPa$

$$\therefore \begin{array}{l} P_{cor} = 1047.05 N \\ P_{can} = 402.95 N \end{array} \Rightarrow \left\{ \begin{array}{l} \sigma_{cor} = 16.43 \, MPa \\ \sigma_{can} = 0.29 \, MPa \\ \delta_{cor} = 0.048 \, mm \\ \delta_{can} = 0.048 \, mm \end{array} \right\}$$

147

Appendix C

Simplified Disk Stress Values

$$P = 1000\,N$$
$$A = 1175\,mm^2$$

$$\{\sigma = 0.85\,MPa\}$$

If real-times stress is measured then the cross sectional area of the disk will change.

Considering the effects of bulging then it can be assumed that the radius of the disk would increase by 0.55 mm
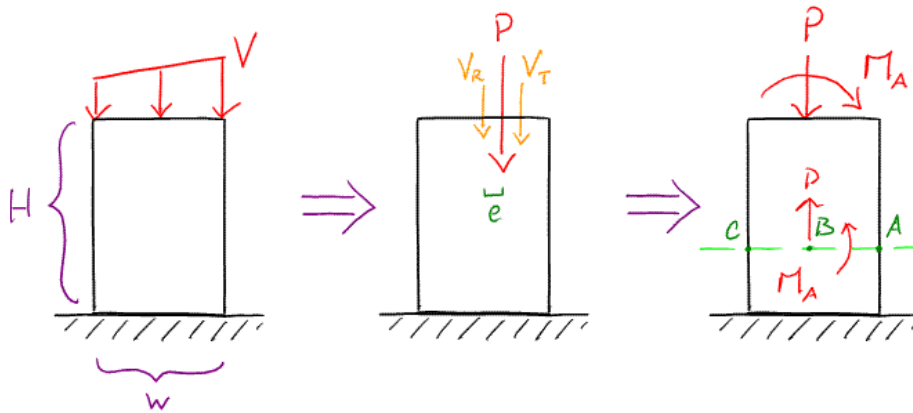
$$\Rightarrow A' = 1242.8\,mm^2$$

$$\{\sigma' = 0.80\,MPa\}$$

Appendix D

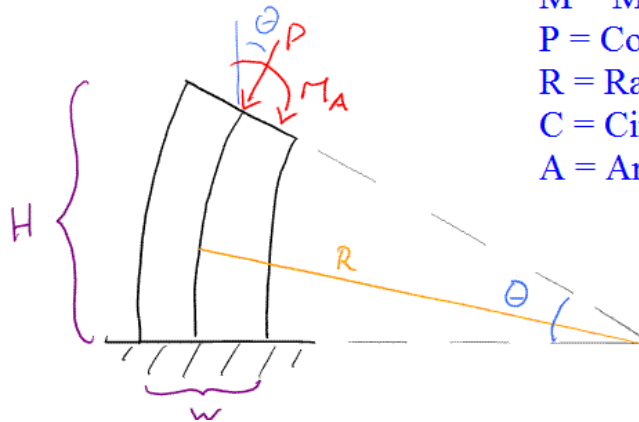## Stress Distribution Calculation for a Curved
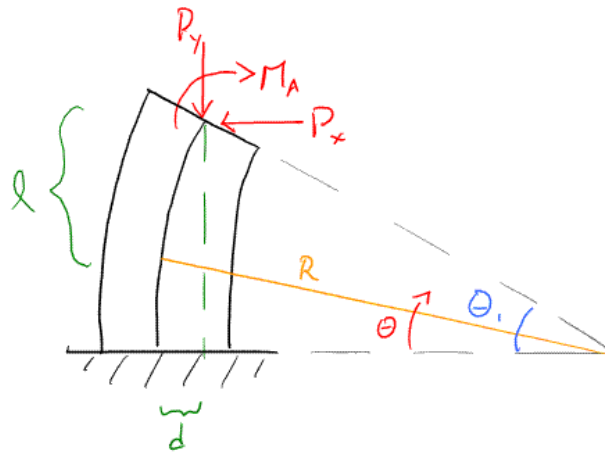

Asymmetric Loading

$$M_A = Pe \quad , \quad e = \frac{w}{2} - \frac{V_R\,w/2 + V_T\,w/3}{P}$$

$$P = V_R + V_T$$

M = Moment
P = Compressive Load
R = Radius of Curvature
C = Circumfrance
A = Area

$$\Rightarrow P_y = P\cos\theta_1$$
$$P_x = P\sin\theta_1$$
$$M = M_A + P_y d - P_x l$$

$$R = C\theta_1$$

$$d = R\cos\theta - R\cos\theta_1$$
$$L = R\sin\theta_1 - R\sin\theta$$

+ve compression
-ve tension

$$\left\{
\begin{aligned}
\sigma_A &= \frac{P}{A} + \frac{(M_A + P_y d - P_x l)w}{2I} \\[2mm]
\sigma_B &= \frac{P}{A} \\[2mm]
\sigma_C &= \frac{P}{A} - \frac{(M_A + P_y d - P_x l)w}{2I}
\end{aligned}
\right\}$$

150